International
Progress Report

IPR-06-18

Äspö Hard Rock Laboratory

Äspö Task Force on modelling of groundwater flow and transport of solutes

Modelling of Task 6D, 6E, 6F and 6F2, using Cast3M code

Christophe Grenier
Gilles Bernard-Michel

ANDRA / CEA

March 2006

Svensk Kärnbränslehantering AB
Swedish Nuclear Fuel
and Waste Management Co
Box 5864
SE-102 40 Stockholm Sweden
Tel 08-459 84 00
+46 8 459 84 00
Fax 08-661 57 19
+46 8 661 57 19

Äspö Hard Rock Laboratory

Report no.
IPR-06-18
No.
F65K
Author
Christophe Grenier
Gilles Bernard-Michel
Date
March 2006
Checked by
Hakim Benabderrahmane
Date
September 2006
Approved
Anders Sjöland
Date
2006-11-29

Äspö Hard Rock Laboratory

Äspö Task Force on modelling of groundwater flow and transport of solutes

Modelling of Task 6D, 6E, 6F and 6F2, using Cast3M code

Christophe Grenier
Gilles Bernard-Michel

ANDRA / CEA

March 2006

Keywords: Fractured block, Retention properties, Tracer tests, Identification, Calibration, Homogenization, Matrix diffusion, Dual porosity, Triple porosity

Sammanfattning (Swedish)

Syftet med modelleringsarbetet inom Task6 är att koppla ihop platsbeskrivningsmodeller och säkerhetsanalysmodeller baserat på data från Äspölaboratoriet. Den förstnämnda typen av modeller är oftast komplexa. De inkluderar detaljerade fysikaliska och geokemiska egenskaper och kalibreras mot in-situ experiment som görs i liten skala under kort tid. Säkerhetsanalysmodellerna är av enklare typ, begränsade till de dominerande fysiska sprickenheterna, vanligen använda för att studera olika möjliga konfigurationer och för långa tidsskalor och stora områden (kilometerskala).

Här presenterar vi resultatet för de delar av Task 6 som relaterar till försöken med det 200 m semi-syntetiska sprickiga bergblocket (över 5600 plana geometriska formationer med sammanhängande egenskaper liksom komplexitetsmönster). Task 6D behandlar frågan om identifiering av systemegenskaper baserat på spårämnesförsök genomförda inom True Block Scale (Test C2). Task 6E studerar transportegenskaperna hos detta block för en blandning av spårämnen från icke-sorberande till starkt sorberande samt byggande av en förenklad säkerhetsanalysmodell. Task 6F behandlar känslighetsanalys som i första hand inkluderar simuleringar på ett enkelt system för att kunna jämföra resultat från olika modelleringsteam som arbetar med Task6F och i andra hand för att studera inverkan av komplexiteten hos sprickorna och även frekvensen för hur sprickorna är ihopkopplade (”connectivity”).

Abstract

The objective of Task6 of the Äspö modeling Task Force exercise is to build a bridge between site characterization (SC) models and performance assessment (PA) models on the basis of the Äspö underground laboratory dataset (Sweden). The first type of models are typically complex. They incorporate detailed physical and geochemical properties and are calibrated against short term and small scale in situ experiments. Performance assessment models are simpler, restrained to the main physical features, generally used to study a variety of possible configurations and apply to long time scales as well as larger spatial scales (kilometric).

We present here the results for the subtasks related with the 200 m semi-synthetic fractured block (over 5600 planar geometrical features with associated properties as well as complexity patterns). Task6D addresses the question of identification of system properties based on the tracer test experiments conducted within the True Block Scale phase (Test C2). Task6E studies the transport properties of this block for a cocktail of tracers ranging from non sorbing to largely sorbing and building of a simplified PA model. Task 6F is devoted to sensibility analysis firstly including simulations on a simple system allowing for comparison of results between the various modeling teams working within the task, secondly, studying the influence of fracture complexity as well as fracture connectivity.

Executive summary

The present document reports the studies associated with transfers within a semi synthetic 200 m fractured block defined in former Task6C [*Dershowitz et al. 03*].

Results are detailed along the various subtasks. Task 6D deals with calibration of a tracer test addressing the issue of level of information contained in tracer tests and its constraining power for PA time scales. Task 6E deals with transport properties of the semi synthetic block for PA time scales. Task 6F provides a common ground to compare transfers within a simple feature for the different modeling teams. Task 6F2 first addresses issues dealing with complexity of fractures, its modeling and impact on transfer properties, secondly, this task addresses issues related with connectivity of the system and its impact in terms of shape of breakthrough curves as related with limited matrix diffusion effects.

Task 6D

This subtask deals with a semi synthetic 200m fractured block. It incorporates 11 measured fracture zones as well as 25 synthetic 100m scale units and 5660 synthetic lower scale units referred as Back Ground Fracturing. The synthetic features are generated to account for the fracturation statistics measured at the site. Full complexity of the larger scale fractured zones is accounted for as well.

The purpose of this task is to address the issue of identification of the flow and transport parameters associated to the major features of the system from a tracer test conducted at the site (referred as Test C2). This test involves a limited volume of the former block, roughly located around features 20, 21, 22, 23.

Our contribution to the task more precisely consists in:

- Modeling of the system and simulation of the pumping conditions and tracer test for the different tracer considered.
- Calibration of the parameters of the system: we look for one single deterministic parameter set involving homogeneous matrix diffusion zone along the flow path.

- Sensitivity analysis to the most sensitive parameters: fracture aperture dominantly responsible for arrival times.

In our modeling strategy, we indeed rely here upon the results obtained along Task 6A and 6B. These subtasks were similar to task 6D except that the system was simpler, limited to a single fracture. We raised the question of the level of complexity to be incorporated in the model as compared with the constraining power of the information contained in the tracer tests. Results showed that the level of information contained in the tracer tests only allows for the identification of simple major features of the system: advective travel time (flow properties and transport porosity along the main flow lines) and averaged properties of immobile zones in the vicinity of the mobile zones, combined with dispersion in the fractures. These are mainly responsible respectively for the peak arrival time of the breakthrough curve and the spread of the curve. In addition to this, the parameters to be identified from the tracer tests considered were shown to be useless to account for long term transfers. The same is true here. The level of information provided by the tracer test is here relatively lower due to the uncertainties related with a block of at least 4 fractures as compared with a single fracture case. The units explored by the plume are for the present situation: 4 fractures (geometry, properties) the intersections involving incoming freshwater and the rest of the heterogeneous matrix volume. The amount of parameters to be identified is larger. Identification of these features can't be expected based on the provided tracer tests and the experience gained in the single fracture case.

In consequence, our approach here is very basic in terms of geometrical complexity of the system. The model considers the 11 deterministic fractured zones provided in the specifications for the flow problem. A sub model for the local tracer test limited to 4 fracture zones (feature 20 to 23) involving homogeneous matrix zone properties is considered for the calibration of the tracer test. The flow boundary conditions are taken from the former larger scale model (all deterministic features). The identification problem corresponds to the estimation of the individual fracture apertures for the 4 features modeled (additionally surface sorption coefficient for sorbing tracers) as well as a homogeneous matrix zone property (porosity, diffusion coefficient, retardation coefficient). Flow parameters, not calibrated, are taken from the deliveries. We search for a unique deterministic parameter set for optimal calibration of the system. This parameter set proved coherent with the measurements available for matrix properties. Sensitivity analysis are conducted based on this optimal set.

From the simulation side we proceed here in two steps involving two modeled systems. A larger 200m scale model is first considered providing the boundary conditions for the lower scale model explicitly modeling the 4 deterministic fractures concerned by the tracer test and used to fit the breakthrough curves. These models are built in our Cast3m code based on Mixed and Hybrid Finite Element scheme for resolution of flow and Finite Volume scheme for the resolution of Eulerian transport. Additional information about these models follow:

1. The 200 m model involves a smeared fracture representation of the fractured system

(limited to the 11 deterministic features). It takes the provided boundary conditions into account and simulates the pumping test (continuous radial converging).

2. Test scale model meshes the 4 deterministic features (20 to 23) with adjacent matrix zones. Boundary conditions from the preceding larger scale model are applied. Transport is simulated for Dirac input and convoluted with the input injection concentration curve. Manual fitting procedure is conducted considering different fracture apertures, dispersion coefficients and matrix properties.

As mentioned previously, the level of information provided by tracer tests (as inferred from previous steps of the task) is very limited whereas the uncertainties are large (geometry, parameter sets, structure of the heterogeneity ...). So we do not consider that we really address here an issue of identification of the system based on Tracer Test C2. We should rather say that we show that for the chosen deterministic set of parameters (within the expected range of values), a satisfactory level of fit (of breakthrough curves) can be achieved. In fact we more verify here that our approach is coherent with the dataset provided, building confidence in the case studied and associated results. Nevertheless, other views of the system are possible and the level of information contained in the tracer test does not allow discrimination.

So work associated with Task6D involves (i) calibration of the system based on homogeneous matrix diffusion coefficients (porosity, diffusion coefficient, penetration depth) and four fracture transport apertures, (ii) check that these parameters well fall into the expected parameter range (as related with the complexity of the features), (iii) Sensitivity analysis study (here limited to the most sensitive parameter as identified in previous phases of the task: fracture apertures controlling the advection time).

The major results follow :

- Good level of fitting could be achieved based on minor changes in the base line parameter sets provided in the specifications. The calibrated matrix properties fall well into the expected ranges considering the data and geometrical features provided. Further refinements of the model are not required from the point of view of the fitting of the tracer test results. This calibrated system is nevertheless not the unique solution, the inverse problem issue being non unique even for the simple system considered here. In particular, it is hard to discriminate spreading of breakthrough curves originating from dispersion in the fracture plane and from matrix diffusion. Similarly, to a certain extent, comparable breakthrough curves are obtained for smaller transport porosity in the fractures (lower advective arrival times) and larger matrix diffusion effect (larger porosity or diffusion coefficient).

- The most sensitive features from this system are related with advective arrival times whatever the tracer considered. The most important parameters are for the transport problem: fracture apertures and surface sorption coefficients. The influence of matrix diffusion in the transport processes proved here more important than for Task6A and B due to the larger contact time with the matrix zones along the larger

travel path. This influence remains anyway still secondary as compared with former properties associated with the arrival of the peak. Indeed, a change in 50% in matrix properties does not so much affect the shape of the breakthrough curves as for a similar change in fracture aperture or sorption properties (intermediate to largely sorbing tracers). A correlated result is that the tracer test better constrains the fracture apertures than the dispersion coefficient or matrix properties.

So, we do not expect sufficient constraining power of the tracer tests as a whole for the future steps of the task. As a consequence, in our approach to Task 6E, we will not condition our model to these tracer tests. Task 6E and 6F will include study of the impact of the different levels of heterogeneity contained in the definition of the semi synthetic block (Task 6C): main conducting features, complexity of the fractured zones, back ground fracturing. These features indeed potentially play an important role in long term transfers and associated retention processes. They were not included in Task 6D since these could definitely not be constrained from the tracer tests breakthrough curves provided.

Task 6E

Task6E addresses the issue of prediction of transport of a cocktail of tracers at post closure time scale. It follows Task6D which was expected to build a common ground for the block models by incorporating constraints related with information contained in the available tracer tests (breakthrough curves). Nevertheless, our results showed that tracer tests poorly constrain the system for PA (Performance Assessment) time scales (hundred thousands to million years). In consequence, no attempt was made here to constrain the model for Task6E study to Task6D tracer tests.

Our simulation approach for Task6E relies upon explicit modeling of the geometrical features according to the geometries and properties provided in the deliveries. Fractures are represented as 2D planes and discretized with triangular elements. Intersections are 1D elements where continuity of fluxes is obtained. Flow is limited to the features provided (matrix blocks are considered no flow zones). Steady state flow is solved within Cast3M code with a mixed and hybrid finite element scheme (MHFE). Transient transport in the fracture network is solved with an Eulerian approach with the same code. This scheme provides indeed valuable advantages in mass conservation for such a fractured network with highly contrasted properties. Transport in the fracture network includes advection, dispersion, diffusion as well as linear sorption effects. Transport in the matrix blocks is considered as well. It corresponds to diffusion into the matrix blocks as well as linear sorption effects. This phenomenon delays the tracer arrival. It is here included in the model by means of a semi-analytical approach (no numerical simulation based on discretization of the matrix zones). Matrix diffusion is computed according to analytical solutions of diffusion in 1D systems (1D infinite, limited 1D, composite medium). Introduction in the Eulerian transport equations is straightforward. This is achieved by means

of an additional source term whereas coupling between fracture and matrix relies upon fracture concentration forcing history for the convolution of matrix evolution of mass as well as source term for fracture concentration evolution. The resulting temporal scheme is fully implicit. The model retains very complex and highly variable patterns of flow and transport in the fracture block as well as within each fracture plane.

Fracture complexity is fully accounted for in a deterministic manner. Dominant fracture type is applied to each modeled fracture. This complexity can be fully accounted for in the model presented above. Previous studies showed indeed that for PA time scales matrix zones in the vicinity of the fracture plane react quasi instantaneously to mass in the fracture. Such zones are equivalently represented by means of a retention coefficient applied to the fracture transport equations. The corresponding matrix zones are fracture coating for Type 2 features and fracture coating, gouge, Mylonite for Type 1 features. Altered and non altered granite for both Type 1 and Type 2 features are represented by means of the semi analytical approach sketched out previously (1D diffusion in a composite medium).

Simulations are conducted for the tracer cocktail and the properties and head gradient provided in the deliveries. Performance measures required in the deliveries are produced. These enclose mainly breakthrough curves through several observation planes as well as mass flux exiting the modeled block.

Final results include 1200 main fractures from the initial semi-synthetic block of 5600 fractures. These features were selected after (i) ordering the fractures by decreasing order of size, (ii) retaining minor fractures present in the vicinity of the source term location, (iii) studying connectivities within the fracture network for a sample of 3000 larger fractures, (iv) studying sensitivity of flow and transport properties of the block to the amount of fractures included.

Sensitivity analysis to different other parameters are considered. These analyzes aim at assessing the quality of the numerical simulations or address physical modeling issues:

- Numerical studies include convergence of the simulations as regard to mesh size, time step, sensitivity to dispersion coefficient.
- Physical modeling issues include sensitivity to the amount of fractures considered (main or minor contributors and associated influences), sensitivity to local matrix properties (complexity factor, fractures purely Type 1 or 2), sensitivity to matrix units located more in the depth of the rock (altered and non altered rock) including their representation and depth (limited versus non limited matrix diffusion, composite or homogeneous properties).

Main conclusions are:

- For the PA time scale considered, a very first order controlling effect to transport in the block corresponds to matrix diffusion effects. Matrix diffusion introduces

important retardation effects. The impact on peak arrival time corresponds to a factor of 10 for non sorbing Iodine to 5.10^5 for Americium (adding to sorbing effects). The maximum flux is reduced by a factor of 50 for Iodine to 3.10^6 for Americium. The impact in terms of arrival time of 95% of the mass is larger due to tailing effect related with matrix diffusion effects. The retardation in 95% ranges from 3600 for Iodine to 4.10^7 for Americium. Penetration depths by the order of several meters to 10 meters are observed. These show that diffusion processes range largely over local effects strictly located around fracture planes. This is clearly in contrast with experimental forced flow regimes for which only high diffusion matrix zones in the vicinity of the flow have a real impact on transport properties. More detailed analysis of the impact of the various matrix zones show that intact rock as well as the altered diorite are here the major contributors to this retardation effect. Matrix zones closer to the conducting unit, like fracture coating, gouge and cataclasite can be represented as retardation factor. Their impact is comparable in amplitude, though smaller, to the impact of altered and non altered rock when considering peak arrival times. Analytical expressions are proposed and validated to estimate the retardation coefficient associated with the role played by these roles in retarding the breakthrough curve peak arrival time.

- The geometrical system of the semi synthetic block provides complex structures of flow and transport. Largest fractures are responsible for larger scale transfers whereas minor fractures do not increase the connectivity of the system. The main features of the flow and transport patterns are surprisingly well accounted for when reducing the amount of modeled fractures. The extreme case of 12 fractures (main conductors + minor fractures in the vicinity of the source location) even yield predictions with very acceptable results (roughly below 10% for the performance measures considered). This simplified system provides breakthrough curves with low sensitivity to the integration of additional features. This means that among this complex system, those 12 features have a first order impact on the system output whereas other features lead to second order effects on breakthrough curves. These effects can nevertheless hardly be read from the curves but should consist in providing porous space to increase the travel paths and travel times of mass particles associated with the tracer. These would consist actually of slower velocity zones to dead end features and results in increasing the tailing of the breakthrough curves at the outlet of the system.

- This properties of the system (boiling down to a limited amount of 12 major features) was not expected at the beginning of the task. Efforts were put in trying to understand the reasons for such a result. This property is related (1) with the actual structure of the fracture network (limited amount of smaller connected units) as well as with (2) secondary, the boundary conditions imposed to the block. Another reason can be found in the limited volume of the source considered (spatial Dirac). The first two items were studied at some extent. Though preliminary, results show

that the main reasons for selecting a single travel path, are mainly to be found in the connectivity of the global system. The boundary conditions of lateral no flow only play a secondary role in amplifying the importance of fracture paths connecting input with output sides (involving Features 23D, 1925B, 22D, 21D, 20D, 2292B, 17S and 19D). Indeed, inflows from the sides over fractures connected with the other sides are limited by the no flow boundaries.
The 12 fracture system appears as a very efficient simplified PA model and a very good compromise between precision, complexity, and numerical efficiency (limited time consuming).
Further efforts are required to assess the role of minor fractures in the transport properties of the system.

- Other features are identified as having second order influence on breakthrough curves and transport properties. Besides smaller scale fracturing presented formerly, dispersion coefficients associated with fractures have minor impact on the breakthrough curves. The spreading of the curves mostly results from the dispersion along the fracture network. Due to the penetration depth of matrix diffusion, actual composite medium (altered rock over 20cm + non altered rock) is hardly discriminated from homogeneous (altered rock) matrix. Similarly, simulations considering dominant fracture type or full Type 1 fractures are roughly comparable.

- Matrix diffusion is here modeled as a retardation coefficient for the higher porosity zones in the vicinity of the fracture (fracture coating, gouge, cataclasite) and local diffusion into adjacent 1D zones for more in depth matrix zones (altered and non altered rock). We don't model explicitly the full 3D geometry of the matrix blocks delineated by the fracture network. This could appear as a major limit of our approach. Nevertheless, when modeling 1D diffusion, a mean term could consist in having location dependent depth (at least depending on the actual neighbor block size). So, due to the variability of matrix block sizes, variable properties should be applied corresponding to local depth available. This was not done here either. Nevertheless, our approach proves a posteriori sufficient and conservative for the semi synthetic block considered. Indeed, the geometry of the main contributors to transport boils down to two main travel ways. The distance between these main travel path proved larger than twice the penetration depth of the tracers into the matrix. Modification of matrix properties to account for the presence of minor back ground features would be required but should not lead to major differences. Our results are nevertheless conservative since more diffusive and porous matrix zones should lead to more delayed arrivals.

Possible perspectives of the modeling work are sketched out in the document. A first idea would be to study the transport properties of the system considering a spatially extended source. Such an non punctual source would possibly integrate a larger amount of transport paths while being more representative of a volumic waste package. Another line of development would consist in working on other test cases, requiring other realizations

of the same initial process which lead to the semi synthetic fractured block selected in Task 6C.

Task 6F

The aim of Task 6F is to provide a basis to compare the results previously obtained by different modeling groups. The large variety in conceptual models associated with former tasks lead to large spread in results and predictions. This subtask helps in analyzing these differences since a series of relatively simple benchmark tests are conceptualized and simulated. Moreover detailed description of the implementation of the systems is provided clarifying the approach to fracture flow, matrix heterogeneity representation, ... Two single fracture units (Feature 1S and 4S) from the semi synthetic block (Task 6C) associated with matrix zones corresponding to pure Type 1 and Type 2 matrix properties are considered. Transfers for Dirac pulses and 3 tracers from non sorbing to intermediate sorbing are simulated. Performance measures include breakthrough curves at a collection line as well as other associated parameters. Different prescribed hydraulic gradient values are applied.

In addition to meeting the requirements of Task6F, we include some analysis of the present results along two main lines. We provide with (i) elements of understanding and quantification of delays associated with sorption and matrix diffusion; (ii) study of the evolution of masses in the various matrix subunits leading to a simplified representation of the system. To achieve this, we introduced another series of simulations named Cases A3, B3, C3.

Task 6F2

Results along two directions are summed up there and complement the work performed before:

- Impact of fracture complexity on transport patterns considering fracture complexity as a several smaller features of Type 1 and Type 2 in series and parallel. Such complex systems are not easily homogenized by an equivalent 1D model (advection, dispersion, matrix diffusion). They would require further modeling efforts for inclusion in the Task 6E model.

- Impact of various scales of fracturation for a fully connected fractured system: case of double and triple porosity in a sugar box geometry. Former results obtained within Task 6E showed that the 5600 fracture system could be simplified to a 12 fracture system for the boundary conditions and initial plume location considered. This is mainly due to the low connectivity of the fractured network and results

into large tailing effects in the breakthrough curves due to the large matrix depth around the main transport path. We provide here with an opposite case consisting in fully connected fractured network (sugar box geometry) including properties taken from Task 6C and uniform flow conditions as in PA conditions. Delays in arrival times associated with matrix diffusion are large in agreement with former results. Nevertheless, the shape of the breakthrough curves significantly differ.

Contents

List of Tables

List of Figures

Chapter 1

Introduction

1.1 Background

We present here a contribution within the framework of the Task Force organized by SKB with the Äspö database (see e.g. [1]). Task 6 is devoted to providing a bridge between detailed modeling scale corresponding to decameter scale blocks for flow and tracer tests conducted at monthly to yearly time scale (accessible to experiments in forced flows) to the PA (Performance Assessment) scale corresponding to natural or post closure conditions (much longer spatial and time scales to several kilometers and million years). The present report provides the second part of the TASK6 modeling work, namely Task 6D, corresponding too calibration of tracer test, Task6E corresponding to PA modeling of a semi-synthetic fractured block issued from Task 6C and Task 6F dealing with sensitivity analysis to various patterns of the system.

The different sub tasks within Task6 are outlined in section 2. Briefly, Task6D is the counter part of Task6A in the sense that both tasks address the issue of identification of system properties based on breakthrough curves obtained from tracer tests. But Task6A dealt with a single fracture system at decametric scale whereas Task6D involves a fractured block at hectometric scale. Furthermore, these tasks have in common that they should provide a common basis for the predictive step associated. The information obtained from the tracer tests as well as from independent measurements are included in simplified PA models considered for predictive purposes. Task6B considered this predictive step for the single fracture case and for two types of slower flow regimes. Task6E is considering transfers at PA time scale and uses calibrated information as a common basis (Task6D).

The main results from Task6A and Bs are the following (see [*Grenier 03*]):

- Task 6A: the information contained in the tracer tests does not strongly constrain the system. The more complex the system, the less constraining their power (more

unknowns associated). Due to the structure of tracer tests, expressed in terms of homogenized model, the information provided boils down to an advective travel time (identification within flow problem and transport porosity or aperture), a dispersion coefficient

and an averaged matrix property (mean matrix diffusion coefficient and porosity). Constraining power on properties associated with arrival time is stronger. The spreading of the curve corresponds to effects related with the latter two effects so that it is hard to separate them. The calibrated matrix properties correspond to a mean property over matrix zones in the vicinity of the flow path and providing the larger diffusion coefficients (gouge, fracture coating, mylonite).

- Task 6B: a simplified representation of the system was proposed for PA time scale. It focuses on the retention effects related with diffusion (and sorption) into matrix zones. The higher diffusion zones in the vicinity of the flow paths act as simple buffers to the tracers for PA time scales (slow flow regimes). Transport is no more dual porosity like but single porosity (no effects like transitory storage and delayed restitution). Matrix zones more in the depth of the blocks are accessed by the plume due to larger contact times. These zones provide transitory storage volumes. The resulting PA model is simple, considering an equivalent flow channel with an additional equivalent matrix zone. The first includes the more diffusive matrix zones in the vicinity of the flow field as an increased transport porosity (or equivalently retardation coefficient). The second homogenize the properties of the matrix blocks in the depth of the rock (altered and non altered granite properties). Results showed that little information could be retained from the former tracer tests due to the fact that the transport regimes strongly differ for forced flow time scale (tracer tests) and natural flow time scale (PA time scale).

    1. The formation parameter governing dual porosity behavior identified from tracer tests is different from the formation parameter controlling transport for the slower regime (involving the total porosity offered). So strictly speaking no information can be transferred from tracer tests to PA time scale. The formation parameters involved are for dual porosity regime $\sqrt{RD}/e$ (R for retardation coefficient, D for matrix diffusion coefficient and e for fracture aperture) and for single porosity regime an equivalent pseudo retardation coefficient or pseudo sorption coefficient by $K_a = dR\omega$ (d for depth of the zone, ω for porosity of the zone).
    2. Nevertheless, if we provide a relationship between D, ω and R, identification of the first parameter formation allows for a unique value in terms of the second parameter formation. Such a relationship could be inferred from independent sample measurements for the different matrix zone properties. Results show that the constraining power of tracer tests remains nevertheless reduced. This is mainly due to the fact that in depth zones concerned by PA time scales are not touched and consequently not identified by tests conducted at smaller time scales.

- Task 6C consisted in building a semi-synthetic fractured block based on measured fractures from the Block Scale experimental zone as well as additional synthetic features simulated in agreement with the statistical properties measured at the block. The results are provided in [*Dershowitz et al. 03*].

1.2 Objectives

1.2.1 Task 6D

We follow here the same line as for previous steps of Task6 as outlined previously in a former report related with Task 6AB [*Grenier 03*]. The system geometry is here (Task 6D) clearly more complex (than Task6A) involving at least 4 deterministic feature sections (features 20 to 23), the associated transport porosities as well as adjacent matrix zones. The flow in these units is more complex as well than for Task6A since the major flow line connecting injection and pumping wells is expected to be sensitive to inflows at fracture intersections. In consequence we limit our calibration ambitions to a simple system involving the former 4 features as well as an homogeneous matrix zone along the fracture. We consider that further complexity can't be constrained from the tracer tests. We confirm below that this system is successful as it properly matches the breakthrough curves provided. As a consequence, some information provided in the task deliveries is not considered in our model. This encloses fracture complexity (type 1 and 2 and complexity factors) or heterogeneity of the matrix zones.

Moreover we do not take the information related with back ground fracturing into account. These features are potentially important since they could be responsible for multiple flow paths between the input and output wells. This issue is not addressed here. Nevertheless, the full complexity of the system will have to be considered for the future task6E. In view of the prediction phase, the importance of the different sub units of the system will have to be identified. The treatment of back ground fracturing as well as fracture complexity belongs to it. Moreover we do not work here with two systems as suggested in the specifications, a detailed one (SC) and a more simpler one (PA) since we do not consider possible identifying more features than the one contained in our simple model (to be referred as PA like) due to the limited constraining power of the experimental tests.

1.2.2 Task 6E

The main objective for Task 6E is to provide predictive simulations in the semi-synthetic block for the PA time scale conditions provided. The following issues are addressed as well, aiming at studying the flow and transport properties of the block and the impact of the various sub-units of the system:

- Sensitivity of the flow and transport properties of the block to the amount of modeled fractures. A reference case is proposed with 1200 fractures which is considered to be a sufficiently converged system. Another case is proposed pertaining on the contrary a minimum amount of fractures (12 units) while providing satisfactory precision in the breakthrough curves and performance measurements. Reasons for the appearance of such a single major pathway are studied considering the connectivity of the system and the type of boundary conditions imposed.

- We study the role played by matrix zones. We show the overall impact of matrix zones in terms of retention properties at PA time scale. More detailed analysis of the role played by intact rock zones is provided as well as associated penetration depths.

- We propose a conceptualization and associated modeling approach for the local complexity of the fractured zones (heterogeneity of matrix zones in the vicinity of the fracture aperture). We study the impact of this heterogeneity knowing that the properties associated to these zones are poorly constrained.

Sensitivity of the results to spatial and temporal discretization as well as dispersion coefficients is studied as well to assess the numerical quality of the results.

1.2.3 Task 6Fs

This subtask corresponds to two major objectives:

- Simulate simplified reference cases for the purpose of comparing the results obtained by the different teams participating into the task.

- Show the sensitivity of the system to various factors not extendedly treated formerly like fracture complexity and connectivity at various scales of the fractured system.

1.3 Outline of the report

In the following, we first recall the different steps of Task 6 treated in this report (chapter 2). Then our modeling approach is sketched out in chapter 3 involving a presentation of our code, the modeling strategy, and conceptualization of the different units of the system (conducting features, fracture complexity, matrix zones). We then move to the detailed description of results for Task 6D (chapter 4), Task 6E (chapter 4), Task 6F and Task 6F2 (chapters 6 and 7). Conclusions and perspectives follow (chapter 8).

Chapter 2

Modeling tasks

2.1 Task 6C - hydro structural model

This task provided the modeling groups with a semi synthetic block scale system (200 m) to work with, including a tracer test for future calibration of the models as well as detailed characteristics of the heterogeneity of the block: deterministic as well as synthetic features, description of the various types of fracture zones with complexity factors and back ground fracturing involving different scales of fracturation. A large dataset for the parameters is provided. The tracer test C2 was conducted on the TRUE Block scale location and is coherent with the semi synthetic system provided. It is moreover used to calibrate the system in the present Task6D step of the task and will provide the basis for Task 6E aiming at predictions at PA time scale. One may refer to [*Dershowitz et al. 03*] for more related information.

2.2 Task 6D - Block scale transport on a tracer test time scale

We addressed the problem of identification of parameters based on the information provided by tracer test C2 involving different tracers ranging from non sorbing to intermediate sorbing. This task constitutes a common basis for Task 6E. The task specifications are provided in [*Elert et Selroos 02*].

2.3 Task 6E - Block scale transport on a PA time scale

This task addresses the issue of providing a bridge toward PA time scale for a 200 m block involving a large variety of deterministically identified features complemented by other

levels of fracturation which in this case are not measured in situ but simulated according to statistical measurements. The task specifications are provided in [*Elert et Selroos 04a*].

2.4 Task 6F - Test bench mark

Task6F is a kind of benchmark test on simple systems or building blocks extracted from the more complex situation in the semi synthetic block (Task 6C) considered for the rest of the modeling work. Task6F provides the opportunity to compare the modeling approaches from the different modeling groups within the Task Force as well as allows for a better understanding of the differences in the transport results. According with the specifications of the task, two single fracture systems are considered for two simple types of matrix complexity. Transfer within these units are modeled for 3 regimes depending on the uniform head gradient imposed. Specifications for the task are provided in [*Elert et Selroos 04b*].

2.5 Task 6F2 - Sensitivity study

Task6F2 deals with sensitivity of results to different factors, specially complexity of fractured zones.

Chapter 3

Model description

We present here the main features of the model for flow and transport as retained for Task 6E. Approximately, the same is true for Task 6D work whereas the system is then simplified to major deterministic units as well as simple matrix properties with the idea that highly detailed system cannot be constrained by tracer test data (a sound understanding of the flow field is a prerequisite).

3.1 Implementation of the Task6C semi-synthetic hydro-structural model

Task6C semi-synthetic hydro-structural model contains detailed information about several scales of heterogeneity within a 200 m fractured block. One may report to [*Dershowitz et al. 03*] for detailed presentation of the block.

Roughly 5600 features are provided including geometry (planar objects), flow and transport properties. In addition, complexity is associated with these units. Those conducting features are indeed found along fault or non fault zones. Fractures or portions of the fractures are schematically divided into Type 1 (fault zone) or Type 2 subunits (non faulted zones). Their geometry is recalled on figures 6.2. The larger fractures belong quite often to fault types. In addition those units can possibly be of higher complexity, meaning that these larger conductive features are composed of several flow conducting channels in series or parallel or even leading to a local fracture network embedded in heterogeneous matrix. Indications for the number of such channels are provided but no actual geometry is given.

We here take the provided fracture plane geometry into account. We consider 1200 fractures for the reference case (see reasons below). Complexity associated with the fractures is limited to a single type all along the fracture plane. A single flow channel is considered in the present study. Reference calculations involve fractures with the domi-

nant type (1 or 2). The geometry of the system, the processes considered, mathematical model, numerical implementation and parameters are detailed in the following sections.

3.2 Geometrical description

3.2.1 Fracture network

We consider a deterministic approach retaining a fraction of the fractures provided. 1200 fractures are considered in our final predictive model. Selection was conducted based on a sensitivity approach to the incremental introduction of an additional fracture, considering the size of the fracture as well as its position in the block. The situation for 150 fractures is provided on figure 3.2(a) with a closer zoom on the source location (feature 23D) 3.2(b). This geometry is considered in the following for sensitivity analysis. We also provide the situation for the 1200 fractures system of the final reference model on figure 3.3.

Fractures are represented as planes. Intersections are 1D. This geometry is acceptable since all objects considered here are very thin compared to their extent. Fractures are discretized with triangular plane elements. Discretization should be sufficient for each fracture to allow for a good representation of flow and transport. Due to the complexity of the geometry (fractures and intersections), we considered a number of meshes per fracture ranging from 300 to 10,000 triangles, depending on the size of the fracture. The choice of 1200 major fractures for the reference calculation results from connectivity studies on 3000 larger units and sensitivity analysis of block properties to the amount of fractures included ordered by decreasing order of sizes. Smaller units would nevertheless require more refined discretization of the system leading to large computer costs. Indeed smaller units should still be represented with sufficient precision to account for complex flow and transport features.

Boundary conditions, parameter values and properties are directly taken from the deliveries.

3.2.2 Pore space

Complexity of the conducting features is simplified to dominant type associated to the unit. For instance when Type 2 is dominant type, the corresponding unit is affected Type 2 all over its surface.

Lacking any further information, Type 1 and Type 2 units are modeled deterministically and strictly as provided in the deliveries as fracture coating, gouge, mylonite ... extending all over the surface of the fracture with the depths of the zones as provided in the deliveries (see figure 6.2).

The questions relative to the complexity of fractured zones is further reported in section 7.

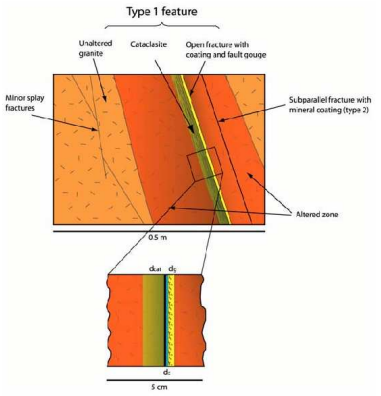

(a) Type 1, fault

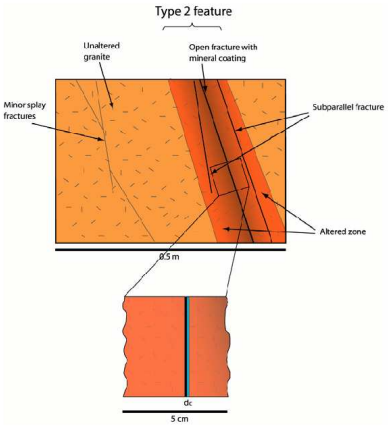

(b) Type 2, non faulted

Figure 3.1: Complexity of fractured zones.

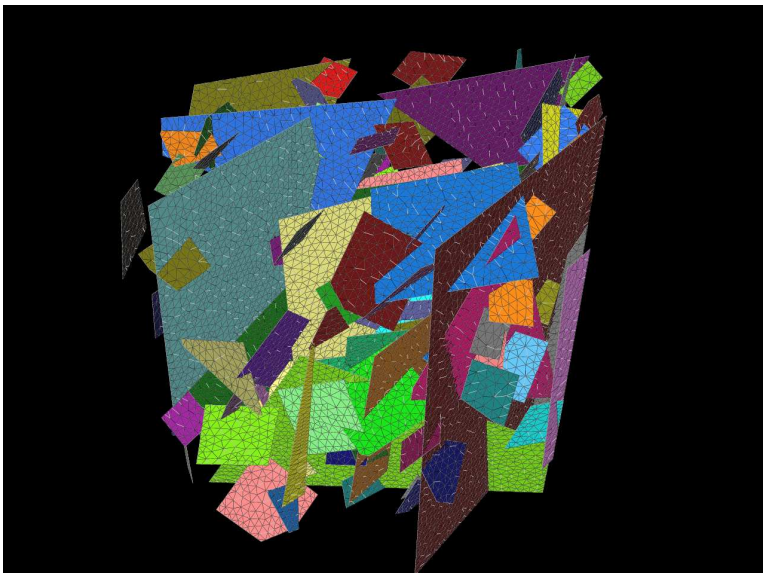

(a) Mesh of 150 fractures

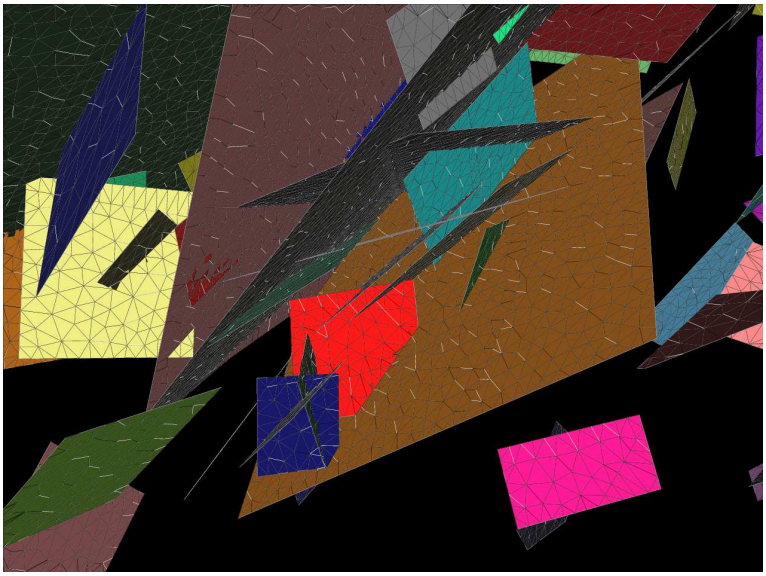

(b) Zoom on the 23D fracture (source term location)

Figure 3.2: 150 fractures Mesh.

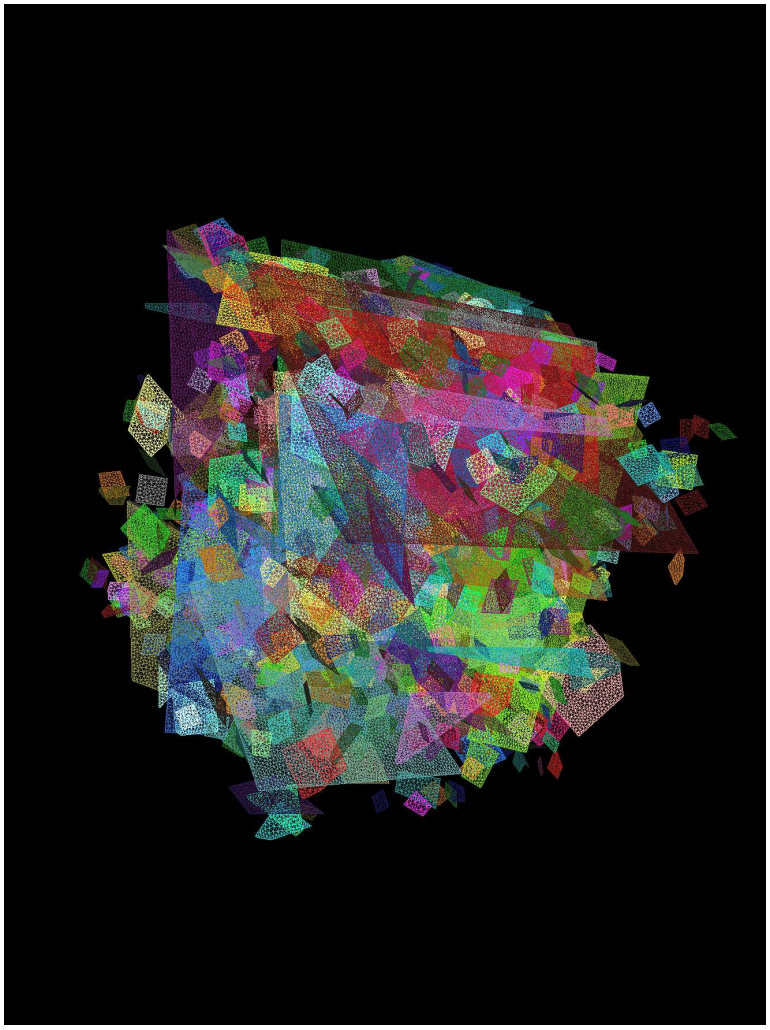

Figure 3.3: 1200 fracture mesh

3.3 Flow model

3.3.1 Processes considered

We model the flow only within the fractures. No flow is considered in the delimited matrix blocks. The flow problem is steady state corresponding to PA time scale conditions (gradient by 10^{-3} as from the deliveries).

3.3.2 Mathematical description

The models are implemented within Cast3M, a continuum code developed at CEA. We consider a classical Darcy equation for steady state flow:

$$\vec{\nabla}(\vec{U}) = Q,\ \vec{U} = -T\vec{\nabla}H \tag{3.1}$$

T stands for transmissivity, H for the head and $\vec{U}$ for Darcy velocity, Q to a source term.

3.3.3 Numerical implementation

The numerical scheme implemented in Cast3M code is MHFE (Mixed and Hybrid Finite Element scheme).

3.3.4 Parameters

Parameter values vary in space depending on the fracture properties. These are in agreement with the deliveries.

3.4 Transport model

3.4.1 Processes considered

We model transport with an Eulerian approach. Transport is advective, dispersive and diffusive in the fracture network. Linear sorption effects are included. Source is Dirac input or continuous source as from the deliveries. It is located in one of the fractures (Feature 23S).

Matrix zones are included in the model. They are accessed only by diffusion (no flow zones). Process considered are diffusion as well as linear sorption. Complexity of conducting features is simplified to the dominant type (full Type 1 or Type 2).

For sorbing tracers, linear sorption modeled by means of retention coefficients are considered for all units of the system: K_a for sorption on the fracture walls and K_d for sorption in the bulk of the rock (matrix).

3.4.2 Mathematical description

The model is implemented within Cast3M as well, providing a unique framework for flow and transport.

The mathematical Eulerian expression for the transport of concentration C_f limited to the fracture network follows (advection, dispersion, diffusion, linear sorption):

$$\omega_f R_f \frac{\partial C_f}{\partial t} = \vec{\nabla}(\overline{D}\vec{\nabla}C_f - \vec{U}C_f). \tag{3.2}$$

$\omega_f = 1$ fracture porosity, $R_f = R_a = 1 + (2K_a/e)$ surface retention coefficient (K_a distribution coefficient, e fracture aperture), $\vec{U}$ Darcy velocity,

$$\overline{D} = \begin{bmatrix} \alpha_L U + \omega D_{mol} & 0 & 0 \\ 0 & \alpha_T U + \omega D_{mol} & 0 \\ 0 & 0 & \alpha_T U + \omega D_{mol} \end{bmatrix}.$$

In the following we present the way matrix diffusion is treated. This first requires presentation of the general method. In a second step we show how this framework is sufficient to treat the full heterogeneity of Type 1 as well as Type 2 matrix zones.

The mathematical Eulerian expression for the diffusive transport of concentration C_m in the matrix follows:

$$\omega_m R_m \frac{\partial C_m}{\partial t} = \vec{\nabla}(\overline{D}_m \vec{\nabla} C_m). \tag{3.3}$$

ω_m porosity, $R_m = R_d = 1 + ((1-\omega)/\omega)\rho_S K_d$ bulk retention coefficient (ρ_S volumetric mass of solid, K_d bulk distr. coefficient), ($\vec{U} = \vec{0}$ since matrix zones are no flow units) $\overline{D}_m = \omega_m D_p$, equivalent diffusion coefficient (and D_p, pore diffusion coefficient).

Nevertheless, matrix blocks are not discretized so that the previous equation 3.3 is not solved numerically. Diffusion in matrix zones is solved considering analytical expressions. This is achieved considering 1D matrix geometries (1D infinite, 1D limited, 1D composite medium). This indeed corresponds to local orthogonal diffusion from the fracture to adjacent matrix zones. It can be proved that for local diffusion around fractures, 1D approach provides satisfactory results. Nevertheless, at first glance, this approach could be criticized since diffusion is expected to extend over large distances due to the PA time scale condition considered. The actual size and shape of matrix blocks should then be taken into account. But full discretization of matrix blocks was not attempted here. This would be difficult in terms of meshing of highly distorted 3D geometries (meshes with large length ratios) and would require a dedicated mesh generator. Efficient simulation of diffusive transport would in addition require refined meshing close to the fracture matrix interfaces (where transient concentration gradients are important and Fourier ratios

should be honored). This would result in very large computer costs. Nevertheless, studies conducted about the geometry of main transport conductors from the source to the outlet showed that these boil down to two main paths, both being mainly limited to fractures in series. The distance between those main transport paths proved a posteriori larger than twice the estimated penetration depth in the matrix. So, for the semi-synthetic block treated and for the parameter provided as well as head gradient, this simple approach including matrix diffusion as a local 1D diffusion phenomenon is assumed pertinent.

Solutions to 1D diffusion processes can be found in [*Carslaw and Jaeger 46*]. These rely upon theory of Laplace transforms or Green functions. The option chosen consists in computing the total mass present in 1D system considering the history of concentration present in the fracture at the inlet to it (mathematically speaking a convolution with the output to a Dirac). From the point of view of the fracture, a source term is introduced in fracture transport equation (Eq. 3.2) expressing the loss of mass toward the matrix zones by a flux term: corrected difference between masses in the matrix at present time and previous time step divided by time step (see equation 3.4). Mass difference between two successive time steps expresses as a linear combination involving the whole history of concentrations in the fracture (at the inlet of the 1D matrix bar). For a given time step, this history involves concentration at former time steps which are already calculated (explicit), and the concentration at present time step (being calculated) appears as well (implicit term). Reorganizing the terms of the equation leads to an explicit source term (involving concentration at former time steps) and a modified term for concentration time derivative on the left side of the equation (implicit part). The final equation is fully implicit expression (see equation 3.5) involves a modified porosity or retardation coefficient (left side) and an additional source term (right side). Such an expression can be easily handled within Cast3M code. Constraints in terms of time step increments appear for large matrix diffusion effects. Indeed for large retardation due to matrix diffusion, time steps should not exceed the limit provided on equation 3.6.

$$\omega \frac{C_f^t - C_f^{t-\delta t}}{\delta t} + \vec{\nabla}(-D\nabla C^t + \vec{U}C^t) = -K\frac{C_m^t - C_m^{t-\delta t}}{\delta t} \tag{3.4}$$

C_f^t, fracture concentration, t current time, δt time discretization, C_m^t, mean concentration in 1D matrix unit adjacent to the fracture location considered. C_m^t expresses as a function of C_f^t history: linear function of C_f^t, $C_f^{t-\delta t}$, $C_f^{t-2\delta t}$ ..., $C_f^{t_0}$. For a 1D bar of length L, Equation 3.4 can be written as follows:

$$\begin{array}{l} (\omega \ + \ \alpha_0 \omega_{Ma} \frac{2L}{e^2}) \frac{C^t - C^{t-\delta t}}{\delta t} + \vec{\nabla}(-D\nabla C^t + \vec{U}C^t) \\ = \ -\omega_{Ma} \ \frac{2L}{e^2} \ \frac{Fct(C^0,\ldots,C^t) - Fct(C^0,\ldots,C^{t-\delta t})}{\delta t} \end{array} \tag{3.5}$$

Although former equation is formally fully implicit, a criterion for convergence of the simulation is required and takes the following form:

$$\frac{\omega_m \sqrt{2 D_m R_m}}{\omega_f e R_f} \sqrt{\delta t} < 1 \tag{3.6}$$

Practically speaking three 1D solutions were implemented for the present purposes: infinite domain (with classical mass increase as square root of time), limited diffusion, composite domain (first limited, second infinite). We illustrate the solution in terms of mean concentration in the matrix bar ($\overline{C_m}$) in equation 3.7 (Imposed C_0 at time $t_0 = 0$, L length of the bar) Associated equivalent retardation coefficient is:

$$\overline{C_m}(t) = C_0(1 - \frac{8}{\Pi^2}\sum_{n=0}^{\infty}\frac{1}{(2n+1)^2}exp(\frac{-D_m(2n+1)^2\Pi^2 t}{4L^2})) \tag{3.7}$$

The next step in the presentation of our method consists in showing that this framework is adequate to treat the full heterogeneity of Type 1 an Type 2 matrix zones. Indeed, our approach considers maximally a composite medium with a heterogeneity of two matrix properties whereas Type 1 involves 5 subunits and Type 2 involves 3 subunits.

Nevertheless, for PA time scales, full modeling of Type 1 system is not necessary as was demonstrated in [*Grenier 03*] for the so called simplified PA model. Indeed, for slow transfers in the fracture, thin high diffusion zones in the vicinity of the fracture directly follow the concentration evolution in the fracture. They provide a larger volume that can be represented as pseudo retardation coefficient or pseudo K_a. This is suggested for instance in [*Dershowitz et al. 03*] to treat fracture coating as equivalent pseudo K_a.

We studied the transport regimes for Type 1 and Type 2 fracture systems by meshing a single fracture system for a total length by 20 m, transmissivities and apertures characteristic of main features. Results show that for the low head gradient, all higher diffusion zones can be equivalently treated by a retardation coefficient expressing as in equation 6.1. For Type 1 configuration, summation is carried upon properties of fracture coating, gouge, mylonite, for Type 2, summation is limited to fracture coating only. More details are provided in [*Grenier 03*].

$$R' = 1 + \frac{1}{b}\sum_i \omega_i d_i R_i. \tag{3.8}$$

R_i is the retardation coefficient in the matrix zone i, d_i its thickness, ω_i its porosity and b the fracture aperture. This coefficient is to be calculated for each tracer (R_i depends on the tracer and the type of matrix, $R_i = 1 + \rho\frac{1-\omega_i}{\omega_i}K_d$) and for each fracture (aperture dependent).

As a conclusion, the simulation framework proposed here meets the needs of Task6E since higher diffusion zones in the vicinity of the fracture are homogenized to an equivalent R' coefficient while the remaining altered and non altered rock units are included within the semi analytical approach presented previously considering the composite medium case.

3.4.3 Numerical implementation

The numerical scheme considered here is MHFE (Mixed Hybrid Finite Element scheme). It has the advantage of providing good mass conservation even for highly heterogeneous media.

Time discretization scheme is fully implicit.

The spatial discretization was varied from 1 meter up to 6 meters. We'll see, in Sec. 5.1.1, that the results are converged for a 3 meter discretization (less than 5 % of error).

Average mesh length in the fractures is close to 2 m along the fracture planes. The elements are all 2D triangles. The total amount of cells is about 150 000.

3.4.4 Parameters

The parameters considered here are first parameters associated with the fractures: transmissivity, apertures, complexity, dominant type ... We strictly considered the values provided in the deliveries.

Parameters associated with fractured zones Type 1 and 2 were chosen in agreement with the deliveries and are reproduced on Table 3.1.

Parameters associated with properties of sorbing tracers are provided on Table 3.1.

Task6E	Fracture	Gouge	Cataclasite	Altered Rock	Non Alt. R.
Extent		$5mm$	$2cm$	$20cm$	-
Porosity	1	20%	1%	0.6%	0.3%
Pore diffusion coef. (m^2/s)	10^{-9}	6.10^{-10}	10^{-10}	$7.8\,10^{-11}$	$5.3\,10^{-11}$
Effective diffusion coef. (m^2/s)	10^{-9}	10^{-10}	10^{-12}	$5.\,10^{-13}$	$1.5\,10^{-13}$
Iodine $K_a(m)$, $K_d(m^3/kg)$	Fr. Coat.	$0.$	$0.$	$0.$	$0.$
Cesium $K_a(m)$, $K_d(m^3/kg)$	Fr. Coat.	$1.6\,10{-}1$	$1.5\,10^{-2}$	$2.0\,10^{-2}$	$1.0\,10^{-2}$
Americium $K_a(m)$, $K_d(m^3/kg)$	Fr. Coat.	0.5	0.5	0.5	0.5

Table 3.1: Parameter set for different matrix zones from the deliveries. Fracture sorption properties correspond to the presence of fracture coating (porosity by 5%, extent by $5mm$, $K_d = 5.2\,10^{-2}$ for Cesium and $K_d = 0.5$ for Americium).

Chapter 4

Task 6D

4.1 Introduction

We follow here the same line as for previous steps of Task6 as outlined previously. The system geometry is here (Task 6D) clearly more complex (than Task6A) involving at least 4 deterministic feature sections (features 20 to 23), the associated transport porosities as well as adjacent matrix zones. The flow in these units is more complex as well than for Task6A since the major flow line connecting injection and pumping wells is expected to be sensitive to inflows at fracture intersections. In consequence we limit our calibration ambitions to a simple system involving the former 4 features as well as an homogeneous matrix zone along the fracture. We consider that further complexity can't be constrained from the tracer tests. We confirm below that this system is successful as it properly matches the breakthrough curves provided. As a consequence, some information provided in the task deliveries is not considered in our model. This encloses fracture complexity (type 1 and 2 and complexity factors) or heterogeneity of the matrix zones.

Moreover we do not take the information related with back ground fracturing into account. These features are potentially important since they could be responsible for multiple flow paths between the input and output wells. This issue is not addressed here. Nevertheless, the full complexity of the system will have to be considered for the future task6E. In view of the prediction phase, the importance of the different sub units of the system will have to be identified. The treatment of back ground fracturing as well as fracture complexity belongs to it. Moreover we do not work here with two systems as suggested in the specifications, a detailed one (SC) and a more simpler one (PA) since we do not consider possible identifying more features than the one contained in our simple model (to be referred as PA like) due to the limited constraining power of the experimental tests.

In the following, we present the models considered in the present study. We consider a first model at 200 m scale involving all 11 deterministic features. This model provides boundary conditions for the second model involving features 20 to 23 as well as matrix

zones in the vicinity of the fractures. These modeling approaches are continuous considering the fractures as planes. We largely use the parameter set provided in the task specifications.
Then we present the calibration of the 4 fracture system in order to match the breakthrough curves provided. In doing so we do not change the parameters associated with flow properties from the ones provided in the specifications. So no calibration of flow properties is considered here. The calibration is conducted on transport parameters for a fixed flow line (four fracture transport apertures, homogeneous matrix properties, associated sorption properties for sorbing tracers). Calibration is carried on visually on breakthrough curves associated with the 3 tracers, looking for a single deterministic optimal solution in terms of fracture transport aperture and matrix porosity as well as diffusion coefficient.
We finally study the sensitivity of the system around this optimal solution to identify the range of precision for the different parameters (associated to advective properties or matrix zones).
We conclude and discuss our results.

4.2 Modeling strategy

4.2.1 Model, implementation and data selection for Task6D

The modeling strategy consists in building a model retaining the most striking features that can possibly be identified from Test C2 experiment. For this, we consider a local model involving 4 deterministic fractures (Feature 20 to 23) as well as adjacent matrix zones. Such a simple model allows for a large number of simulations for calibration as well as sensitivity analysis purposes. The flow boundary conditions for this model are obtained from a larger scale 200 m model run with the boundary conditions provided in the deliveries.

As presented above and confirmed below, we simply aim here at providing a single 'optimal' solution for the problem. Additional sensitivity analysis provide insights into the quality associated with this solution. In line with conclusions for previous Task6A and 6B, it appears that little information is gained from the tracer test. The constraining power of these tracer tests is too limited to practically allow for identification of pertinent features. As a consequence, the present work is more a positive evaluation of the internal coherence of the data provided (geometrical features, parameter sets, breakthrough curves) rather than an exercise constraining the properties of the system on the basis of the tracer tests. More simplified models than the 4 feature system should not be considered for sake of realism.

The data selection is consequently limited to simple features. These can be described as average properties (fracture transmissivity, apertures, matrix properties). We remain close to the datasets provided in the deliveries. Fracture zones complexity is not addressed here since tracer tests allow for identification of average matrix properties and not detailed

structures. Back ground fractures are not considered here for simplicity but could possibly play a role in providing alternative advective travel paths. Nevertheless, the small scale features provided in the semi synthetic model are not deterministically identified. So, strictly speaking, the influence of back ground fracturing should better be addressed in a stochastic framework or modeled by an equivalent continuum for instance.

4.2.2 Implementation of the Task6C semi-synthetic hydro structural model

The major features of the approach follow:

- We consider a deterministic approach. Fractures are basically modeled as 2D planes. We restrain our work to 11 deterministic fractures for a 200 m scale model. For the calibration phase we consider a smaller scale model involving Features 20 to 23 as well as neighboring matrix zones. So, the modeling approach is conducted in two steps involving two models. The first larger scale model provides flow boundary conditions for the second.

- No matrix blocks are included in the larger scale model. Limited matrix diffusion zones are included in the smaller scale model. These units are modeled as 3D zones between the fracture and a plane parallel to the fractures at centimetric distance.

- The models are implemented within Cast3M, a continuous code. Permanent calculations are conducted for Darcy flow simulation by MHFE (Mixed Hybrid Finite Element scheme) and for transient Eulerian transport by FV (Finite volume scheme).

- No calibration is considered for the flow problem (parameters from the deliveries are considered. Calibration is conducted on the local model including the parameters associated with transport properties (fracture transport apertures, matrix porosity and diffusion coefficients, sorption parameters). We consider no flow in the matrix blocks.

The characteristics of these models are clarified below in sections 4.2.3 for the 200m scale model and 4.2.4 for the local model considering features 20 to 23.

Processes considered

We model flow within the fractures only. No flow is considered in the matrix blocks. The flow problem is permanent corresponding to pumping conditions.

We model transport in all the parts of the modeled systems. We consider advective and dispersive transport in the fractures and diffusive transport in the matrix blocks. For

sorbing tracers, linear sorption by means of retention coefficients are considered for all units of the system: K_a for sorption on the fracture walls and K_d for sorption in the bulk of the rock.

The smeared fracture approach considered for the 200 m scale geometry is detailed below (see section 4.2.3).

Mathematical description and numerical implementation

Globally, the equations solved remain the same whatever the approach (smeared fracture for the 200 m scale model or explicit meshing of the units for the local 4 fracture model). We consider a classical Darcy equation for flow and the transport equation provided below. Parameter values vary in space depending on the fracture properties.

Flow equation (permanent):

$$\vec{\nabla}(\vec{U}) = Q,\ \vec{U} = -K\vec{\nabla}H \tag{4.1}$$

K stands for the equivalent permeabilities associated with the smeared fracture approach. H for the head and $\vec{U}$ for Darcy velocity, Q for a source term.

Transport equation:

$$\omega R\frac{\partial C}{\partial t} = \vec{\nabla}(\overline{D}\vec{\nabla}C - \vec{U}C). \tag{4.2}$$

The parameters considered vary in space (take different values for fracture and matrix zones):

fracture :
- $\omega = 1$ fracture porosity,
- $R = R_a = 1 + (2K_a/e)$ surface retention coefficient (K_a distribution coefficient, e fracture aperture),
- $\vec{U}$ Darcy velocity,
- $\overline{D} = \begin{bmatrix} \alpha_L U + \omega D_{mol} & 0 & 0 \\ 0 & \alpha_T U + \omega D_{mol} & 0 \\ 0 & 0 & \alpha_T U + \omega D_{mol} \end{bmatrix}$.

matrix :
- $\omega = \omega_m$ porosity,
- $R = R_d = 1 + ((1-\omega)/\omega)\rho_S K_d$ bulk retention coefficient (ρ_S volumetric mass of solid, K_d bulk distr. coefficient),
- $\vec{U} = \vec{0}$,
- $\overline{D} = \omega D_p$, equivalent diffusion coefficient (and Dp, pore diffusion coefficient).

4.2.3 200 m scale model for flow only

We detail here the features associated with the first geometry considered, the one associated with the 200 m scale. This geometry is considered for flow simulations only and provides boundary conditions for the more local 4 fracture flow model. Transport simulations for calibration are conducted on the 4 fracture local system.

Geometrical description

We consider the 11 deterministic fractures provided in the task specifications. They are represented on figure 4.1(a). The resulting smeared fracture model is represented on figure 4.1(b). The matrix blocks are excavated, they are considered as no flow units. Matrix zones are not considered in this model.

Mathematical description and numerical implementation

The mathematical description of the model considered for simulation of the flow problem were presented previously (section 4.2.2). The Darcy problem is simulated for permanent pumping conditions within our Cast3M code based on continuous approach and a Mixed and Hybrid Finite Element scheme.

We consider here 11 deterministic fractures. These are treated as 2D planar objects but are modeled within a smeared fracture approach. This is due to the fact that we do not have the simulation tools to model transfers in such an explicitly meshed 11 fracture geometry. Such tools are presently still under development. The smeared fracture approach is detailed below.

Within a smeared fracture approach, these fractures as well as their intersections and matrix blocks are not explicitly meshed but are represented on a regular grid as a heterogeneous continuous field of properties (permeability, porosity, dispersion coefficient, matrix diffusion coefficient ...). One may refer to [*Fourno et al. 03*] for a presentation of the approach as well as a presentation of the performances of the approach. So far, this approach has been intensively tested on 2D problems and proved sufficiently precise to account for flow and transport within a fractured block provided the mesh size is sufficiently small and the transitory transfer regimes are not too contrasted.

We apply this approach here to a 3D case consisting of the 11 deterministic features mentioned previously. The size of the grid was optimized to account for the details of the geometrical system while providing acceptable computational time. The calculation consists of a permanent flow problem so that none of the difficulties associated with mesh size as compared with discretization time is pertinent. Nevertheless a smeared approach requires providing proper equivalent permeabilities for each mesh corresponding to the presence of a fracture. The expressions for these parameters are provided of 2D cases in [*Fourno et al. 03*]. The rule is that total flux through each fracture taken separately

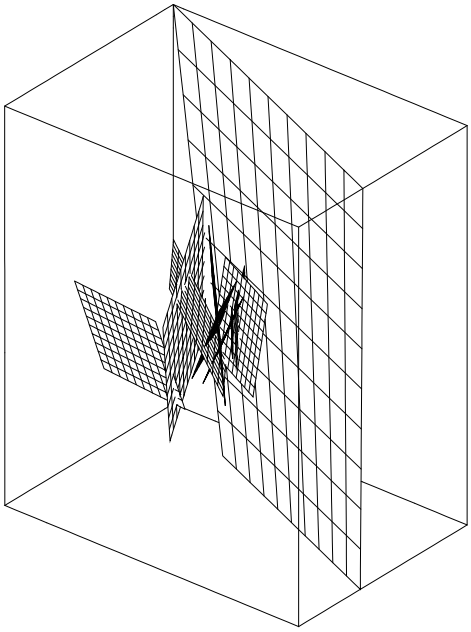

(a) Fracture planes for the 11 deterministic features

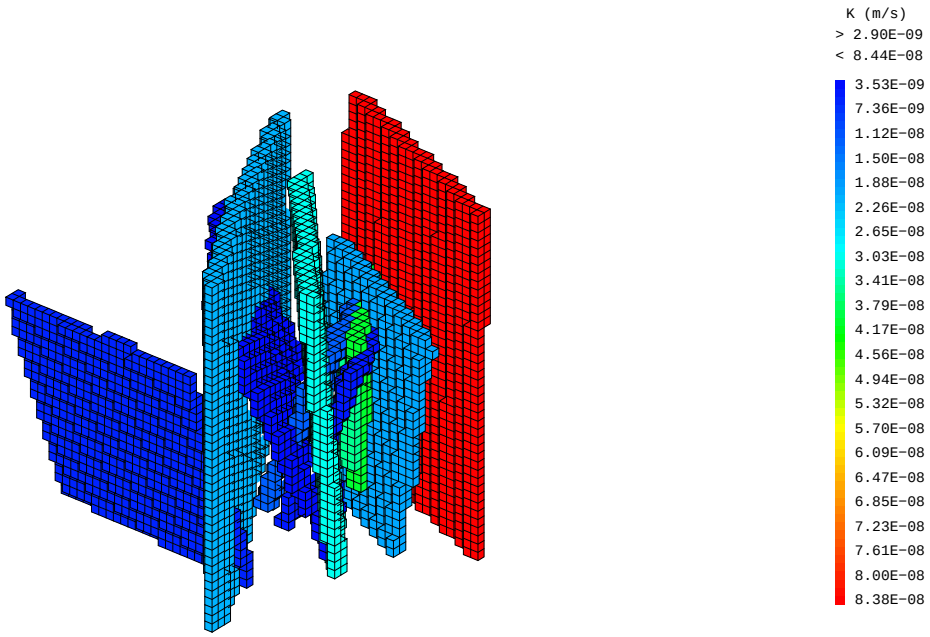

(b) Permeability fi eld associated with the 11 fracture system for a smeared fracture approach

Figure 4.1: Geometrical features and permeability field for the 200 m scale system modeled

should be matched. For a unique transmissivity within a single feature, the equivalent permeability along the smeared fracture representation of the feature (stair case like) is constant. Mathematical developments associated with the MHFE scheme considered in our code show that:

1. The permeability value associated with a feature depends upon its (i) transmissivity T, (ii) the smeared fracture grid mesh size δx and (iii) the slope of the fracture as compared with the regular grid main directions.

2. Considering a fracture parallel to one of the grid directions, the permeability correction is expressed in terms of the represented fracture aperture divided by the by the regular mesh grid size. Expressed in terms of transmissivity as provided in the data deliveries: $K^{SF} = T/\delta x$ (K^{SF} smeared fracture permeability, T measured feature transmissivity, δx spatial discretization (mesh size).

In addition, transmissivities at fracture intersections are chosen as the larger of all present at this location. One should as well stress that the approach is not like Oda tensor theory since the mesh size is chosen here small enough as compared with the fracture extensions.

The issues associated with smeared fracture approach as related with 3D problems are being currently studied. We consider here a rough approximation for the permeability values by correcting all transmissivities as for a fracture parallel with the main directions of the regular grid. This leads to estimated maximal 20% error in terms of fracture permeability. The worst case is met for slopes by 45 degrees. This situation is not met for a majority of fractures since most are sub vertical. Ongoing work will help refining the definition of equivalent properties for 3D cases.

The given boundary conditions are applied onto the system presented. Pumping test is simulated considering a source term by $3.25\,10^{-5}\,m^3/s$. The boundary conditions imposed are provided on the former coarser regular mesh on figure 7.4. For our finer mesh, the nearest location was chosen to apply the prescribed head value.

Parameters

The parameters considered here are transmissivity values. These are obtained from the task specifications and summed up below in table 4.1. The resulting permeability field for the smeared fracture approach is presented on figure 4.1(b). These permeability values correspond to the transmissivity values divided by the size of the mesh as explained in the preceding section. The spatial discretization is 4.76 m. The total initial regular volume is divided into 42^3 regular meshes.

Simulation results

Illustration for the results of the flow simulation are provided on Figures 4.3 for the whole system as well as reduced to the 4 fractures concerned by the tracer test on Figures 4.4.

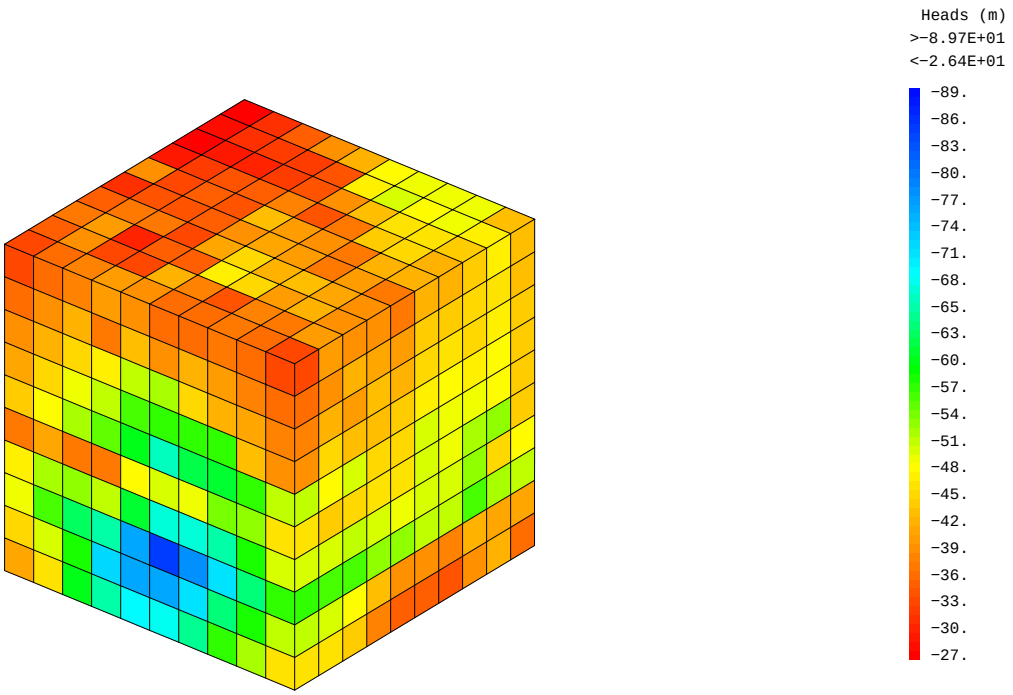

(a) First view of the boundary conditions

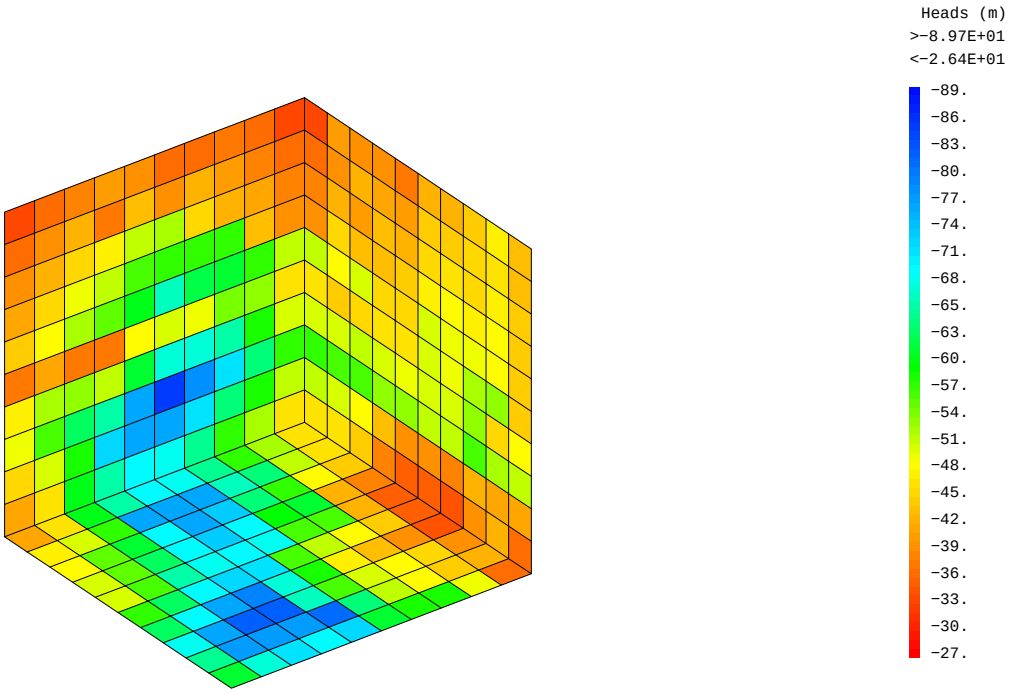

(b) Second view of the boundary conditions

Figure 4.2: Boundary conditions in heads applied on the system (as provided in the data deliveries)

Structure Name	Transmissivity (m^2/s)	Aperture (m)
5	$4.020\ 10^{-7}$	$2.917\ 10^{-4}$
6	$1.910\ 10^{-7}$	$2.010\ 10^{-4}$
7	$9.760\ 10^{-8}$	$1.437\ 10^{-4}$
10	$2.980\ 10^{-8}$	$7.941\ 10^{-5}$
13	$1.380\ 10^{-8}$	$5.404\ 10^{-5}$
19	$1.020\ 10^{-7}$	$1.469\ 10^{-4}$
20	$1.430\ 10^{-7}$	$1.740\ 10^{-4}$
21	$6.020\ 10^{-8}$	$1.129\ 10^{-4}$
22	$2.190\ 10^{-8}$	$6.807\ 10^{-5}$
23	$1.660\ 10^{-7}$	$1.874\ 10^{-4}$
24	$8.510\ 10^{-8}$	$1.342\ 10^{-4}$

Table 4.1: Transmissivity values for the 11 deterministic features modeled (according to data deliveries)

The drawdown at the well is -243 m for the boundary conditions provided (Fig. 7.4).

No model calibration was conducted for the flow model. The values considered in the simulation are the ones provided in the deliveries (see table 4.1).

4.2.4 Local model for flow and transport

The rest of the work is conducted on a simpler geometry. We model four fractures (feature 20 to 23) involved along the path of the plume. Adjacent matrix zones accessed by diffusion are included in the model. We neglect herewith the influence of back ground fracturing as providing alternative pathways between injection and pumping wells.

We do not consider here a smeared fracture approach to model transport in these units. This is due to the fact that this approach has not been sufficiently validated at present for 3D cases. Moreover, discretization of matrix zones should be fine for such limited matrix diffusion regimes corresponding to quick forced flow regimes. Indeed a classical smeared fracture approach does not allow for precise modeling of transfer phenomena within two subunits showing very contrasted transport regime. One may refer to [*Fourno et al. 03*] for the range of validity of the approach. Slower flow regimes leading to larger fracture matrix interactions are better represented by a smeared fracture approach. This is simply due to numerical constraints for a single mesh size and time discretization for the whole domain.

No calibration for the flow parameters is attempted here (transmissivities for Features 20 to 23) in coherence with the former model operating at 200 m scale. Calibration is conducted on transport features involving the four fracture apertures and matrix properties. The latter correspond to a unique porosity and matrix diffusion coefficient value. Indeed as mentioned before, results from previous tasks ([*Grenier 03*]) show that tracer test only

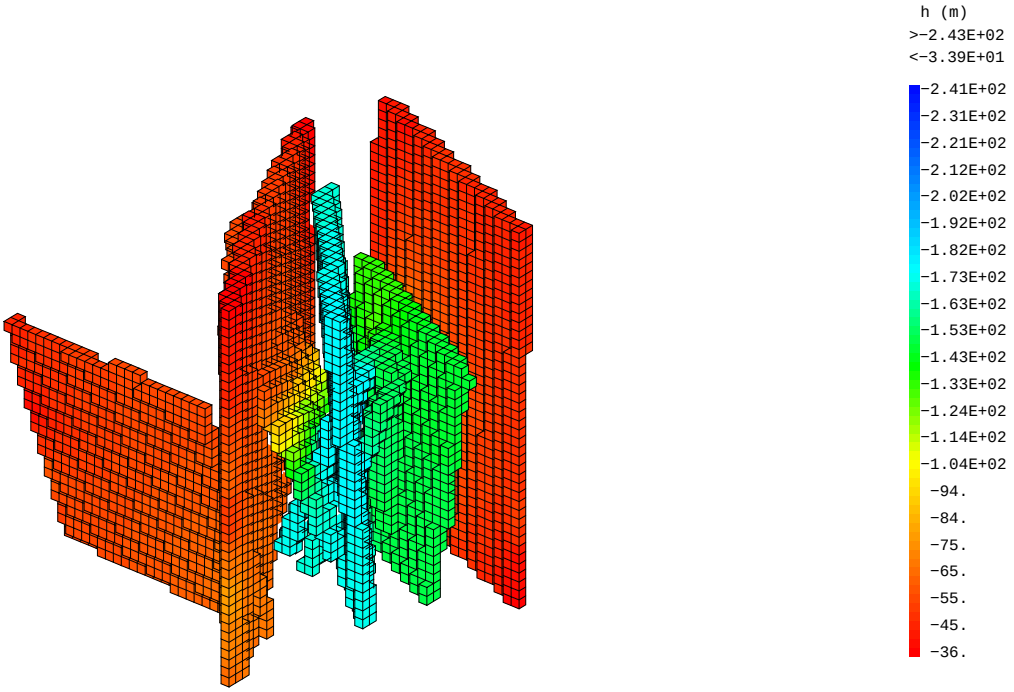

(a) Head fi eld (m)

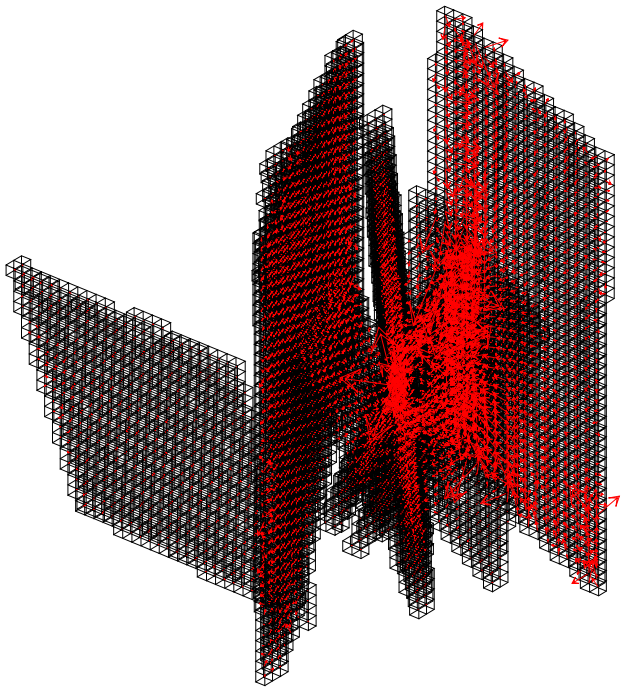

(b) Velocity fi eld

Figure 4.3: Flow model for the 200 m scale system, 11 deterministic features

(a) Head fi eld (reduced system, 4 features 20 to 23)

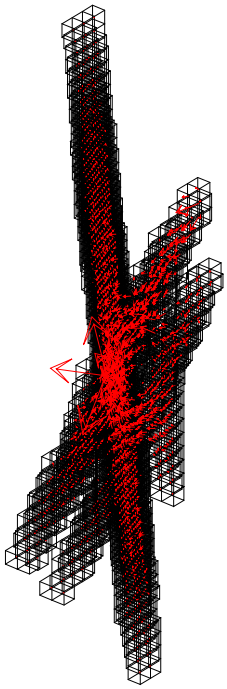

(b) Velocities

Figure 4.4: Flow model for the 200 m scale system reduced on fractures 20 to 23

allow for identification of averaged matrix properties. This is what the single matrix diffusion coefficient and matrix porosity represents in the present calibration exercise.

Geometrical description

Fractures 20, 21, 22, 23 are explicitly meshed as well as matrix zones in the vicinity of the fractures. All these units are modeled in 3D. One may refer to figure 4.5.

The injection well is connected to pumping well continuously along portions of features 20 to 23. Fracture portions that do not contain the travel path are not meshed. The water inputs associated with these subunits are accounted for as source terms at the meshed fracture intersections. These water inflows are obtained from the 200 m model and accounted for in the present model as a source term. Head boundary conditions at the limits of the system are obtained from the previous 200 m model.

Fractures are modeled here as the planes provided in the specifications for which an aperture is associated so that they are meshed as 3D objects. Adjacent matrix zones are enclosed in the model. Average mesh length in the fractures is close to 1 m along the fracture planes. The elements are all 3D. The total amount of cells is 10 000 including meshes in the matrix. For calibration purposes (large number of simulations) we work on the upper half of the system allowing for reduction of computer costs for each simulation. The consequences in terms of loss of precision are minor.

Processes considered

We consider flow in the fractures, no flow in the adjacent matrix zones. Transport in the fractures considering advection, dispersion, linear sorption. Transport in the matrix by diffusion and considering linear sorption.

Mathematical description and numerical implementation

Flow is solved in all cases with a continuous approach and considering a Mixed and Hybrid Finite Element scheme available in Cast3M. We don't consider here for transport a MHFE scheme but a more recently developed Finite Volume scheme providing similar precision results for lower computer costs. One may refer to former section 4.2.2 for more information.

Parameters

Flow parameters are considered as in the deliveries. Transport parameter values are calibrated against the breakthrough curves provided. This lead to changes in the fracture apertures (provided in table 4.2) and matrix properties as well as sorption properties (provided in table 4.3).

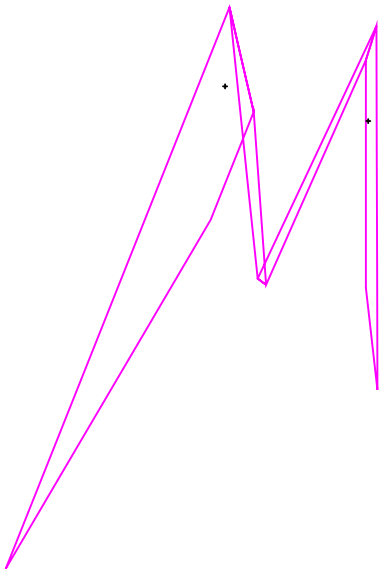

(a) Fracture planes for the 4 features (20 to 23)

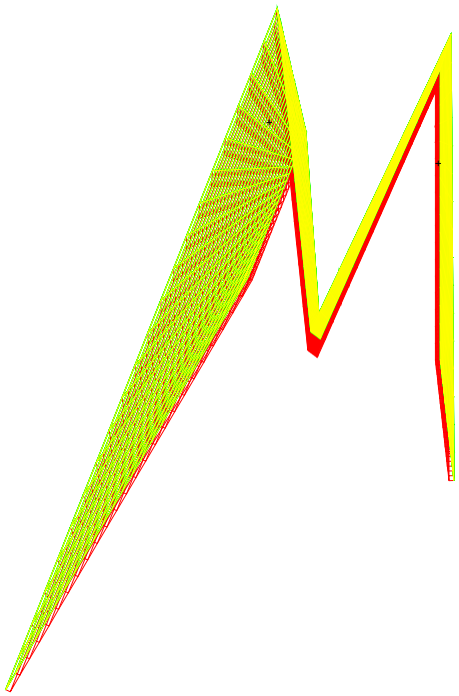

(b) Mesh for the 4 fracture system (features 20 to 23 and matrix diffusion zones)

Figure 4.5: Geometrical features of the 4 fracture system modeled

Simulation results

The head field, velocity field as well as the advection path are represented on figures 4.6. **The length of the advection path is** $77.65m$. The depth of the matrix zone meshed is centimetric. As mentioned previously, flow features are not calibrated here so that this travel path is not modified during calibration.

The fracture transport apertures were modified to account for peak breakthrough curves arrival time. Fracture apertures for features 23 and 22 were multiplied by 2.5 from the values provided in the data deliveries (see table 4.2). Calibration procedure includes matrix properties. We consider here a unique parameter value in terms of diffusion coefficient as well as matrix porosity. The detail for all matrix zones is not modeled. Calibrated sorption properties are included in table 4.3 and 4.5. Here, the values associated with Ka and Ra include the effect of fracture coating, a diffusion zone which is not explicitly modeled but accounted for by means of an equivalent sorption coefficient (see [*Elert et Selroos 02*]).

The calibration procedure as well as considerations about the complexity of the system, sensitivity of the system to the various parameters are detailed in the next section.

Structure Name	Transmissivity (m^2/s)	Aperture (m) initial	Aperture (m) calibrated
20	$1.430\ 10^{-7}$	$1.740\ 10^{-4}$	id.
21	$6.020\ 10^{-8}$	$1.129\ 10^{-4}$	id.
22	$2.190\ 10^{-8}$	$6.807\ 10^{-5}$	(x 2.5)
23	$1.660\ 10^{-7}$	$1.874\ 10^{-4}$	(x 2.5)

Table 4.2: Transmissivity values as well as fracture apertures associated with the 4 deterministic features modeled (according to data deliveries and as calibrated)

Matrix properties	Pore diffusion coeffi cient (m^2/s)	Porosity
Calibration	2.10^{-10}	2%

Table 4.3: Matrix properties as calibrated

4.2.5 Model calibration

We conducted calibration of the model aiming at a single optimal (deterministic) dataset. As mentioned above the parameters considered involve the 4 fracture apertures corresponding to features 20 to 23 as well as a unique matrix diffusion coefficient and matrix porosity. Matrix diffusion depth was chosen large enough so that the plume would not meet the no diffusive flux boundary condition. Additional parameter are considered for sorbing tracers. These involve the corresponding K_d values.

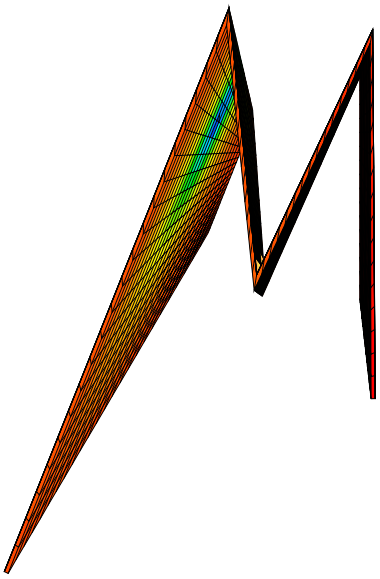

(a) Head fi eld

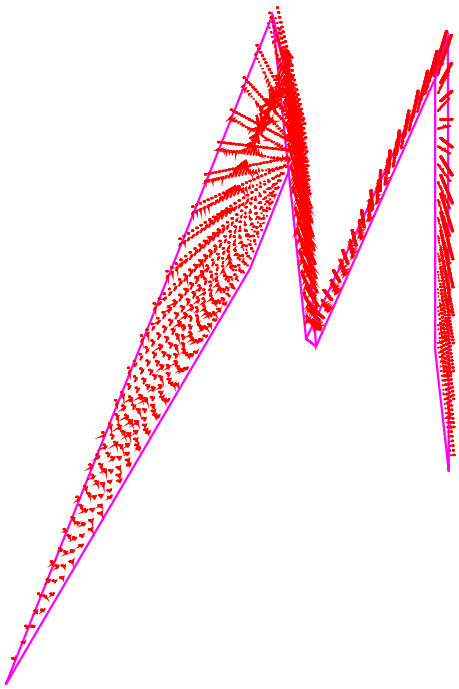

(b) Darcy velocity fi eld 4 fracture system (features 20 to 23)

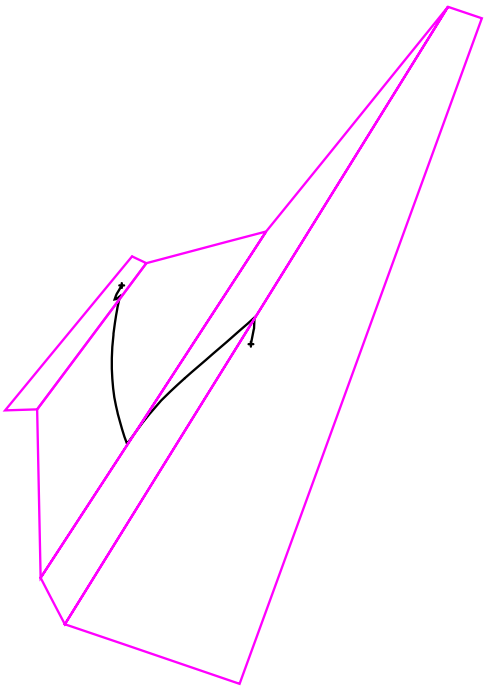

(c) Advective path between injection and pumping well

Figure 4.6: Flow features for the 4 fracture system (features 20 to 23)

Task6D	Fracture	Gouge	Fr. Coating	Mylonite	Altered Rock	Non Alt. R.
Extent		$5mm$	$0.5mm$	$2cm$	$20cm$	$20cm$
Porosity	1	15%	5%	1%	0.6%	0.3%
Pore diffusion coeffi cient (m^2/s)	10^{-9}	3.10^{-10}	2.10^{-10}	10^{-10}	8.10^{-10}	5.10^{-10}
Strontium $K_a(m)$, $K_d(m^3/kg)$	5.10^{-4}	$7.1\,10^{-4}$	$2.3\,10^{-4}$	$6.7\,10^{-5}$	6.10^{-5}	6.10^{-5}
Strontium R_a or R_d	1.5	11.8	12.8	180	26.8	53.8
Cobalt $K_a(m)$, $K_d(m^3/kg)$	8.10^{-3}	8.10^{-4}	8.10^{-4}	8.10^{-4}	8.10^{-4}	8.10^{-4}
Cobalt R_a or R_d	9	13.2	42	215	358	718
Technetium $K_a(m)$, $K_d(m^3/kg)$	0.2	0.2	0.2	0.2	0.2	0.2
Technetium R_a or R_d	201	3061	10261	53461	89460	$1.8\,10^5$
Americium $K_a(m)$, $K_d(m^3/kg)$	0.5	0.5	0.5	0.5	0.5	0.5
Americium R_a or R_d	501	7651	25651	1.310^5	$2.2\,10^5$	$4.5\,10^5$

Table 4.4: Parameter set for different matrix zones from the deliveries

Sorption parameters	K_a surface	R_a surface	K_d bulk	R_d bulk
Rhenium	2.510^{-5}	1.33	0	1
Calcium	1.7310^{-4}	3.31	1.2510^{-4}	17.5
Cesium	3.3810^{-2}	451.33	2.0010^{-2}	2647.0
Radium	1.7610^{-2}	235.33	1.3010^{-2}	1720.9
Technetium	0.27	3601.3	0.2	26461.
Americium	0.68	9001.3	0.5	66151.

Table 4.5: Sorption coefficients (as in final simulations). Ka and Ra account for the presence of fracture coating as well as sorbing effects in this unit.

The quality of fit was estimated visually on the breakthrough curves for the different tracer considered. Roughly, calibration procedure starts from the non sorbing case for which the transport parameters are first calibrated. The breakthrough curves for the sorbing tracers allow for identification of sorbing properties. Overall coherence is researched over all tracer test by conducting different runs for all 3 tracers. The different steps are conducted considering the observed sensitivity of the system to the different parameters and taking the former Task 6A experience into account. No systematic calibration procedure is nevertheless conducted, overall sensitivity to the different parameters is not quantitatively estimated. The initial guess corresponds to the dataset provided in the deliveries.

The results of the calibration are provided on figures 4.7 as well as on tables 4.2, 4.3 and 4.5.

Following comments are necessary:

- The quality of the fit is quite acceptable.
- The breakthrough curve corresponding to Cesium is scarce and can be fitted in various ways. This tracer does not strongly constrain the calibration.

- The values of the calibrated parameters are acceptable. They correspond to properties close to those associated with gouge material though weaker. This is fully in agreement with the fact that tracer tests averages on the properties of the materials in the vicinity of the flow path and providing the larger diffusion coefficient as well as porosities. The values of the parameters corresponding to the different matrix zones are recalled on table 4.4.

4.3 Results

Our approach consists in searching for a unique dataset calibrating the tracer test experiments. So performance measures are provided for this unique situation. Sensitivity analysis is provided later down.

Performance measures correspond to different boundary conditions :

- Dirac input : we consider here the release of a unit mass at the initial simulation time. The mass is located in the mesh corresponding to the input well.
- Real input.

We show for these boundary conditions :

- Breakthrough curves (for both Dirac and real injection conditions). These correspond to the total mass leaving the system.
- Maximum release rate for Dirac input.
- Breakthrough time recovery (5, 50 and 95 percents of the injected mass).

The graphs are provided as required in the specifications : in log-log scale in a frame 20cm * 12cm.

For each tracer, we associate a color as follows:

- Blue for Rhenium/Iodine
- Red for Calcium
- Green for Cesium
- Yellow for Radium
- Cyan for Technetium
- Magenta for Americium

The parameter data set is provided along tables 4.2, 4.3, 4.5.

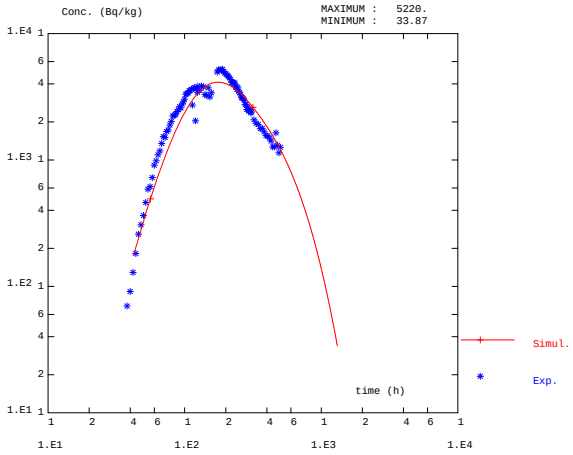

(a) Rhenium

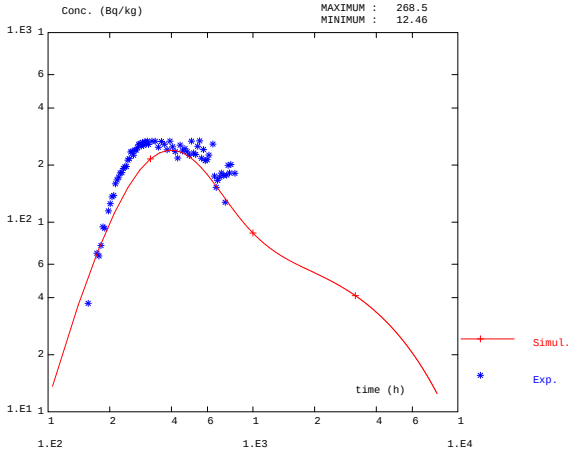

(b) Calcium

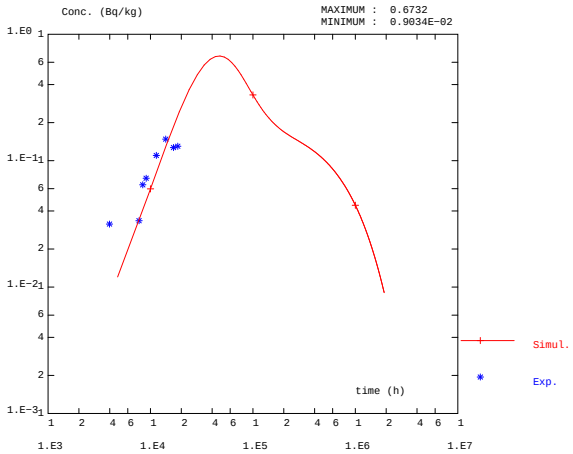

(c) Cesium

Figure 4.7: Fitted breakthrough curves for different tracers

4.3.1 Flow

Description of the flow paths

One may refer to figure 4.6. The length of the advection path is 77.65 m along features 23, 22, 20 and 21.

Drawdown in injection and pumping boreholes

Drawdown at pumping borehole is -243 m, at injection borehole -151 m.

4.3.2 Transport

F-factor: ratio flow wetted surface to water flow

The whole of the fracture is filled up with water in motion. The fracture apertures are summed up on table 4.6.

Structure Name	Aperture (m)
20	$1.740\ 10^{-4}$
21	$1.129\ 10^{-4}$
22	$1.702\ 10^{-4}$
23	$4.685\ 10^{-4}$

Table 4.6: Fracture apertures associated with the 4 deterministic features modeled (as calibrated)

Breakthrough time history for the tracers

The breakthrough time history for the six tracers considered are provided on figure 4.8. The order of arrival is related with the sorbing properties of each tracer : first Rhenium, then Calcium, Cesium, Radium, Technetium, Americium. The same breakthrough curves are provided on figures 4.9 and 4.10 in another format.

4.3.3 Maximum release rates

Maximum release rates as well as the time associated with the peak are provided on Table 4.8. The order of arrival follows the importance of the sorption phenomenon of the tracer considered.

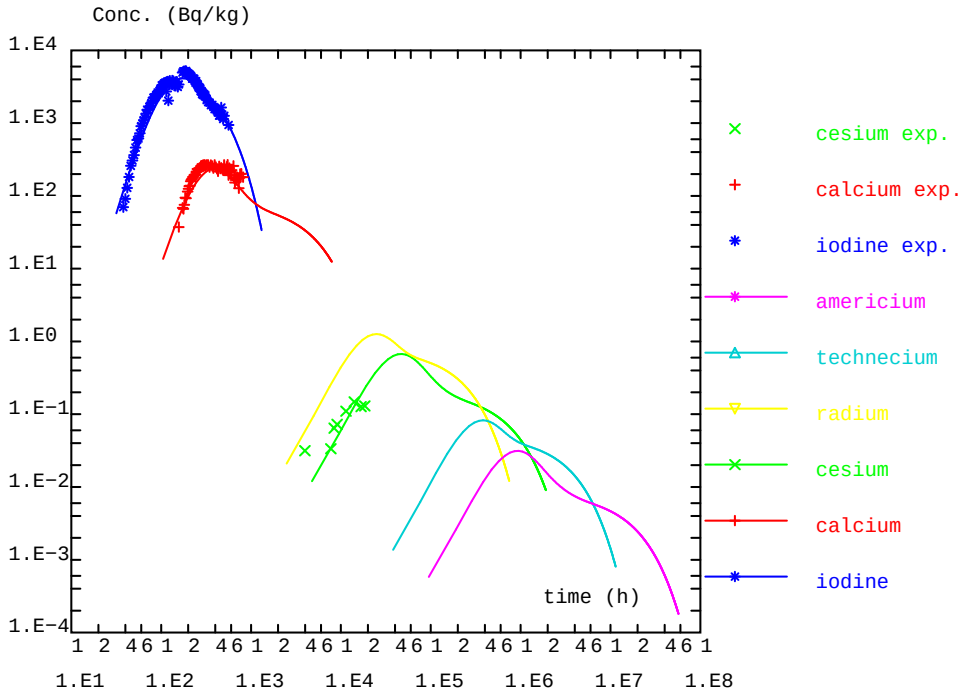

(a) BTC for injected signal

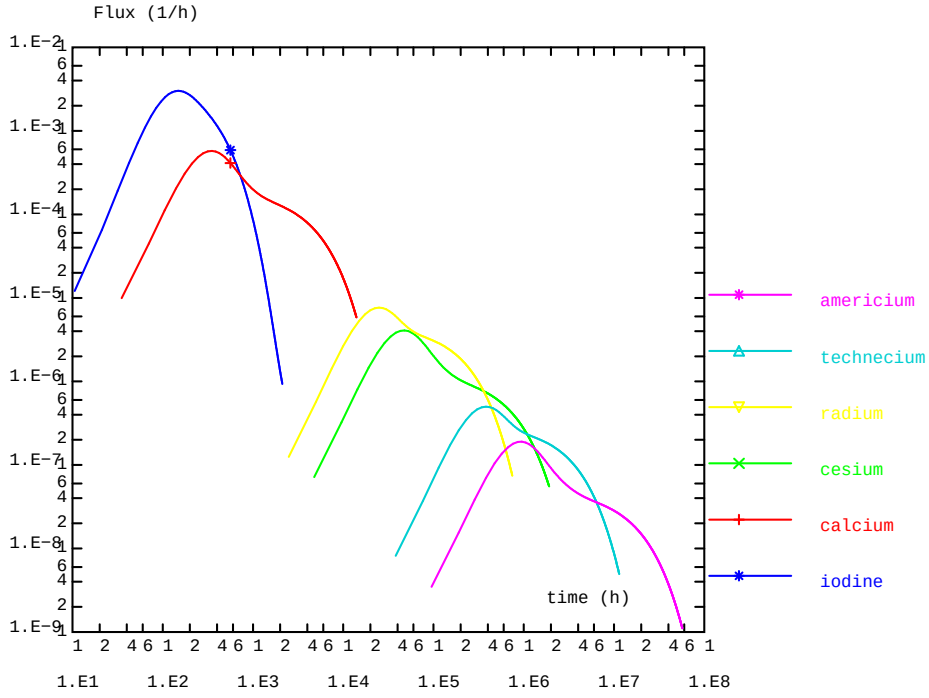

(b) BTC for Dirac input

Figure 4.8: Breakthrough time histories for Real source and Dirac input

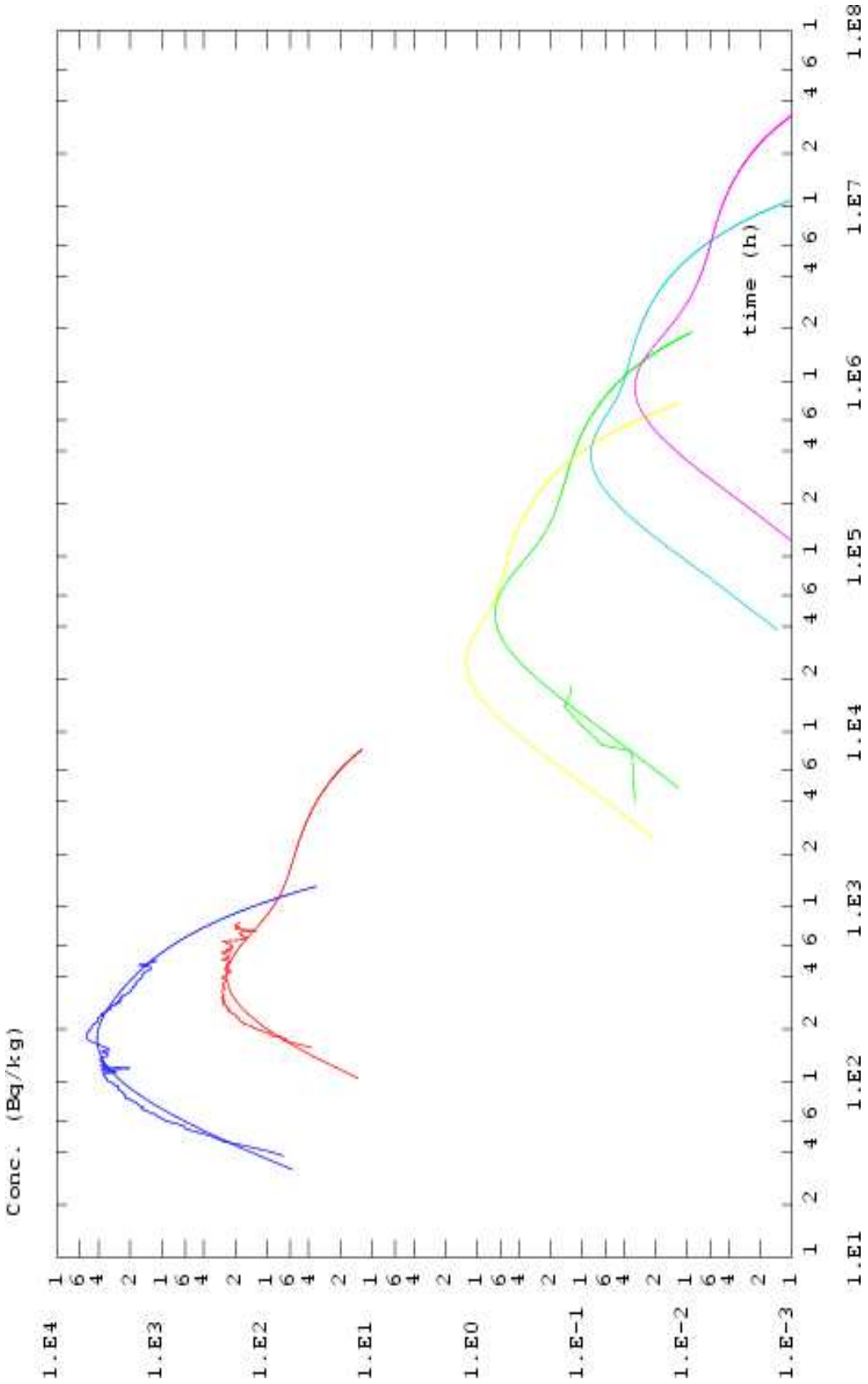

Figure 4.9: Breakthrough time histories for real source

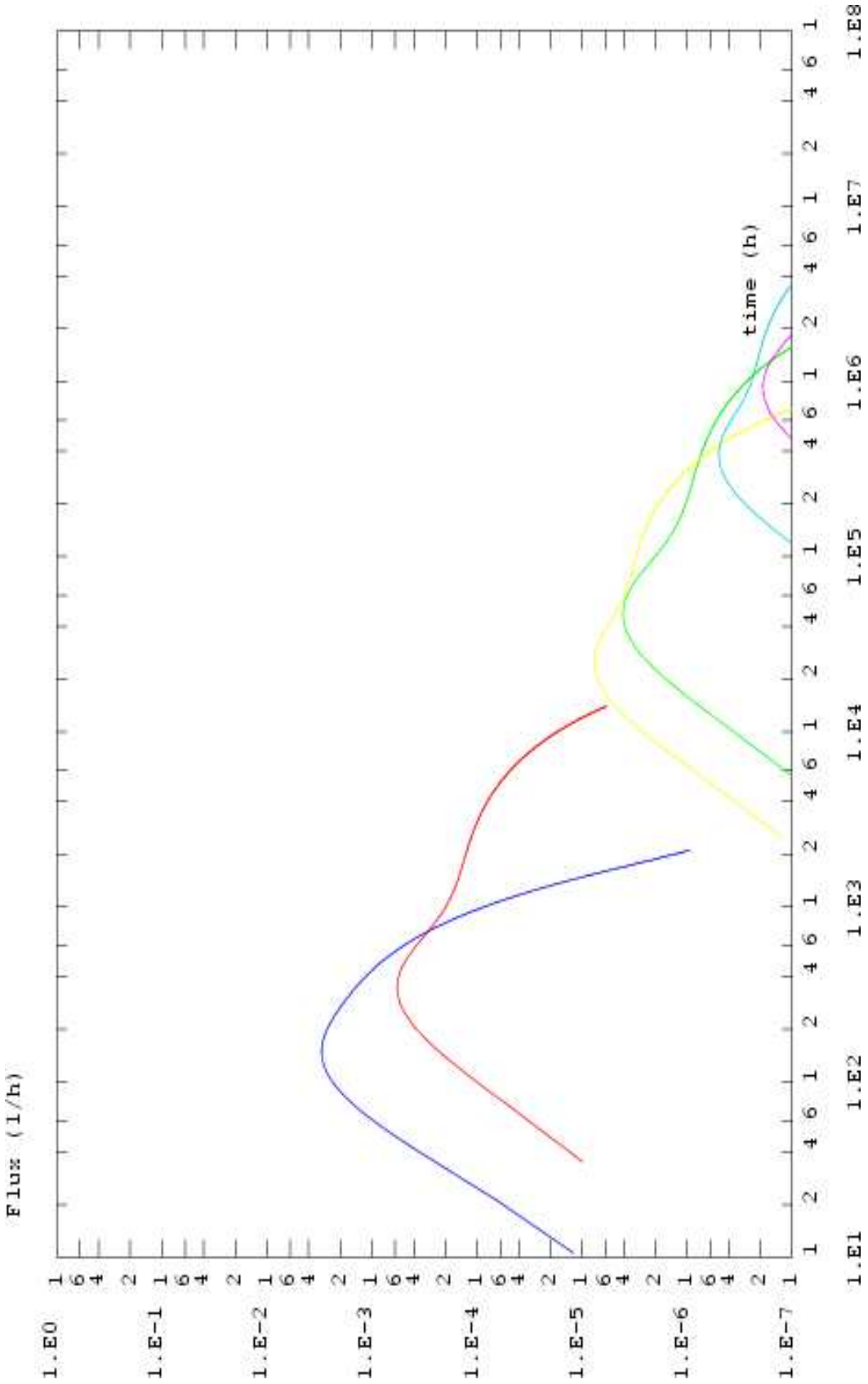

Figure 4.10: Breakthrough time histories for a mass Dirac input

Source	$T_{5\%}(h)$	$T_{50\%}(h)$	$T_{95\%}(h)$
Rhenium Dirac	79.362	248.67	788.33
Rhenium Real	100.53	290.99	1222.2
Calcium Dirac	227.89	2086.1	10956.
Calcium Real	298.01	1910.8	7836.0
Cesium Dirac	31043.	3.1210^5	1.6510^6
Cesium Real	35819.	3.2210^5	1.8710^6
Radium Dirac	16186.	1.2310^5	5.1710^5
Radium Real	18677.	1.3110^5	7.1610^5
Technetium Dirac	2.4810^5	1.8910^6	7.9410^6
Technetium Real	2.8610^5	2.0010^6	1.110^7
Americium Dirac	6.1910^5	7.5710^6	4.0910^7
Americium Real	7.1410^5	8.1410^6	5.5110^7

Table 4.7: Performance measures: breakthrough time history

Source	Maximal flux	Time (h)
Rhenium Dirac	$3.0110^{-3}(1/h)$	148.14
Rhenium Real	$5.8910^5(Bq/h)$	179.89
Calcium Dirac	$5.7510^{-4}(1/h)$	350.60
Calcium Real	$34090.(Bq/h)$	385.66
Cesium Dirac	$4.0810^{-6}(1/h)$	47758.
Cesium Real	$95.892(Bq/h)$	47758.
Radium Dirac	$7.6510^{-6}(1/h)$	24902.
Radium Real	$179.91(Bq/h)$	24902.
Technetium Dirac	$4.9910^{-7}(1/h)$	3.8110^5
Technetium Real	$11.737(Bq/h)$	3.8110^5
Americium Dirac	$1.8910^{-7}(1/h)$	9.5210^5
Americium Real	$4.4593(Bq/h)$	9.5210^5

Table 4.8: Performance measures: maximum fluxes for Dirac and real source for the different tracers considered

4.3.4 Sensitivity analysis

We study here the sensitivity of the system to its different units. We saw previously (Task6A and B) that matrix properties play a minor role (shape of the tail) whereas fracture transport apertures are responsible for changes in the peak level and arrival time that have larger consequences.

Studies conducted here show similarly that the most sensitive parameter is advective travel time. So two points could be considered to illustrate and quantify this effect:

1. Modify flow properties. This was not studied here since no calibration in terms of flow properties is considered. It is nevertheless potentially important and should

include as well the issue of back ground fracturing and the role played by minor faults as providing alternative travel paths.

2. Study the sensitivity of the system calibrated to fracture aperture.

The latter point is presented here.

We conduct here sensitivity study of the breakthrough curves to fracture apertures. In this we consider the calibrated data set and change iteratively the apertures corresponding to features 20 to 23. The change is plus or minus 50% of the fracture aperture. Results are provided on figure 4.11 for a Dirac input. The advection path is from the injection well along features 23, 22, 20 and finally 21. The impact in aperture change is larger for feature 23 and 22, weak for feature 20, negligible for feature 21. This is due to the advective travel time in each unit. It is lower for features close to the pumping well due to the structure of the velocity field in radial flow conditions. As a consequence a modification of the transport aperture related with a feature providing a large travel time (e.g. feature 23) has a major impact on the shape of the breakthrough curve.

The point illustrated here is developed below in terms of identification of the apertures associated with the different features. The conclusions are that fracture transport apertures can be acceptably constrained for features 23 and 22 but not for features 20 and 21.

The same exercise was conducted for sorbing tracers and lead to similar results.

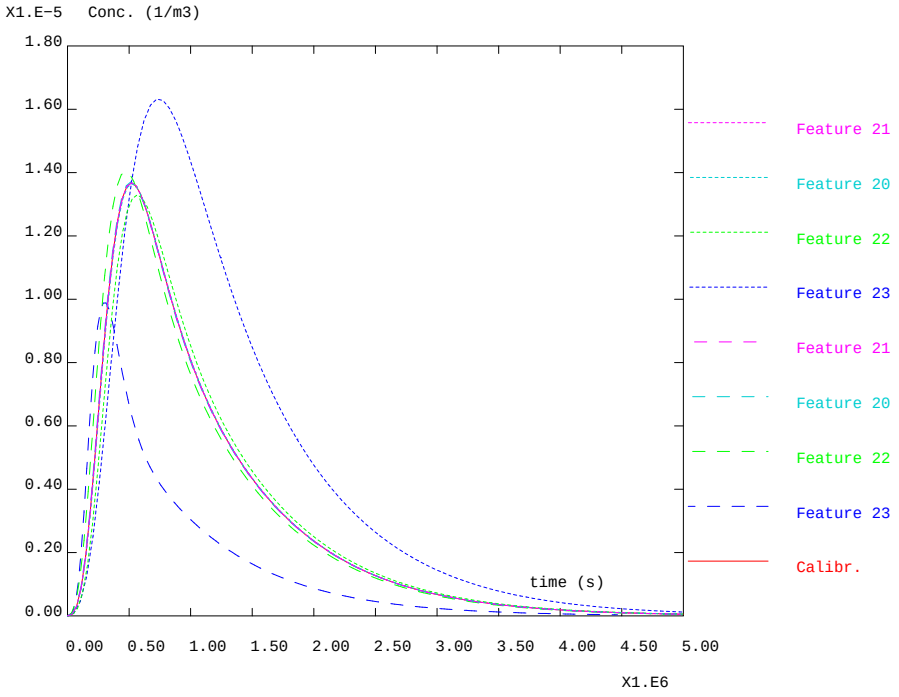

Figure 4.11: Sensitivity to fracture transport apertures for a Dirac input

4.4 Discussion and conclusions

4.4.1 Discussion of results

We comment here more in details about the calibration procedure and more precisely what information is contained in the tracer test breakthrough curves. One may refer to section 4.2.5 and figure 4.8.

- Little information is contained in the Cesium breakthrough curve due to the scarcity of the time series.
- The following points are of importance to extract the information contained in the breakthrough curves:
  - The *peak arrival time* is strongly related with the advective travel path depending on boundary conditions as well as fracture apertures. As developed below, due to the radial structure of the flow, the fracture far from the pumping well along the advective path have the larger impact on the arrival time. The travel time in such units is much larger so that a change in the former strongly affects the arrival time. In conclusion, the time associated with the peak of the breakthrough curve allows for identification of an averaged transport aperture along the advective travel path. This average most strongly depends on fracture properties far from the pumping well (features 23 and 22).
  - The calibrated data set is not unique due to another important point. Indeed the *spread of the breakthrough curve* is largely connected with dispersion in the fracture planes as well as matrix diffusion. The information contained here in the tail of the measured curves does not allow for strict discrimination between these two mechanisms. This was mentioned previously (see [*Grenier 03*]). It is confirmed here although due to constraints in the discretization of the planes as well as numerical stability, this could not be largely tested.
  - Moreover, similar considerations as the previous ones can be conducted in relation with matrix diffusion properties. As stated previously (see [*Grenier 03*]), the average matrix property calibrated is more representative of matrix properties in zones where flow is slow so that contact time with the matrix is large. So tracer tests allow for identification of matrix properties more closely related with feature 23 and 22 matrix properties.
- Although most conclusions drawn here are in line with former results obtained on the single fracture case ([*Grenier 03*]), it should be stressed that matrix diffusion has in the present case a larger impact (not illustrated here) on the breakthrough curves. This is due among others to the larger transport path allowing for slower velocities at the injection end and larger contact times of the plume with the matrix zones. As a consequence matrix diffusion can be better identified due to larger sensitivity of the breakthrough curves to it.

- The calibrated data set is globally coherent with the data provided in the deliveries:
  - Matrix property calibrated provides an averaged view of the most diffusive and porous matrix zones close to the fracture advection path. The calibrated values show lower and close to gouge properties, the most diffusive and porous unit.
  - Fracture apertures are in the same order of magnitude as for the provided dataset. We nevertheless had to multiply the aperture associated with the two major units by a factor 2.5.

The quality of the calibration can be drawn along the following points:

- We provide here results showing that for the provided coherent dataset and a simple geometrical model, fair calibration can be achieved. This optimal solution is nevertheless not unique.
- Sensitivity analysis to the flow properties were conducted superimposing fluctuations on the fluxes imposed as boundary conditions. These are obtained from the larger 200 m model. The advective travel path proved rather sensitive to the input fluxes (though constrained (by construction) to remain in the 4 modeled fractures). No systematic sensitivity analysis has been conducted for Dirac or injected input signal.
- As mentioned before and in [*Grenier 03*], it is hard to distinguish between dispersion and matrix diffusion.

4.4.2 Main conclusions

We conclude here in the line previously drawn in [*Grenier 03*] mentioning that little information is obtained from the tracer tests provided. A calibration could be provided here based on a rather simple geometrical model. The calibrated dataset is nevertheless non unique as shown by sensitivity analysis to elements of the parameter set as well as boundary conditions. So we consider the present study more assesses the global coherence of the geometrical features as well as parameter sets rather than represents an actual calibration exercise in the sense of a clear identification of system properties. The parameters calibrated here appear realistic.

4.4.3 Lessons learned and implications for Task6 objectives

As a conclusion, tracer tests provide a limited amount of information. They provide an average view of the properties of matrix zones close to the flow path and providing larger diffusion coefficients as well as porosities. This identification is nevertheless non unique.

The determination of the advective travel path is a prerequisite. It is done considering the peak arrival time and constraints the average fracture aperture. Discrimination between dispersion and matrix diffusion effects both leading to a spread in the breakthrough curves is difficult. This is due to the low precision in the breakthrough curves for large times.

As a consequence, including the information contained in the Test C2 tracer test in the coming Task 6E should prove of secondary importance. This is due to the limited constraining power of the test as well as the reduced spatial scale of the zone studied by the test as compared with the size of the block considered for predictions.

Nevertheless, the dataset available considered in the present study showed coherent. So, we will make use of the information resulting from Task 6C in the future including fracture geometries, transmissivities and apertures as well as properties associated with matrix zones.

For the future steps of the task, the whole complexity of the system should be included, involving back ground fracturing as well as fracture complexity. This was not considered here in the framework of inverse problem since tracer test was expected to be not enough constraining to identify such details of the system.

Chapter 5

Task 6E

5.1 Modeling strategy

Modeling strategy is presented in former section 3. Nevertheless sensitivity to the amount of fractures included in the model is conducted with the idea that all 5600 fracture should not necessarily be included into the model. We order the fracture by decreasing size, retaining in addition features situated in the vicinity of the initial pulse regardless of their size. A large portion of the initial 5600 fractures are nevertheless not connected so that they can be sorted out directly (we conduct here a discrete fracture approach).

Sensitivity of the transport simulations to various characteristics of the model (mesh size or minimal number of meshes discretizing the fracture planes, dispersion coefficient ...) as well as the amount of fracture included is presented in the following section.

No calibration was conducted for the model based on any tracer test due to the limited amount of information inferable from them for PA time scale applications. Refer to chapter 4.

5.1.1 Convergence tests

We conduct here convergence studies. The quality of the numerical simulations has to be tested by varying the values associated with spatial and temporal discretizations. We work here on the 150 fracture system. The same results hold for the final 1200 fracture predictive simulations.

Globally, care was put into the following items:

- All fractures should be sufficiently discretized to enable reproduction of the complex flow and transport features existing in such a highly heterogeneous medium. Low discretization excessively simplifies transfers between units. The effect of this

simplification is hard to assess. As a consequence we put efforts in sufficiently meshing the system and assess the quality of the flow field and transport features within the modeled conductors. A visualization of the complexity of the flow field within one fracture plane is provided on figure 5.1. The associated transport features are as well highly variable along quicker and slower flow lines with complicated transport paths.

- All 5600 fractures can't be included into the model with sufficient numerical precision. Indeed including small fractures requires spatial discretization sufficiently small compared with the smallest feature considered. This results into very large computer costs. In addition care should be taken into proper treatment of complex intersections resulting in meshing difficulties. We decided excluding smaller fractures from the model rather than decreasing simulation quality. This was nevertheless possible because of the results of connectivity studies as well as sensitivity analysis of block properties to the amount of fractures included. It is in close connection with the properties of the block: geometrical structure as well as the associated parameters. For instance a fracture block close to percolation conditions can not be treated without including smaller units. We conduct here sensitivity analysis to the amount of fractures included in the model. These are ordered by decreasing size. Care is provided to smaller fractures in the vicinity of the injection location.

These issues are discussed in more details in the following sections.

Flow

Spatial discretization

We test the variation of the hydraulic flux versus the cell size. As we can see, Tab. 5.1, the flow calculation is already converged for 5 meter cells.

As shown on figure 5.1, the flow patterns are complex with our approach providing a large distribution of transport paths.

Cell Size	5 m	4 m	3 m	2.5 m
out flux	5.74	5.77	5.80	5.77

Table 5.1: Spatial convergence: flow out-fluxes for the different cell sizes considered.

The order 2 Hybrid Mixed Finite Element method guarantees an error reduction proportional to the square of the cell diameter. Hence the error is reduced by a factor 4 when we vary the cell size from 5 down to 2.5 meters. The observed difference between the out fluxes on these two meshes (less than 1 %) indicates a very low error, even for the coarsest mesh.

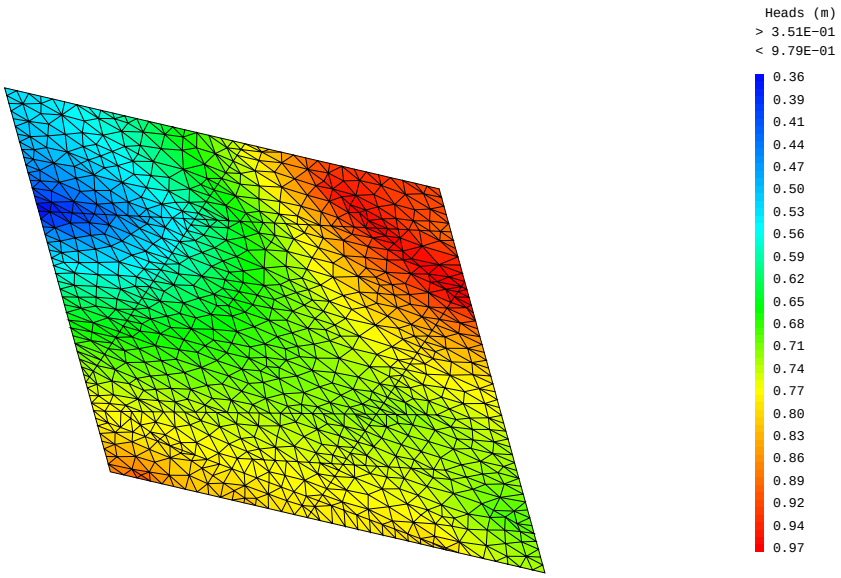

(a) Head fi eld

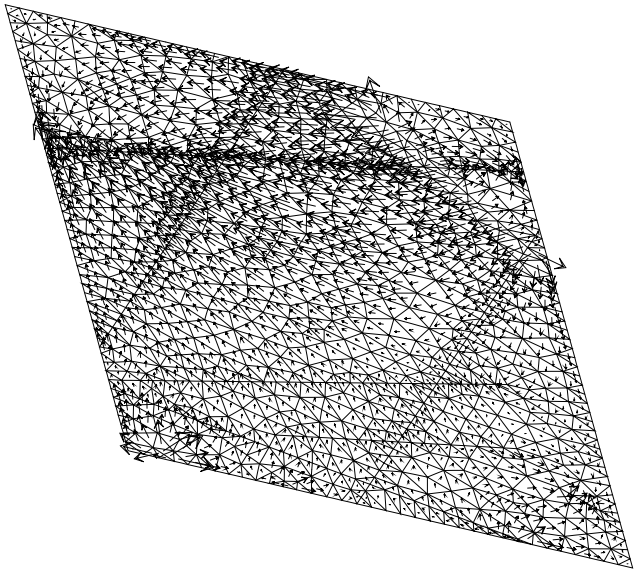

(b) Flow fi eld, Darcy velocities

Figure 5.1: Variability of the head and flow field within one fracture plane.

Geometrical convergence

Now that we are sure that our discretization of Darcy's law is accurate enough, we have to ensure that the considered geometry represents correctly the flow in the 200 meter block.

We therefore test the hydraulic flux at the exit ($x = 1800m$) versus the amount of fractures represented. We classify the fracture by decreasing size order. We then mesh the n first fractures, n being varied from 50 up to 1200. We plot the evolution of the flux versus n, see Fig. 5.2.

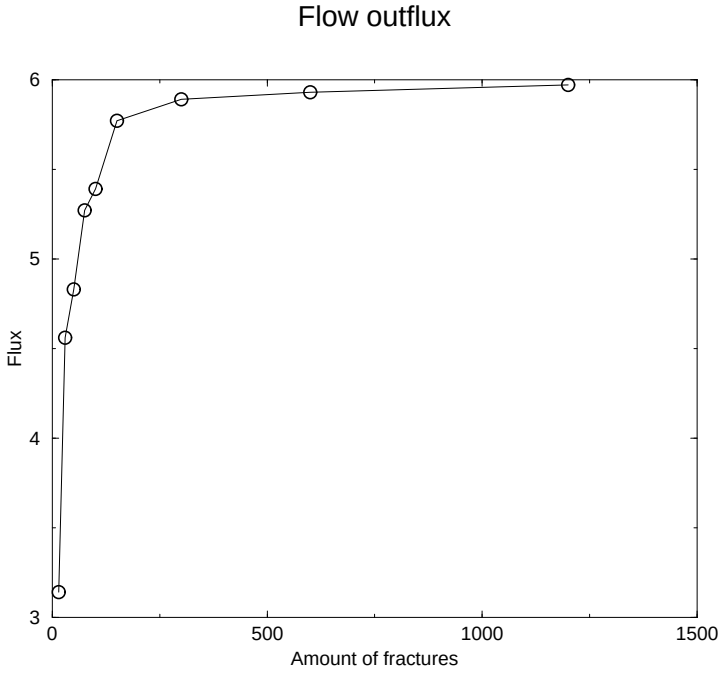

Figure 5.2: Evolution of the hydraulic flux versus the amount of fractures

We notice that the 150 largest fractures contributes to 95 % of the flow flux. Therefore, we will limit ourselves to these 150 largest fracture for our sensitivity studies. The reference model contains 1200 features.

Transport

Spatial discretization

A similar spatial convergence test has been carried out for the transport with similar result. We conclude that cells of diameter below 3 meters allow good accuracy for the discretization. We will therefore use 2.5 meters cells (maximum size) in our simulations.

Time discretization

The transport problem being non stationary, we have to check the impact of time discretization. We varied the time steps by a factor 10 until the influence on the concentration fluxes are below 5 %. This resulted in simulations conducted with series of times steps varying from small times steps to begin to larger time steps for the large times. Indeed, concentration strongly varies at the beginning whereas fronts are weaker for the end of the tails of breakthrough curves. The time increments considered for the different RNs are summed up in Tab. 5.2. The presented discretizations are only valid for the full final system presented below as reference case (matrix diffusion and a retardation coefficient based on the dominating fracture type). These time steps have been reevaluated in every different physical situations.

RN	step (y)	step (y)	step (y)	step (y)	step (y)	step (y)	step (y)	step (y)
I129	2.4	12	80	400	$2\ 10^3$			
until	$\rightarrow 240$	$\rightarrow 480$	$\rightarrow 2400$	$\rightarrow 24\ 10^3$	$\rightarrow 8\ 10^4$			
Ca	8	24	48	96	240	1600	$8\ 10^3$	$4\ 10^4$
until	$\rightarrow 120$	$\rightarrow 1200$	$\rightarrow 2400$	$\rightarrow 4800$	$\rightarrow 19200$	$\rightarrow 48\ 10^3$	$\rightarrow 48\ 10^4$	$\rightarrow 16\ 10^4$
Cs	1600	$4\ 10^3$	9600	$24\ 10^3$	$16\ 10^4$	$8\ 10^5$	$4\ 10^6$	
until	$\rightarrow 24\ 10^3$	$\rightarrow 96\ 10^3$	$\rightarrow 48\ 10^4$	$\rightarrow 192\ 10^4$	$\rightarrow 48\ 10^5$	$\rightarrow 48\ 10^6$	$\rightarrow 16\ 10^7$	
Ra	1600	$4\ 10^3$	9600	$24\ 10^3$	$16\ 10^4$	$8\ 10^5$	$4\ 10^6$	
until	$\rightarrow 24\ 10^3$	$\rightarrow 96\ 10^3$	$\rightarrow 48\ 10^4$	$\rightarrow 192\ 10^4$	$\rightarrow 48\ 10^5$	$\rightarrow 48\ 10^6$	$\rightarrow 16\ 10^7$	
Tc	4800	$12\ 10^3$	28800	$72\ 10^3$	$48\ 10^4$	$24\ 10^5$	$12\ 10^6$	
until	$\rightarrow 72\ 10^3$	$\rightarrow 288\ 10^3$	$\rightarrow 144\ 10^4$	$\rightarrow 576\ 10^4$	$\rightarrow 144\ 10^5$	$\rightarrow 144\ 10^6$	$\rightarrow 48\ 10^7$	
Am	4800	$12\ 10^3$	28800	$72\ 10^3$	$48\ 10^4$	$24\ 10^5$	$12\ 10^6$	
until	$\rightarrow 72\ 10^3$	$\rightarrow 288\ 10^3$	$\rightarrow 144\ 10^4$	$\rightarrow 576\ 10^4$	$\rightarrow 144\ 10^5$	$\rightarrow 144\ 10^6$	$\rightarrow 48\ 10^7$	

Table 5.2: Time discretization, transport with matrix diffusion

Geometrical convergence

General remarks

We studied the influence of the amount of fracture included to the flow and transport properties of the block. Results show mainly that the larger fractures have to be included into the system. Smaller fractures mainly lead to second order effects in terms of flow and transport properties. Nevertheless small fractures in the vicinity of the initial source term are very important to account for. We noticed in particular that a fracture (numbered 2101C) has a major role in the transport. This fracture connects the 23D unit (hosting source term) to the rest of the flowing network. Without it there is limited flow in 23D unit and mass exits mainly by diffusion. Including 2101C allows a new flow path across 23D. These units are represented on Fig 5.3.

We had to consider as well all the fractures (among the 5600) intersecting the 23D. Nine fractures were found : the 22D, 1925B, 2101C, 176C, 2984B, 483C, 1198C, 1386B and 748B, see Fig. 5.4.

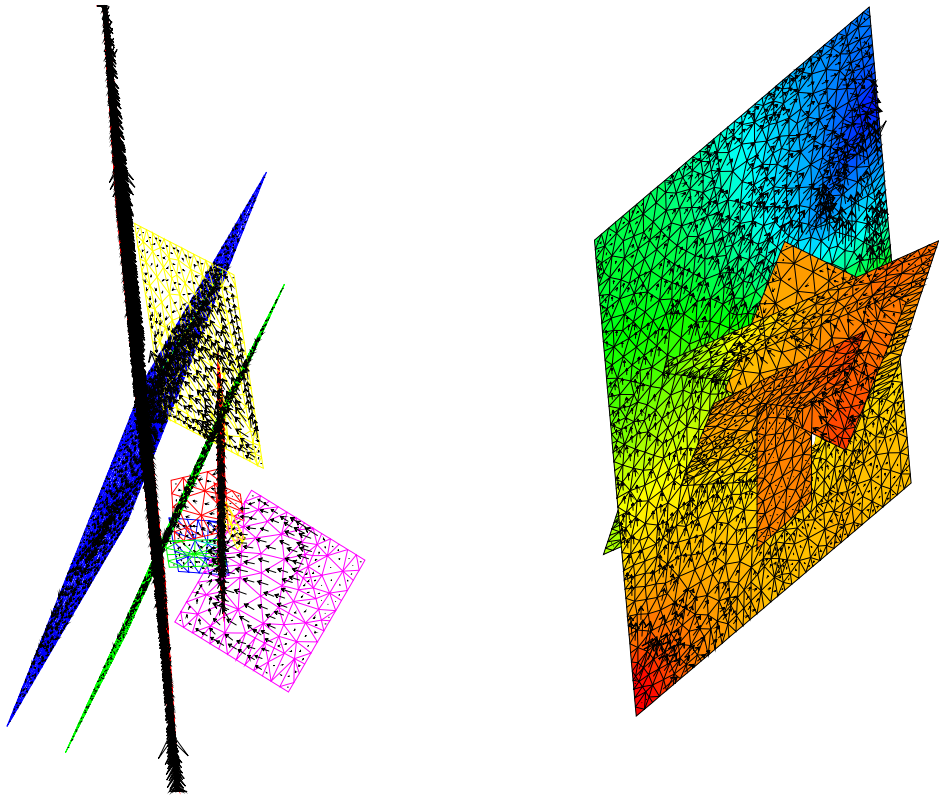

(a) Flow in 23D with connecting 2101C fracture

(b) Flow in 23D without 2101C fracture

Figure 5.3: Influence of fracture 2101C.

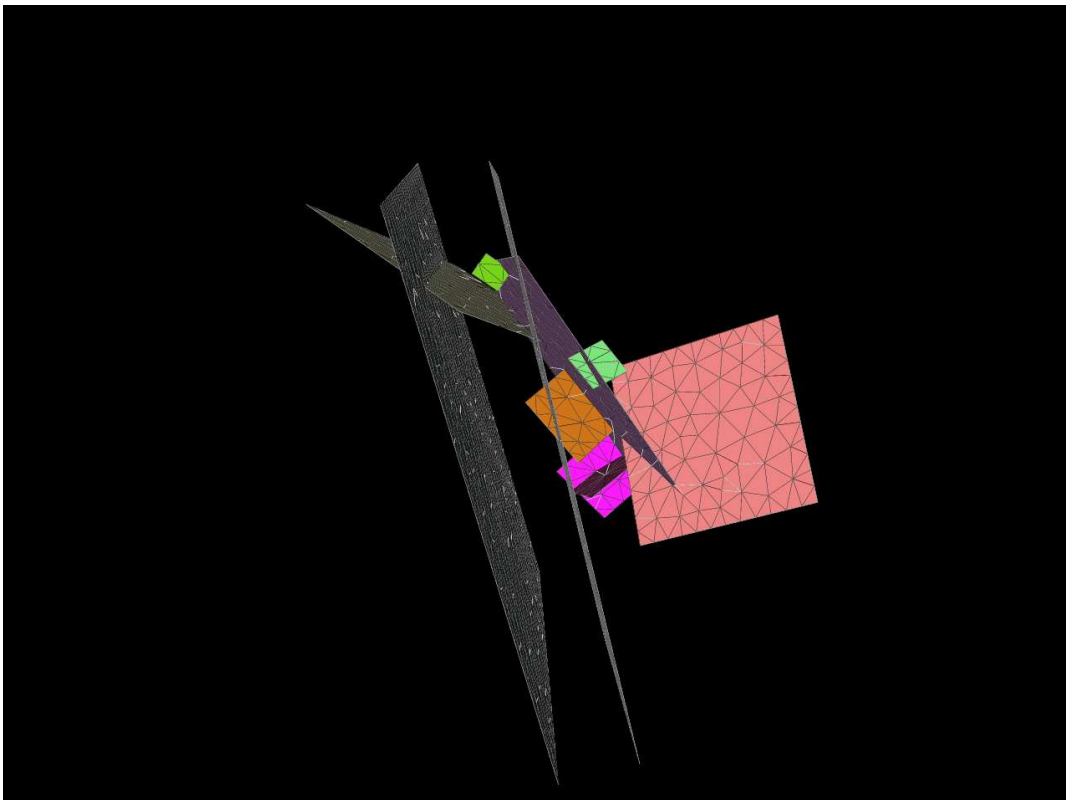

Figure 5.4: Fractures intersecting 23D.

Similarly to the flow calculations, we studied the sensitivity of the concentration flux to the amount of fractures considered for the numerical simulations. We search here for a good reference case knowing that all units can't be included in the model because of meshing constraints. A similar study of sensitivity to the amount of fractures with the idea of simplifying the system to minimal features in the chapter 5.2.

Comparisons

We compare 4 different situations for Dirac pulse injection as source term:

- A geometry made of the 50 largest fractures (including 23D but not the smaller features).
- The previous geometry plus the nine smaller fractures intersecting fracture 23D.
- The 150 largest fractures plus the nine fractures intersecting fracture 23D.
- The 1200 largest fractures (containing these nine units).

We point out that only the 2101C fracture is of importance among the nine intersecting fractures. This fracture being in the 100 largest fractures, all simulations involving more than a hundred of fractures could be done without adding the eight other fractures intersecting 23D, with no real effect on the results.

We sum up in Tab. 5.3 the differences between time recoveries for these simulations. The physical model retained for these simulation involves the final reference conditions except for the amount of fractures (1200):

- matrix diffusion with two layers ;
- retardation coefficient based on fracture dominating type ;
- longitudinal dispersivity of 3 meters.

We notice that the 50 plus 9 fractures and the 150 plus 9 fractures simulations give almost the same results. On the other hand, the 50 fractures simulation gives longer recovery times : nearly twice longer for 5 % recovery, 5 times longer for 50 % recovery, and not evaluated for 95 % recovery due to very long recovery times. This shows the very strong influence of the local flow properties in the vicinity of the 23D source fracture, although the global flow out flux is not strongly affected (20 % lower for the 50 fractures compared to the 50 plus 9 intersecting fractures).

The 1200 fractures simulation gives slightly longer time recoveries than with 150 fractures (less than 10 %). It indicates that background fractures do have a small retardation effect by providing increased volume of slower transfer properties.

Source	$T_{5\%}(h)$	$T_{50\%}(h)$	$T_{95\%}(h)$
Iodine 50	48	1000	> 80000
Iodine 50P9	26	260	44000
Iodine 150P9	26	260	42000
Iodine 1200	29	300	48000
Calcium 50	624	15000	$> 1.6\ 10^6$
Calcium 50P9	312	3840	$6.4\ 10^5$
Calcium 150P9	310	3840	$6.4\ 10^5$
Calcium 1200	336	4400	$7.2\ 10^5$
Cesium 50	$3\ 10^5$	$8.8\ 10^6$	$> 1.6\ 10^8$
Cesium 50P9	$1.4\ 10^5$	$2.1\ 10^6$	$> 1.6\ 10^8$
Cesium 150P9	$1.4\ 10^5$	$2.1\ 10^6$	$> 1.6\ 10^8$
Cesium 1200	$1.53\ 10^5$	$2.4\ 10^6$	$> 1.6\ 10^8$
Radium 50	$1.2\ 10^5$.	$3.4\ 10^6$	$> 1.6\ 10^8$
Radium 50P9	64000.	$8.4\ 10^5$	$1.5\ 10^8$
Radium 150P9	64000.	$8.6\ 10^5$	$1.4\ 10^8$
Radium 1200	68000.	$9.6\ 10^5$	$1.6\ 10^8$
Technetium 50	$8.0\ 10^5$	$2.1\ 10^7$	$> 4.8\ 10^8$
Technetium 50P9	$4.0\ 10^5$	$5.4\ 10^6$	$> 4.8\ 10^8$
Technetium 150P9	$4.0\ 10^5$	$5.5\ 10^6$	$> 4.8\ 10^8$
Technetium 1200	$4.3\ 10^5$	$6.2\ 10^6$	$> 4.8\ 10^8$
Americium 50	$3.1\ 10^6$	$6.5\ 10^7$	$> 4.8\ 10^6$
Americium 50P9	$1.1\ 10^6$	$1.4\ 10^7$	$> 4.8\ 10^8$
Americium 150P9	$1.1\ 10^6$	$1.4\ 10^7$	$> 4.8\ 10^8$
Americium 1200	$1.2\ 10^6$	$1.7\ 10^7$	$> 4.8\ 10^8$

Table 5.3: Sensitivity to the amount of fractures : breakthrough time recoveries

5.1.2 Sensitivity studies

In this chapter we address modeling issues by means of sensitivity studies:

- Section 5.1.2: sensitivity study to dispersion coefficient allows us to raise the question of the importance of dispersivity associated with single conductors against dispersion effects resulting from numerous transport paths. This sensitivity analysis helps as well in choosing the most adequate value (classically chosen as mesh size in lack of further information).

- Section 5.1.2: sensitivity of breakthrough curves to matrix zones located in the close vicinity of fracture planes. We consider the different configurations associated with the complexity of the conductors: calcite for Type 2 and gouge, cataclasite, calcite for Type 1. We consider successively fractures associated with pure Type 1, pure Type 2 and finally the dominant type associated with each feature as from deliveries. The additional impact of altered and non altered rock actually belonging

to the fractured zones but requiring further complexity of the model is conducted in the following section.

- Section 5.1.2: sensitivity to matrix diffusion involving additionally deeper matrix zones (corresponding to altered and non altered rock). We add more in depth zones to the model, these zones are not equivalent to retardation coefficient but act as transitory storage zones. We consider here 3 different options to study their impact: unlimited diffusion into a homogeneous zone, unlimited diffusion, diffusion into a semi infinite composite medium. The latter configuration corresponds to the actual complexity required since altered rim (20 cm) as well as non altered rock with very large depth are represented.
- Section 5.1.2: analysis of the impact of various matrix zones is conducted and analytical expressions for retardation in peak arrival times are proposed based on single fracture cases.
- Based on former studies the actual model for reference calculations is selected in 5.1.2.
- Section 5.1.2: sensitivity to the amount of modeled fractures is carried out here aiming at a final simplest system possible providing breakthrough curves similar to reference calculations with limited reduced precision. We end up with a system of 12 fractures called simplified PA model. This simplified model provides breakthrough curves differing maximally from reference case by 20%. The way breakthrough curves are degraded is studied providing insights into the influence of back ground fracturing.

Dispersivity

We study the sensitivity of the model to the dispersivity value. We choose dispersivity with tensorial structure, longitudinal and transverse components in the local velocity spatial reference. Two values of the dispersivities are studied:

- α_L = 30 m and α_T = 3 m.
- α_L = 3 m and α_T = 0.3 m.

In order to maximize the effect of the considered dispersivity variation (which occurs only in the fracture and not in the no flow matrix), we are not taking into account the matrix diffusion in the sensitivity test.

We can't consider lower values because numerical diffusion induces a dispersivity of approximately the size of a cell (approximately 2-3 meters in our case).

Larger values are also not to be considered. Indeed, the dispersivity coefficient is connected to the size of the heterogeneity it models. 50 meters is in any case a higher limit since only few fractures have larger extensions.

Comparisons of breakthrough curves

We represent, Fig 5.5, the breakthrough curves for the two studied cases. The graphs are provided as required in the specifications : in log-log scale in a frame 20cm * 12cm.

For each tracer, we associate a color as follows:

- Red for Rhenium/Iodine
- Blue for Calcium
- Green for Cesium
- Yellow for Radium
- Cyan for Technetium
- Magenta for Americium

We notice that the curves are comparable in both cases, with a slightly more pronounced spreading of the flux in the stronger dispersivity case (as expected). As a consequence, overall spreading mostly results from the multiplicity of travel path velocities rather than choice for dispersivity values. The actual choice of dispersivity for the final reference calculation only corresponds to second order effects.

Comparisons of maximum release rates

The maximum peak values for the flux are summed up in Tab. 5.4. The maximal flux for $\alpha_L = 30$m is reduced less than 15 % below the values obtained with the limited dispersivity case.

Source	Maximal flux	Time (y)
Iode Dirac - 3m	$2.110^{-2}(1/y)$	20
Iode Dirac - 30m	$1.810^{-2}(1/y)$	22
Calcium Dirac - 3m	$3.310^{-3}(1/y)$	135
Calcium Dirac - 30m	$3.210^{-3}(1/y)$	165
Cesium Dirac - 3m	$1.810^{-5}(1/y)$	26000
Cesium Dirac - 30m	$1.810^{-5}(1/y)$	30000
Radium Dirac - 3m	$2.010^{-5}(1/y)$	22000
Radium Dirac - 30m	$2.010^{-5}(1/y)$	22000
Technetium Dirac - 3m	$3.510^{-6}(1/y)$	1.310^5
Technetium Dirac - 30m	$3.610^{-6}(1/y)$	1.510^5
Americium Dirac - 3m	$1.410^{-6}(1/y)$	3.310^5
Americium Dirac - 30m	$1.410^{-6}(1/y)$	3.810^5

Table 5.4: Performance measures: maximum fluxes for Dirac for the different tracers considered and two different dispersivities (3m and 30m).

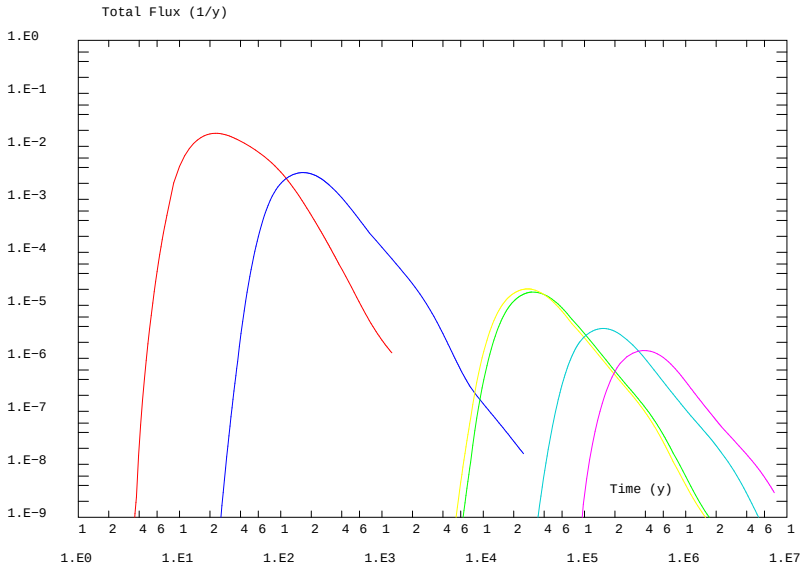

(a) Breakthrough curves for a 3 meters longitudinal dispersivity coeffi - cient

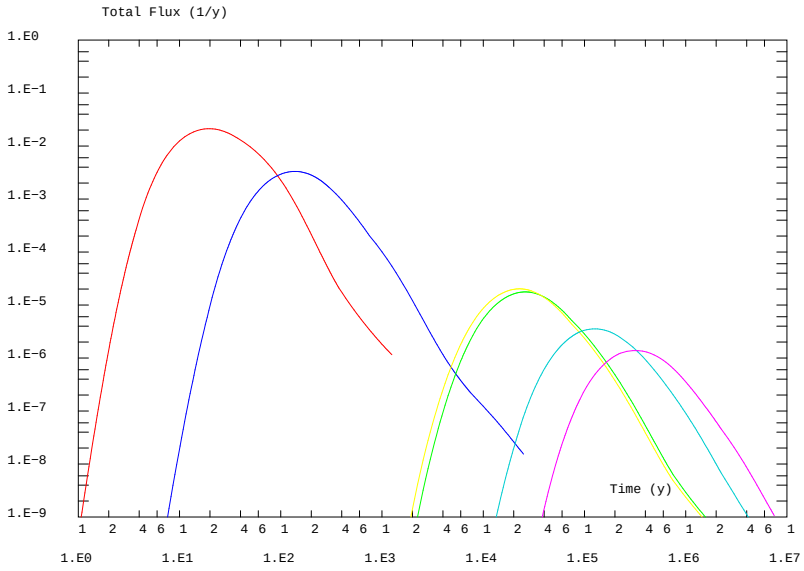

(b) Breakthrough curves for a 30 meters longitudinal dispersivity coef- fi cient

Figure 5.5: Influence of dispersivity.

Comparisons of tracer time recoveries

The 5, 50 and 95 % time recoveries for the flux are summed up in Tab. 5.5.

Source	$T_{5\%}(y)$	$T_{50\%}(y)$	$T_{95\%}(y)$
Iode Dirac - 3m	11	34	130
Iode Dirac - 30m	14	44	180
Calcium Dirac - 3m	75	230	900
Calcium Dirac - 30m	100	260	1300
Cesium Dirac - 3m	14000	43000	1.810^5
Cesium Dirac - 30m	19000	47000	2.510^5
Radium Dirac - 3m	13000.	3.510^4	1.510^5
Radium Dirac - 30m	16000.	4.010^4	2.110^5
Technetium Dirac - 3m	7.010^4	2.110^5	9.010^5
Technetium Dirac - 30m	9.010^4	2.210^5	1.210^6
Americium Dirac - 3m	1.710^5	5.310^5	2.210^6
Americium Dirac - 30m	2.210^5	5.610^5	$> 3.010^6$

Table 5.5: Dispersivity $\alpha_L =$ 3m and 30m : breakthrough time history

We notice an influence of about 25 % on the time recoveries. It appears that the dispersivity, at least in the considered variation range, has no major influence on the tracer migration. Dispersivity models macro dispersion in the fractures as related with non explicitly modeled fracture heterogeneities. No indication is provided in the deliveries. We choose the lowest possible value: a numerical dispersivity of 3 meters (the size of the largest cell). More precisely, dispersivity corresponding to the size of each cell is considered so that minimal dispersivity is applied (equals numerical dispersion). This is achieved as provided below.

The convective term, in the transport equation, is discretized with a stream upwind discretization. This ensures the monotonicity of the discretized convection operator, which in practice implies that there won't be any negative value of the concentration. This stream upwind discretization induces a "numerical" diffusion $|U|L$, where L is the size of the cell and $|U|$ the norm of the Darcy velocity. This diffusion is set to 0 whenever its value is higher than the physical diffusion-dispersion. Which exactly means that the local Peclet number on each cell is lower than 1.

We can observe that this "numerical" diffusion is numerically **consistent**. It means that is tends to zero when the size of the cell tends to 0, which is obvious because this numerical diffusion scales with L. It can also be interpreted as a dispersivity, with a longitudinal coefficient $\alpha_L = L$ and a transverse coefficient $\alpha_T = 0$. Hence, it is not possible to reduce the actual longitudinal dispersivity below the size of the cell.

Complexity factor

We study here the sensitivity of the system to matrix zones in the vicinity of the fractures. These are for Type 1 fracture coating, cataclasite, gouge and for Type 2, fracture coating. For the flow velocities considered as well as for the actual fracture properties, these units have in common that they behave as simple buffers for transit in the fractures. They can be represented by an equivalent retardation coefficient. More details are provided in chapter 3. Different configurations are studied to assess the uncertainty in properties associated with the complexity of the fracture zones. More in depth matrix units like altered and non altered units are not included here but will be included later providing a direct measurement of their own impact on performance measurements.

Equivalent retardation coefficient

We sum up the different parameters involved in the complexity factors models, Tab. 5.1.2. We calculate the retardation coefficient the following way (refer to section 3):

$$R = 1 + \frac{1}{b} \sum_i \omega_i d_i R_i. \tag{5.1}$$

R_i is the retardation coefficient in the matrix zone i, d_i its thickness, ω_i its porosity and b the fracture aperture. This coefficient is to be calculated for each tracer (R_i depends on the tracer) and for each fracture (the aperture is changing).

The retardation coefficients R_i are obtained from the k_d :

$$R_i = k_{di} \rho_i (1 - \omega_i)/\omega_i, \tag{5.2}$$

where ρ_i is the density of the matrix zone, ω_i its porosity.

Models

Three different options are studied :

- We assign to each fracture its dominant type.
- We assign a pure type 1 to all fractures.
- We assign a pure type 2 to all fractures.

We don't handle different portions of different feature types within a fracture (no heterogeneity within a single conductor). Aiming to develop a simple PA model, such a stochastic approach is avoided since it would considerably slow down the calculations. Furthermore, at long time scales, choose the dominating type seems sensible.

The 2 other options are there to frame the field of possible situations as extreme sets.

For the type 1 fracture, the matrix diffusion zones considered are the gouge, the fracture coating and the cataclasite, in Eq. (5.2). For the type 2 fracture, only fracture coating is considered.

Task6E	Fracture	Fr. Coating	Gouge	Cataclasite	Altered Rock	Non Alt. R.
Extent	depends feature	$0.5mm$	$5mm$	$2cm$	$20cm$	$20cm$
Porosity	100 %	5%	20%	1%	0.6%	0.3%
Iodine eff. Diff. (m^2/s)	$2\ 10^{-9}$	$3.1\ 10^{-12}$	$2.8\ 10^{-11}$	$2.5\ 10^{-13}$	$1.1\ 10^{-13}$	$3.7\ 10^{-14}$
Ca eff. Diff. (m^2/s)	$2\ 10^{-9}$	$5.\ 10^{-12}$	$4.4\ 10^{-11}$	$3.9\ 10^{-13}$	$1.7\ 10^{-13}$	$5.8\ 10^{-14}$
Cs eff. Diff.(m^2/s)	$2\ 10^{-9}$	$1.3\ 10^{-11}$	$1.2\ 10^{-10}$	$1.0\ 10^{-12}$	$4.5\ 10^{-13}$	$1.5\ 10^{-13}$
Ra eff. diff. (m^2/s)	$2\ 10^{-9}$	$5.6\ 10^{-12}$	$5.0\ 10^{-11}$	$4.4\ 10^{-13}$	$1.9\ 10^{-13}$	$6.5\ 10^{-14}$
Tc eff. diff. (m^2/s)	$2\ 10^{-9}$	$3.1\ 10^{-12}$	$2.8\ 10^{-11}$	$2.5\ 10^{-13}$	$1.1\ 10^{-13}$	$3.7\ 10^{-14}$
Am eff. diff. (m^2/s)	$2\ 10^{-9}$	$3.7\ 10^{-12}$	$3.3\ 10^{-11}$	$2.9\ 10^{-13}$	$1.3\ 10^{-13}$	$4.4\ 10^{-14}$
Iodine $K_d(m^3/kg)$	0	0	0	0	0	0
Ca $K_d(m^3/kg)$	0	$2.3\ 10^{-4}$	$7.1\ 10^{-4}$	$6.7\ 10^{-5}$	$8.8\ 10^{-5}$	$4.4\ 10^{-5}$
Cs $K_d(m^3/kg)$	0	$5.2\ 10^{-2}$	$1.6\ 10^{-1}$	$1.5\ 10^{-2}$	$2.\ 10^{-2}$	$1.\ 10^{-2}$
Ra $K_d(m^3/kg)$	0	$4.6\ 10^{-2}$	$1.4\ 10^{-1}$	$1.3\ 10^{-2}$	$1.8\ 10^{-2}$	$8.8\ 10^{-3}$
Tc $K_d(m^3/kg)$	0.	0.2	0.2	0.2	0.2	0.2
Am $K_d(m^3/kg)$	0.	0.5	0.5	0.5	0.5	0.5

Table 5.6: Parameter set for task6E (fracture and the matrix zones : gouge, fracture coating, cataclasite, altered rock, non altered diorite). The parameters are the ones provided in [*Dershowitz et al. 03*]

Results

We observe the effect of the three approaches in a transport simulation of the 6 tracers, without diffusion into deeper matrix zones. We consider the 150 main fractures block. Breakthrough curves at $x = 1800m$ are provided in Fig. 5.6.

Full Type 1 and full Type 2 simulations provide bounding simulations. These two cases are indeed extreme cases for the complexity of the system. Further results show that full Type 1 and dominant type poorly differ. This means that first order fractures are larger ones mainly corresponding to Type 1. Type 2 leads to less retarded curves (as expected since fractures only bear fracture coating as compared with Type 1 bearing additional gouge and cataclasite). Quantitatively, retardation factors for Type 1 range from 7 (Iodine) to $1.5\ 10^5$ (Americium). For Type 2 complexity, the contribution of fracture coating leads to retardation factors ranging from 1.05 (Iodine) to 3000 (Americium). This retardation correspond to the sole influence of fracture coating, gouge and cataclasite. The influence of altered and non altered zones is studied below. These coefficients were obtained considering arrival times from table 5.8 and taking into account the water transit time in the system ($3.35y$).

We also observe the effect of the three approaches in a transport simulation of the 6 tracers, with matrix diffusion and with no dispersivity. We consider the 150 main fractures, Fig 5.7.

Time recoveries

The 5, 50 and 95 % time recoveries for the flux are summed up in Tab. 5.7, for the 150

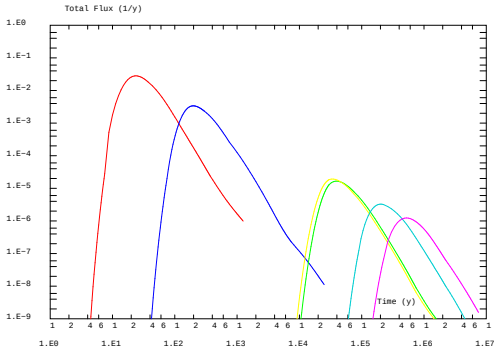

(a) Breakthrough curves for type 1 fractures

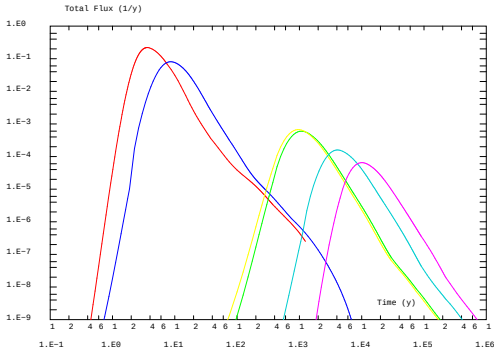

(b) Breakthrough curves for type 2 fractures

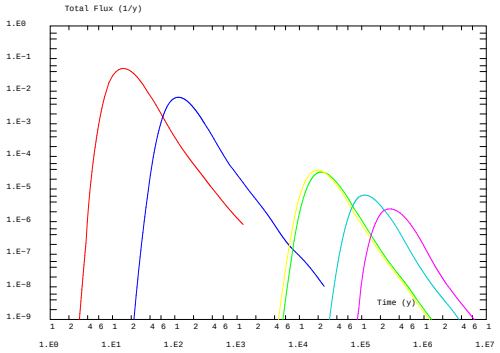

(c) Breakthrough curves for dominating type

Figure 5.6: Influence of the fracture complexity.

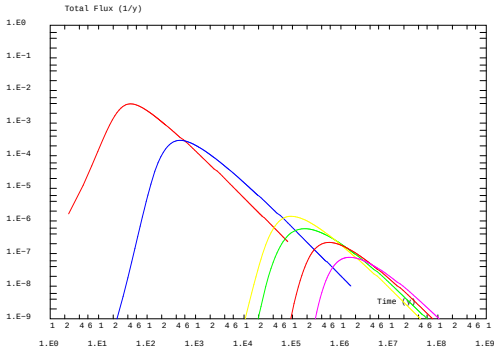

(a) Breakthrough curves for type 1 fractures

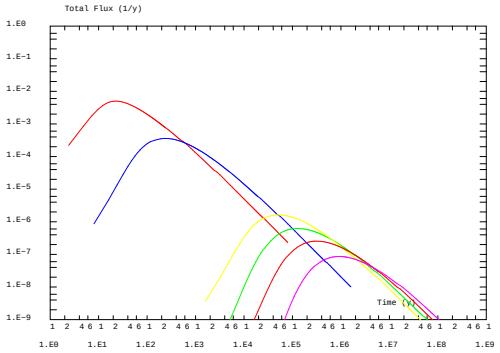

(b) Breakthrough curves for type 2 fractures

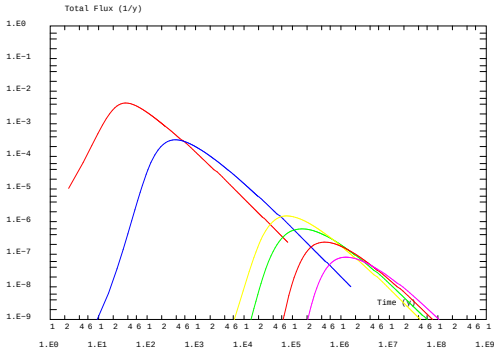

(c) Breakthrough curves for dominating type

Figure 5.7: Influence of the fracture complexity with matrix diffusion.

fractures mesh. There is no matrix diffusion in the altered and non altered matrix zone. We present the results for type 1 fractures only, and for type 2 fractures only.

Source	$T_{5\%}(y)$	$T_{50\%}(y)$	$T_{95\%}(y)$
Iodine Dirac - type 1	15	32	110
Iodine Dirac - type 2	2.5	4.8	13.5
Calcium Dirac - type 1	135	288	1000.
Calcium Dirac - type 2	5.2	11.6	36
Cesium Dirac - type 1	27000	57000	$2.0\ 10^5$
Cesium Dirac - type 2	625	1500	5250
Radium Dirac - type 1	24000.	$5\ 10^4$	$1.7\ 10^5$
Radium Dirac - type 2	560.	1300	4600
Technetium Dirac - type 1	$1.3\ 10^5$	$2.6\ 10^5$	$1.0\ 10^6$
Technetium Dirac - type 2	2400	5400	20000
Americium Dirac - type 1	$3.\ 10^5$	$7.1\ 10^5$	$2.4\ 10^6$
Americium Dirac - type 2	6300	14000	50000

Table 5.7: only type 1 fractures, and only type 2 fractures : breakthrough time history

Maximum fluxes

The maximum peak values for the flux are summed up in Tab. 5.8.

Source	**Maximal flux (1/y)**	**Time (y)**
Iodine Dirac - type 1	$2.8\ 10^{-2}(1/y)$	23
Iodine Dirac - type 2	$0.22(1/y)$	3.5
Calcium Dirac - type 1	$3.4\ 10^{-3}(1/y)$	200
Calcium Dirac - type 2	$8.1\ 10^{-2}(1/y)$	8.6
Cesium Dirac - type 1	$1.6\ 10^{-5}(1/y)$	39000
Cesium Dirac - type 2	$6.0\ 10^{-4}(1/y)$	1000.
Radium Dirac - type 1	$1.9\ 10^{-5}(1/y)$	33000
Radium Dirac - type 2	$6.7\ 10^{-4}(1/y)$	960.
Technetium Dirac - type 1	$3.3\ 10^{-6}(1/y)$	$2.0\ 10^5$
Technetium Dirac - type 2	$1.6\ 10^{-4}(1/y)$	4000.
Americium Dirac - type 1	$1.2\ 10^{-6}(1/y)$	$5.2\ 10^5$
Americium Dirac - type 2	$6.5\ 10^{-5}(1/y)$	$1.0\ 10^4$

Table 5.8: Performance measures: maximum fluxes for Dirac for the different tracers considered and with only type 1 or only type 2 fractures and no diffusion in the altered and non altered rock.

Matrix diffusion

Influence of additional matrix zones on the retention of the plume are studied in the present section. These correspond to altered and non altered zones. As detailed in chapter

3, these matrix zones are accounted for in the different ways in our model as the zones in the vicinity of the fracture plane. We first comment on the choice of the diffusion model: 1D infinite, bounded and composite. We then provide breakthrough curves and compare with the former case included only zones in the vicinity of the fracture plane.

Matrix diffusion models

Main transport characteristics

We present, Fig. 5.1.2, the tracer main transport paths, selecting only the fractures where the concentration peak is above a thousandth of the global maximum. The present system corresponds to 150 fractures with dominant type and no diffusion in deeper matrix zones. We can see that two main paths are visible. One is following the fractures 23D, 1925B, 22D, 21D, 20D, 2292B, 17S, 19D directly to the exit, where the concentration is the strongest. The second path is separated by at least 50 meters from the first one, and concentrations are a hundred times lower.

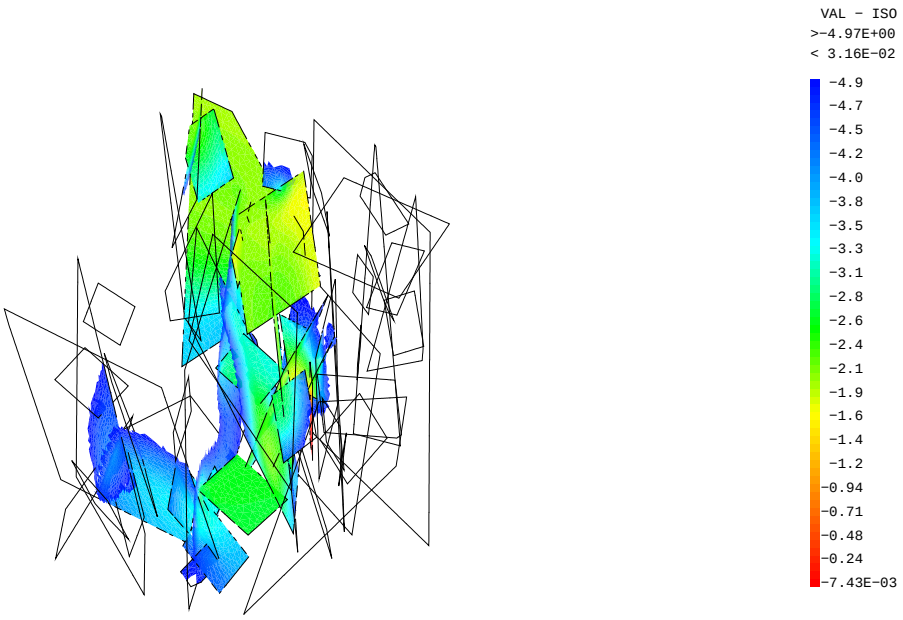

Figure 5.8: Two main flow paths as illustrated by base 10 logarithm of concentration

We have evaluated that penetration depth in the matrix is between one to 10 meters. Therefore, we can assume that the matrix diffusion process might be seen as “infinite” in the perpendicular direction to the fractures. Indeed, the concentration flux in the matrix won’t see the influence of surrounding fractures.

We hence consider a 1 dimensional diffusion in the matrix. We consider three approaches as presented in chapter 3:

- We consider only one kind of rock (unaltered) and an infinite 1D media seen by the fracture. We use Green function to calculate the semi-analytical solution of the diffusion transport equation of tracers in this simplified matrix.

- We consider also one 1D layer in the rock, but with a limited extension (a fixed length is given). We impose a no flux condition on that boundary. We also derive a semi analytical solution based on Green functions.

- We consider a 1D layer of altered granite of fixed length, followed by a 1D infinite layer of unaltered rock. The analytical solutions are also calculated.

The last situation corresponds to the actual conditions where altered rock zone is present over 20 cm before large non altered depths. The two first cases are implemented for sake of comparisons.

The former analytical solution can be coupled implicitly with the transport discretization system. More details are given in section 3.

Comparisons

Results show that composite medium behaves similarly as the homogeneous unbounded case when non altered properties are considered. This is due to the fact that penetration depth is large compared with the 20 cm associated with altered rock. For the same reason, bounded matrix considering 20 cm of altered rock properties differs strongly from the composite medium showing that modeling of non altered rock is of first importance.

We show similarly that matrix diffusion in deeper matrix zones (altered and non altered zones) is of major importance in the system by comparing the former results limiting matrix to zones in the vicinity of the fracture plane (see Fig. 5.6) to Fig. 5.7 providing similar configurations with additional composite matrix model.

Results show that the matrix diffusion in altered and non altered zones has a strong influence on the retention properties associated with the breakthrough curves. To quantify the difference, we present the time recoveries and maximum fluxes obtained in these different cases.

Time recoveries

The 5, 50 and 95 % time recoveries for the flux are summed up in Tab. 5.9, for the 150 fractures mesh.

We notice an influence of a factor 3 up to 10 for the 5 % time recoveries. This influence is reaching a factor 50 for the 50 % time recoveries and goes over 200 for the 95 % time recoveries.

It then appears than the matrix diffusion has a very strong influence on the results, especially at the large time scales (95 % time recoveries) when the penetration length into the matrix is maximum.

Source	$T_{5\%}(y)$	$T_{50\%}(y)$	$T_{95\%}(y)$
Iodine Dirac - no diff	8.7	18	56
Iodine Dirac - diff	26	260	42000
Calcium Dirac - no diff	75	150	475
Calcium Dirac - diff	310	3840	$6.4\ 10^5$
Cesium Dirac - no diff	15000	30000	$1.0\ 10^5$
Cesium Dirac - diff	$1.4\ 10^5$	$2.1\ 10^6$	$> 1.6\ 10^8$
Radium Dirac - no diff	13000.	$2.6\ 10^4$	$87\ 10^3$
Radium Dirac - diff	64000.	$8.6\ 10^5$	$1.4\ 10^8$
Technetium Dirac - no diff	$7.5\ 10^4$	$1.5\ 10^5$	$4.9\ 10^5$
Technetium Dirac - diff	$4.0\ 10^5$	$5.5\ 10^6$	$> 4.8\ 10^8$
Americium Dirac - no diff	$1.8\ 10^5$	$3.7\ 10^5$	$1.2\ 10^6$
Americium Dirac - diff	$1.1\ 10^6$	$1.4\ 10^7$	$> 4.8\ 10^8$

Table 5.9: With and without matrix diffusion in deeper altered and non altered zones: breakthrough time history

Maximum fluxes

The maximum peak values for the flux are summed up in Tab. 5.10.

Source	Maximal flux (1/y)	Time (y)
Iodine Dirac - no diff	$4.9\ 10^{-2}(1/y)$	15
Iodine Dirac - diff	$4.3\ 10^{-3}(1/y)$	37
Calcium Dirac - no diff	$6.5\ 10^{-3}(1/y)$	110
Calcium Dirac - diff	$3.2\ 10^{-4}(1/y)$	360
Cesium Dirac - no diff	$3.3\ 10^{-5}(1/y)$	23000
Cesium Dirac - diff	$5.6\ 10^{-7}(1/y)$	$1.5\ 10^5$
Radium Dirac - no diff	$3.7\ 10^{-5}(1/y)$	19000
Radium Dirac - diff	$1.5\ 10^{-6}(1/y)$	76000
Technetium Dirac - no diff	$6.5\ 10^{-6}(1/y)$	$1.1\ 10^5$
Technetium Dirac - diff	$2.3\ 10^{-7}(1/y)$	$4.4\ 10^5$
Americium Dirac - no diff	$2.4\ 10^{-6}(1/y)$	$2.8\ 10^5$
Americium Dirac - diff	$8.1\ 10^{-8}(1/y)$	$1.2\ 10^6$

Table 5.10: Performance measures: maximum fluxes for Dirac for the different tracers considered and with or without matrix diffusion.

We observe up to more than a factor 20 of difference on peaks and factor on the associated times ranging from 3 to 6. The differences observed are in good agreement with the short (5 %) and average (50 %) time recoveries.

Analysis of the impact of matrix diffusion

Former results show that matrix diffusion plays a dominant role in the retention process. The overall contribution of matrix diffusion to retention processes can be first estimated comparing the peak arrival times for the whole system (dominant type and altered and non altered rock) as compared with the initial fracture network without matrix diffusion. The base case leads to arrival time of the peak by 3.3 years. Peak arrival times for the whole system range from $37y$ for the non sorbing tracer (iodine) to 1.210^6y in the case of the most sorbing tracer (americium). Refer to table 5.7. The overall retardation as regard to the peak arrival time corresponds to roughly an order of magnitude. Sorbing effects strengthen retardation effects in a multiplicative manner. The influence of matrix diffusion as a retention process can be estimated from the larger times of the breakthrough curve. Indeed, the impact of matrix diffusion on peak arrival times is relatively moderate as compared with retardation of for instance $t_{95\%}$ (arrival time of 95% of the injected mass). Table 5.9 shows that later time arrival of mass is very strongly delayed. Recovering of 95% of the mass corresponds to $11.7y$ for the sole fracture network and rises to $4200y$ for iodine and is larger than 4.810^8y in the case of americium. This result is classical for the impact of matrix diffusion and is referred as tailing effect.

More detailed comments can be made on matrix diffusion impact by considering the effects related with matrix zones in the vicinity of the fracture and matrix zones in the depth of the rock. The first are homogenized as a retardation factor in our model (fracture coating + gouge + cataclasite for Type 1 and fracture coating for Type 2), the second (altered and non altered rock) are explicitly modeled by a semi analytical term in the equations. Results are provided above while gradually including the various matrix zones:

- Inclusion of matrix zones in the vicinity of the conductive fracture is conducted considering pure Type 1 (fracture coating, gouge, cataclasite) versus pure Type 2 (fracture coating). Refer to figures 5.6 and tables 5.7, 5.8.
- Inclusion of matrix zones more in the depth of the matrix blocks in addition to the dominant type (altered and non altered rock). Refer to preceding section, figures 5.7 and tables 5.9 and 5.10.

Results corresponding to the first kind of zones show that the dominant type is close to the pure Type 1 case. Peak arrival times are roughly less than half way behind. Inclusion of dominant type leads to retardation factors on peak arrival times ranging from 5 (see $15y$ for iodine in table 5.10) to roughly 10^5 (see $2.8\,10^5$ for americium in the same table). We sum up the results from Table 5.10 in terms of retardation coefficient (labeled here R') in Table 5.11 in the column retardation coefficients from simulations.

Results corresponding to the second kind of zones are provided in the same table 5.10. Here, the overall retardation on the peak arrival time of all matrix zones ranges from roughly 10 for iodine to 4.10^5 for americium. The specific effect of altered and non altered rock can be derived recalling that retardation is additive for both effects. In

consequence the retardation for Iodine corresponds to $R'' = (37. - 15.)/3.35$ which is in value close to a factor 7. The retardation coefficients associated with the impact of altered and non altered zones are summed up in table 5.12, in the column retardation coefficients from simulations.

Results show that both groups of matrix zones (close to the conductive feature or further) have quantitatively comparative impact on the peak arrival times. Nevertheless, altered and non altered zones in the depth of the matrix lead to roughly twice larger retardation coefficients on peak arrival times as fracture coating, gouge and cataclasite situated in the vicinity of the conducting feature. Moreover, altered and non altered rock leads to strong tailing effects on breakthrough curves so that the impact of the zones on late arrival of mass (ie $T_{95\%}$ is much larger than can be read from peak arrival times. So, the overall retardation and modification of shape of the breakthrough curves is mainly impacted by the properties of altered and non altered rock masses in the depth of the rock. This effect is bound to be even stronger for slower transfers related with lower permeability blocks.

In tables 5.11 and 5.12, we try to approximate the results in terms of retardation coefficients read on the simulated curves by simple analytical models related with single fracture systems. This approach is potentially interesting here since we proved that a limited number of fractures is responsible for transfers in the block studied. So the question is can we approximately guess the level of retardation coefficients for the travel path based on a single fracture analytical expression.

For Type 1 and Type 2 complexities, the impact of fracture coating, gouge and cataclasite are accounted for in the model by means of a retardation coefficient associated with each fracture. This was presented in section 3, with equation 6.1 recalled below. In the same line R' are calculated as follows for a single fracture aperture by $1.5\ 10^{-4}m$:

$$R' = 1 + \frac{1}{b} \sum_i \omega_i d_i R_i. \tag{5.3}$$

R_i is the retardation coefficient in the matrix zone i, d_i its thickness, ω_i its porosity and b the fracture aperture. Summation is over fracture coating properties alone for Type 2 but on fracture coating, gouge and cataclasite for Type 1. Results for this fracture aperture are provided as retardation coefficients estimated on table 5.11. Results show an overall good agreement between simulated and estimated retardation coefficients. As contemplated, quantitative differences are observed, but ranges are acceptable. As a consequence these easy analytical expressions are a valuable help to estimate retardation of peak arrival times.

The same is attempted for retardation related with altered and non altered zones. As explained in section 3, these zones are modeled as diffusion zones. Estimation of the impact of matrix diffusion on arrival times can be attempted based on simple analytical expressions. Starting from the solution of transfer of mass in a single fracture with pure advection and 1D infinite matrix diffusion, the position of the concentration peak is

derived. The associated expression follows:

$$R = (R' + R'')t_w \tag{5.4}$$

where R' corresponds to surface sorption retardation coefficient, R'' to the retardation associated with matrix diffusion and t_w is water transit time in the system. R'' expresses as follows:

$$R'' = 1 + \frac{2}{3}\frac{\omega^2 dR}{b^2}t_w \tag{5.5}$$

with ω porosity and d pore diffusion coefficient of matrix zone, R bulk retardation coefficient, b fracture aperture. This expressions involves t_w so it is not a classical retardation coefficient but takes into account the fact that retardation of peak arrival time for such a system is proportional (for large enough effects) to the length of the system. R'' coefficients were calculated for all tracers, for fracture aperture by $1.5\,10^{-4}$ and the observed water travel time ($3.35y$). We consider altered rock and non altered rock properties since matrix zones are indeed heterogeneous although our analytical expression was obtained for an homogeneous matrix. Results are provided on table 5.12. They show that approximate evaluation of the retardation of the peak arrival time is possible. The range of values as from simulations is indeed bounded by estimations relying upon altered and non altered properties.

As a consequence such simple analytical expressions are valuable helps in estimating the importance of retardation of peak arrival times as resulting from complex matrix zones. Nevertheless the impact of matrix zones in the depth of the rock leads as well to strong tailing effect not described by our analytical expressions limited to peak arrival times.

The selected reference model

Based on the previous studies, we consider the following model as our reference model for the PA calculations :

- The largest 1200 fractures where flow and transport calculations are converged, see chapter 5.1.1.
- 2.5 meters cells in order to achieve good numerical accuracy of the calculation (less than 10 % of numerical error).
- A small dispersivity of 2.5 meters which has very little influence on the results.
- For the complexity, we consider the dominating type of the fractures.
- The matrix diffusion is a 1D model with one bounded layer of altered rock (20 cm), followed by one infinite layer of unaltered rock.
- Fracture aperture, efficient diffusivities, permeabilities ..., are issued from task specifications and previous tasks reports (6C).

R'	Ret. coef. Simul.	Ret. coef. Estim.
Iodine Pure Type 1	7.	9.2
Iodine Dominant Type	4.5	–
Iodine Pure Type 2	1.05	1.2
Calcium Pure Type 1	60.	86.2
Calcium Dominant Type	433	–
Calcium Pure Type 2	2.6	3.2
Cesium Pure Type 1	$1.2\,10^4$	17320.
Cesium Dominant Type	$7.\,10^3$	–
Cesium Pure Type 2	300.	445.8
Radium Pure Type 1	10^4	$1.5\,10^4$
Radium Dominant Type	$5.7\,10^3$	–
Radium Pure Type 2	287.	394.
Technetium Pure Type 1	$6.\,10^4$	$8.7\,10^4$
Technetium Dominant Type	$3.2\,10^4$	–
Technetium Pure Type 2	1200.	1711.
Americium Pure Type 1	$1.55\,10^5$	$2.18\,10^5$
Americium Dominant Type	$8.3\,10^4$	–
Americium Pure Type 2	3000.	4276.2

Table 5.11: Estimation of retardation coefficients from the simulations as compared with analytical estimations: role of zones in the vicinity of the conducting fracture. Fracture opening by $1.5\,10^{-4}m$, water arrival time by $3.35y$.

R"	Ret. coef. simul.	Ret. coef. estim. Altered	Ret. coef. estim. Non Alt.
Iodine	7	9.8	2.5
Calcium	50	355.8	61.4
Cesium	$3.8\,10^4$	$7.9\,10^4$	$1.3\,10^4$
Radium	$1.7\,10^4$	$7.1\,10^4$	$1.1\,10^4$
Technetium	10^5	$7.9\,10^5$	$2.7\,10^5$
Americium	$2.8\,10^5$	$2.\,10^6$	$6.7\,10^5$

Table 5.12: Estimation of retardation coefficients from the simulations as compared with analytical estimations: role of zones in the depth of the matrix blocks. Fracture opening by $1.5\,10^{-4}m$, water arrival time by $3.35y$.

Calculations are achieved with time scales allowing 95 % recovery of the tracers, except for the 2 slowest tracers, for which the calculation is stopped slightly before. Indeed, we didn't simulate on more than a hundred million years, since it has not much physical sense : the recovery time wouldn't be meaningful if we would consider the radioactive decay.

A simplified PA model

We also tried simplifying the geometry as far as possible with only secondary order decrease of the quality of the performance measures. Flow and transport are simulated from this simplified geometry. The process leading to a final 12 fracture system is detailed in the following subsections.

Selection of the main fractures

For the transport

We calculate the mass contained in each fracture, versus time. We sort out the mass peaks by decreasing order. This is done on the 1200 fracture system. We obtain the following sequence :

$$23D- > 1925B- > 22D- > 21D- > 20D- > 2292B- > 17S- > 19D- > ... \tag{5.6}$$

The 19D fracture is intersecting the exit of the block ($x = 1800m$). These fractures are all connected, therefore we have a straight path from the 23D to the exit. The mass peak at the exit is nearly 1000 times smaller that in the 23D. The left aside fractures (following the 19D by decreasing order) contain a very few fraction of the mass. We will show below that they indeed have a minor role in the radionuclide transport by comparison with simulations of the 1200 fractures system.

We decide to keep only these 8 fractures to define the simplified PA model.

For the flow

We also want to simplify the system of fractures of importance for the flow. Of course we have to retain the fractures important for the transport, plus the one allowing a connection between the storage (fracture 23D) and the upstream boundary of the block.

We established the flow flux in the fractures and also sort them in decreasing order. We then keep the minimum amount of fractures allowing a connectivity between the boundaries $x = 1800m$, $x = 2000m$ and the storage (23D). We therefore add the fractures 13S, 5D, 7S, 10D and 8S, and also the 2101C, whose importance had been illustrated in previous chapters.

The simplified model

Everything remains the same as for the full 1200 fractures network, except that we now only use the 14 selected fractures both for the flow and the transport calculations.

Actually, numerical simulations have demonstrated that fractures 8S and 10D have no influence on the transport. These two fractures correspond the second path, visible on Fig. 5.1.2, which is not going through the storage (23D). Their presence has also only a minor influence on the flow running through the storage.

Finally, we consider the 12 fracture system: 23D, 1925B, 22D, 21D, 20D, 2292B, 17S, 19D, 13S, 5D, 7S and 2101C for the PA model. This network of fractures runs

obviously much faster on a computer since the amount of fractures is a hundred times less than the 1200 fractures system.

Comparisons with this PA model and the 1200 fractures network are presented in the following chapter.

5.2 Results

We present the results obtained on a very simplified 12 fractures PA model and the 1200 fractures PA model. We first describe the flow path in the block, then the transport results for the reference approach and the simplified one.

5.2.1 Flow

Description of the fbw paths

The main characteristics of the flow have been described in Sec. 5.1.2. We present in the following subsections, the residence time for the water and its breakthrough time history.

Residence time

In order to determinate the water residence time, we consider the following transport model:

- A diffusion-convection transport equation with no dispersion (ie dispersion equal to the cell size).
- No matrix diffusion.
- A retardation coefficient equals to 1.
- The given fracture aperture (files features.doc provided with this task).
- No sorbing properties.

Breakthrough time history for the water

We present the breakthrough time history for the water, Fig. 5.9. The maximum peak of outflow (at $x = 1800m$) is obtained at 3.35 years. The maximum is 0.23 1/y for a Dirac mass pulse on non sorbing tracer following the above defined requirements.

Time recoveries

The time recoveries at $x = 1800m$ are :

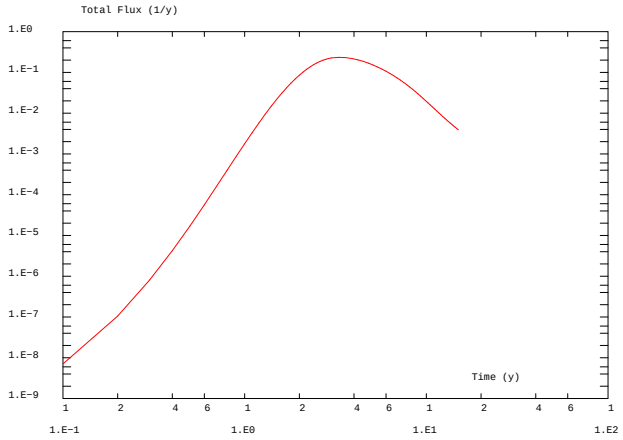

Figure 5.9: Breakthrough curves for water

- 2.1 years to recover 5 % of the injected mass.
- 4.2 years to recover 50 % of the injected mass.
- 11.7 years to recover 95 % of the injected mass.

5.2.2 Transport - reference model

We consider here the release of a unit mass at the initial simulation time. The mass is located in the mesh corresponding to the input, in the 23D feature.

We show :

- Breakthrough curves at three different planes (x=1920 m, x=1880 m, x= 1800 m). These correspond to the total mass exiting the system.
- Maximum release rate for Dirac input.
- Breakthrough time recovery (5, 50 and 95 percents of the injected mass).

The graphs are provided as required in the specifications : in log-log scale in a frame 20cm * 12cm.

For each tracer, we associate a color as follows:

- Blue for Iodine
- Red for Calcium
- Green for Cesium

- Yellow for Radium
- Cyan for Technetium
- Magenta for Americium

Breakthrough time history for the tracers

The breakthrough time history for the six tracers considered are provided on figure 5.10. The order of arrival is related with the sorbing properties of each tracer : first Iodine, then Calcium, Radium, Cesium, Technetium, Americium.

Maximum release rates

Maximum release rates as well as the time associated with the peak are provided on Table 5.13. The order of arrival follows the importance of the sorption phenomenon of the tracer considered.

Source	Maximal flux	Time (y)
Iodine Dirac - $x = 1920m$	$2.4\ 10^{-2}(1/y)$	4.8
Iodine Dirac - $x = 1880m$	$6.6\ 10^{-3}(1/y)$	22
Iodine Dirac - $x = 1800m$	$4\ 10^{-3}(1/y)$	35
Calcium Dirac - $x = 1920m$	$2.4\ 10^{-3}(1/y)$	21
Calcium Dirac - $x = 1880m$	$5.1\ 10^{-4}(1/y)$	195
Calcium Dirac - $x = 1800m$	$3.0\ 10^{-4}(1/y)$	380
Cesium Dirac - $x = 1920m$	$5.2\ 10^{-6}(1/y)$	7500
Cesium Dirac - $x = 1880m$	$9.8\ 10^{-7}(1/y)$	$84\ 10^{3}$
Cesium Dirac - $x = 1800m$	$5.4\ 10^{-7}(1/y)$	$1.6\ 10^{5}$
Radium Dirac - $x = 1920m$	$1.2\ 10^{-5}(1/y)$	4300
Radium Dirac - $x = 1880m$	$2.4\ 10^{-6}(1/y)$	$4.2\ 10^{4}$
Radium Dirac - $x = 1800m$	$1.4\ 10^{-6}(1/y)$	$8.0\ 10^{4}$
Technetium Dirac - $x = 1920m$	$2.0\ 10^{-6}(1/y)$	$1.9\ 10^{4}$
Technetium Dirac - $x = 1880m$	$3.8\ 10^{-7}(1/y)$	$2.4\ 10^{5}$
Technetium Dirac - $x = 1800m$	$2.1\ 10^{-7}(1/y)$	$4.7\ 10^{5}$
Americium Dirac - $x = 1920m$	$7.1\ 10^{-7}(1/y)$	$3.4\ 10^{4}$
Americium Dirac - $x = 1880m$	$1.3\ 10^{-7}(1/y)$	$6.3\ 10^{5}$
Americium Dirac - $x = 1800m$	$7.4\ 10^{-8}(1/y)$	$1.2\ 10^{6}$

Table 5.13: Performance measures: maximum fluxes for Dirac for the different tracers considered. 3 control planes. 1200 fractures.

Time recoveries

The 5, 50 and 95 % time recoveries for the flux are summed up in Tab. 5.14.

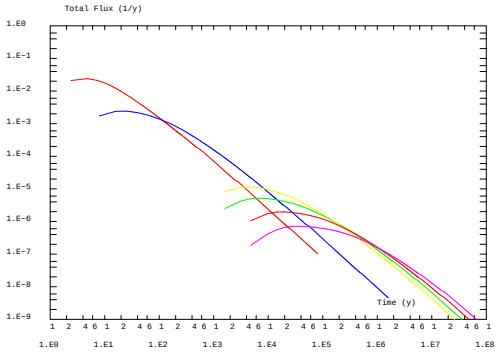

(a) Breakthrough curves $x = 1920m$ - Dirac pulse

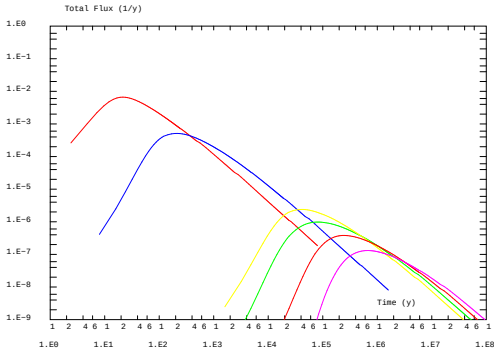

(b) Breakthrough curves $x = 1880m$ - Dirac pulse

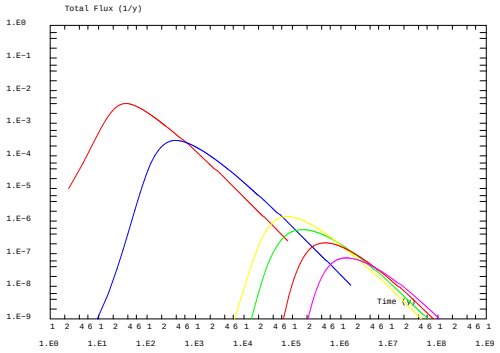

(c) Breakthrough curves $x = 1800m$ - Dirac pulse

Figure 5.10: Breakthrough curves at 3 different locations - 1200 fractures model

Source	$T_{5\%}(h)$	$T_{50\%}(h)$	$T_{95\%}(h)$
Iodine Dirac - 1920 m	**	50	12 10^3
Iodine Dirac - 1880 m	14	177	26 10^3
Iodine Dirac - 1800 m	28	300	48 10^3
Calcium Dirac - 1920 m	16	700	1.8 10^5
Calcium Dirac - 1880 m	170	2500	4.10^5
Calcium Dirac - 1800 m	336	4400	7.2 10^5
Cesium Dirac - 1920 m	9600	3.9 10^5	1.08 10^8
Cesium Dirac - 1880 m	8 10^4	1.4 10^6	$>$ 1.6 10^8
Cesium Dirac - 1800 m	1.5 10^5	2.4 10^6	$>$ 1.6 10^8
Radium Dirac - 1920 m	4800.	1.5 10^5	4.2 10^7
Radium Dirac - 1880 m	36. 10^3	5.5 10^5	8.8 10^7
Radium Dirac - 1800 m	68. 10^3	9.6 10^5	$>$ 1.6 10^8
Technetium Dirac - 1920 m	24 10^3	9.8 10^5	2.6 10^8
Technetium Dirac - 1880 m	2.3 10^5	3.6 10^6	$>$ 4.8 10^8
Technetium Dirac - 1800 m	4.3 10^5	6.2 10^6	$>$ 4.8 10^8
Americium Dirac - 1920 m	72 10^3	2.9 10^6	$>$ 4.8 10^8
Americium Dirac - 1880 m	6.3 10^5	1.1 10^7	$>$ 4.8 10^8
Americium Dirac - 1800 m	1.2 10^6	1.7 10^7	$>$ 4.8 10^8

Table 5.14: Breakthrough time history at $x = 1920$ m, $x = 1880$ m and $x = 1800$ m. 1200 fractures reference model. Dirac pulse.

5.2.3 Sensitivity analysis - simplified PA model

Same specifications are met for graphs. Results for the 12 fractures simplified model are presented in the following subsections.

Breakthrough time history for the tracers

The breakthrough time history for the six tracers considered are provided on figure 5.11. The order of arrival is related with the sorbing properties of each tracer : first Iodine, then Calcium, Radium, Cesium, Technetium, Americium.

A first look at the results show that breakthrough curves corresponding to the 1200 fracture case (Fig. 5.10) and the 12 fracture case (see Fig. 5.11) are surprisingly similar. A deeper look provides quantitative differences for all tracers and performance measurements by roughly 10%. The 12 fracture system provides somewhat broader curves mainly corresponding to quicker arrival times and slight longer tailing. These features could be explained by the simplified structure of the flow providing different arrival times. The longer tailing of the curves might be in relation with the amount of smaller fractures which are not of first order importance for the flow but provide intermediate storage zones to the tracers corresponding with overall retention effect.

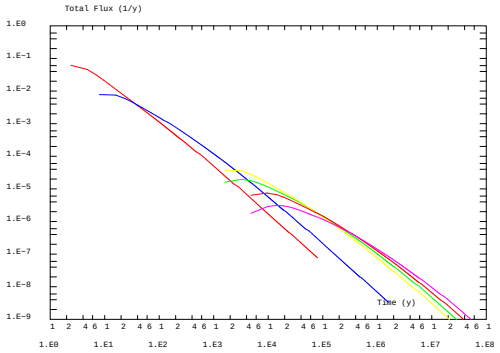

(a) Breakthrough curves $x = 1920m$ - Dirac pulse

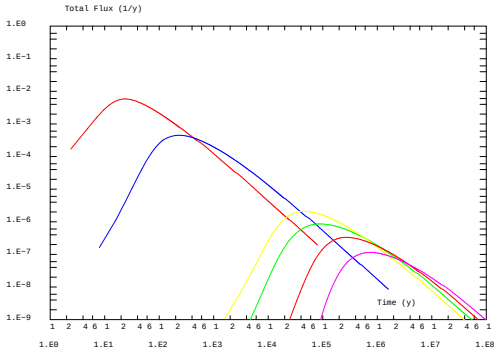

(b) Breakthrough curves $x = 1880m$ - Dirac pulse

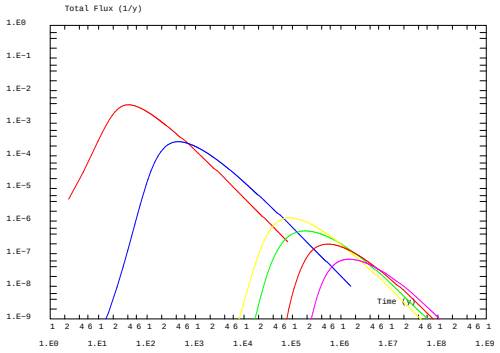

(c) Breakthrough curves $x = 1800m$ - Dirac pulse

Figure 5.11: Breakthrough curves at 3 different locations - 12 fractures model

Maximum release rates

Maximum release rates as well as the time associated with the peak are provided on Table 5.15. The order of arrival follows the importance of the sorption phenomenon of the tracer considered.

Source	Maximal flux	Time (y)
Iodine Dirac - $x = 1920m$	$6.2\ 10^{-2}(1/y)$	2.3
Iodine Dirac - $x = 1880m$	$5.8\ 10^{-3}(1/y)$	23
Iodine Dirac - $x = 1800m$	$3.7\ 10^{-3}(1/y)$	38
Calcium Dirac - $x = 1920m$	$7.8\ 10^{-3}(1/y)$	9.0
Calcium Dirac - $x = 1880m$	$4.5\ 10^{-4}(1/y)$	220
Calcium Dirac - $x = 1800m$	$2.7\ 10^{-4}(1/y)$	420
Cesium Dirac - $x = 1920m$	$1.9\ 10^{-5}(1/y)$	3300
Cesium Dirac - $x = 1880m$	$8.6\ 10^{-7}(1/y)$	$86\ 10^{3}$
Cesium Dirac - $x = 1800m$	$5.0\ 10^{-7}(1/y)$	$1.8\ 10^{5}$
Radium Dirac - $x = 1920m$	$3.7\ 10^{-5}(1/y)$	1700
Radium Dirac - $x = 1880m$	$2.1\ 10^{-6}(1/y)$	$4.7\ 10^{4}$
Radium Dirac - $x = 1800m$	$1.3\ 10^{-6}(1/y)$	$8.6\ 10^{4}$
Technetium Dirac - $x = 1920m$	$7.5\ 10^{-6}(1/y)$	$9.5\ 10^{3}$
Technetium Dirac - $x = 1880m$	$3.3\ 10^{-7}(1/y)$	$2.6\ 10^{5}$
Technetium Dirac - $x = 1800m$	$2.0\ 10^{-7}(1/y)$	$5.3\ 10^{5}$
Americium Dirac - $x = 1920m$	$3.1\ 10^{-6}(1/y)$	$1.5\ 10^{4}$
Americium Dirac - $x = 1880m$	$1.15\ 10^{-7}(1/y)$	$6.8\ 10^{5}$
Americium Dirac - $x = 1800m$	$6.8\ 10^{-8}(1/y)$	$1.4\ 10^{6}$

Table 5.15: Performance measures: maximum fluxes for Dirac for the different tracers considered. 3 control planes. 12 fractures.

We notice that for the $x = 1920m$ peaks amplitude are about twice up to three times greater than for the 1200 fractures network. Whereas, arrival times are twice up to three times smaller, which somehow logical: less matrix diffusion occurs if the flow is faster in the fractures. The agreement is poor between both models. Nevertheless, for the $x = 1880m$ and $x = 1800m$ planes, results between the two models are in good agreement. For the $x = 1800m$ case, differences are around 10% for peak arrival time and less than 10% for peak level.

This indicates that our simplified model doesn't capture well enough the complex structure of the network close to the storage (23D). Indeed, observing the results very close to the storage leads to smaller time scales (the transfer time involved is up to a hundred times less than at the exit $x = 1800m$). Advection is then dominant over matrix diffusion, and a refined representation of the fracture network is required. On the other hand, for longer distances corresponding to block size, simulations show that the main features of the simplified model are sufficient to characterize the transport.

The following section confirms these results.

Time recoveries

The 5, 50 and 95 % time recoveries for the flux are summed up in Tab. 5.16.

Source	$T_{5\%}(h)$	$T_{50\%}(h)$	$T_{95\%}(h)$
Iodine Dirac - 1920 m	**	19.2	$4.4\ 10^3$
Iodine Dirac - 1880 m	17	199	$30\ 10^3$
Iodine Dirac - 1800 m	31	300	$42\ 10^3$
Calcium Dirac - 1920 m	**	240	$6.4\ 10^4$
Calcium Dirac - 1880 m	190	2900	$4.5\ 10^5$
Calcium Dirac - 1800 m	360	4400	$6.4\ 10^5$
Cesium Dirac - 1920 m	1600	$1.3\ 10^5$	$3.9\ 10^7$
Cesium Dirac - 1880 m	$8.8\ 10^4$	$1.6\ 10^6$	$> 1.6\ 10^8$
Cesium Dirac - 1800 m	$1.6\ 10^5$	$2.4\ 10^6$	$> 1.6\ 10^8$
Radium Dirac - 1920 m	900.	$5.2\ 10^4$	$1.5\ 10^7$
Radium Dirac - 1880 m	$40.\ 10^3$	$6.2\ 10^5$	$1.0\ 10^8$
Radium Dirac - 1800 m	$76.\ 10^3$	$9.6\ 10^5$	$1.4\ 10^8$
Technetium Dirac - 1920 m	$4.8\ 10^3$	$3.2\ 10^5$	$9.6\ 10^7$
Technetium Dirac - 1880 m	$2.5\ 10^5$	$4.0\ 10^6$	$> 4.8\ 10^8$
Technetium Dirac - 1800 m	$4.6\ 10^5$	$6.2\ 10^6$	$> 4.8\ 10^8$
Americium Dirac - 1920 m	$14\ 10^3$	$9.8\ 10^5$	$2.8\ 10^8$
Americium Dirac - 1880 m	$7.2\ 10^5$	$1.2\ 10^7$	$> 4.8\ 10^8$
Americium Dirac - 1800 m	$1.3\ 10^6$	$1.7\ 10^7$	$> 4.8\ 10^8$

Table 5.16: Breakthrough time history at $x = 1920$ m, $x = 1880$ m and $x = 1800$ m. 12 fractures simplified PA model. Dirac pulse.

Results provide similar trends as for the previous section. Results are in good agreement (within 10 %) between the two models at long enough distance from the storage (23D). Closer to the storage (x=1920 m), and especially at short times (for example 5 % recoveries), the results are not in good agreement. We then obtain recovery times up to 5 times faster for the simplified 12 fractures network. Contribution of some minor local conductors should then be included in the model.

Conclusions

Overall results show that for breakthrough curves at the limits of the domain, the simplified 12 fracture system is sufficient to provide all first order features. The precision for all performance measures is indeed met by 10%. This result might appear at first surprising. One should nevertheless stress that several factors tend to allow for an acceptable simplified system:

- The connectivity among the fracture network remains limited. From the overall fracture network a limited number is hydrologically connected.

- The boundary conditions tend to connect input and output side of the block while no flow conditions on the sides does not allow for important fractures crossing them to provide with flow from the sides. A limited number of flow paths are as such selected and there is only limited mixing with flow from side fractures.

- Matrix diffusion is here a dominant effect as compared with advection for quicker flow regimes. The high quality of the simulation based on the simplified geometry could partly result from the fact that the transport operates for slow velocities. More in depth studies of travel paths would nevertheless be required to verify this assessment.

Nevertheless lower quality of the fits for the breakthrough curve close to the source ($x = 1920m$) shows that the equivalence on lower averaging volumes is not quite achieved.

It should be nevertheless stressed that the 12 fracture system was obtained based on observation of main conductors and travel paths from larger systems. The simplification provided actually relies upon intrinsic properties of the block (and associated boundary conditions). Further reduction of the system with the aim of only accounting for the reference system breakthrough curves could be attempted. This kind of black box approach (though possibly on a physical base like N fractures in series involving M fractures in parallel) was not considered here. This could provide with a less computer intensive model providing good precision results. But this would be achieved at the expense of the generality of the cases considered and of the understanding of the transport mechanisms.

5.2.4 Sensitivity analysis - boundary conditions

Former results show that a surprisingly limited amount of fractures (12) from the roughly 6000 initial block are sufficient to represent the main features of the transfer in the block. This is potentially related with the geometrical features of the fractured network. In particular, connectivity does not significantly increase with introduction of additional smaller fractures.

Another source of explanation for this situation can be researched as well in the boundary conditions imposed to the block. Indeed the boundary conditions of no flow on all sides except the input and output sides of the cubic block potentially lead to the selection of a small amount of travel paths, here mainly one single major travel path. Allowing water to flow from the sides of the domain could potentially influence the transfers in the block at least by allowing freshwater to mix at the intersection of side fractures with the main travel path. In consequence we study in the following the transfer in the block for different boundary conditions. In particular, in section 5.2.4, we consider similar flow conditions as in the deliveries but resulting from linear heads at the limits of the domain. We further take some time to study the transfer in the block for a series of other uniform flow conditions along other sides of the block (two orthogonal horizontal directions, vertical direction, in one direction and its opposite, for no flow boundaries on the sides of the

cube). These studies are intended to understand former results and gain understanding in the properties of the block.

Another source of explanation for the limitation of the main transfer to a single dominant transport path is related with the limited size of the source. A larger source term would put mass on a larger variety of flow lines and possibly increase the dispersion in the fracture network. In addition, this situation is expected for a real storage facility where the volume of the storage is large leading to an extended source term as compared with local fracturation scale. Studying the transfer properties of the present block for extended initial source would be straightforward with the present model. Nevertheless this was not done due to time constraints but is contemplated for the future.

In the following we study the properties of the block by varying the boundary conditions of the block while maintaining the same level of head gradient (vary the type of boundary condition on the sides of the cube, vary head gradient orientation and directions). These studies are intended to be a first step in the study of the transport properties of the block and require further efforts to be finalized. This could not be done due to time constraints.

Other boundary conditions, for similar flow conditions

We modified the flow boundary conditions considering the 1200 fracture system implemented previously. We apply constant head gradient (the head is still varying from 0 to 1) along the x axis on the boundaries of the domain. The only change compared to the original problem is that we are not blocking the flow anymore on the sides of the block which are perpendicular to the x axis. Indeed instead of considering no flow side conditions we allow flow to come in and out on the sides of the system. Head vary linearly on the boundaries of the cubic domain. Mean head gradient is the same as in the case considered in the deliveries.

Breakthrough curves associated with the former no flow conditions and the present are provided on figure 5.12.

Time recoveries

The 5, 50 and 95 % time recoveries for the flux are summed up in Tab. 5.17, for the 1200 fractures mesh.

Maximum fluxes

The maximum peak values for the flux are summed up in Tab. 5.18.

Results

Results show that peak arrival times are twice larger than for the nominal case and maximal flux twice smaller (see Table 5.10). Breakthrough curves are skipped to the larger times with larger impact than a factor of 2 on the time of arrival of 95% of mass injected.

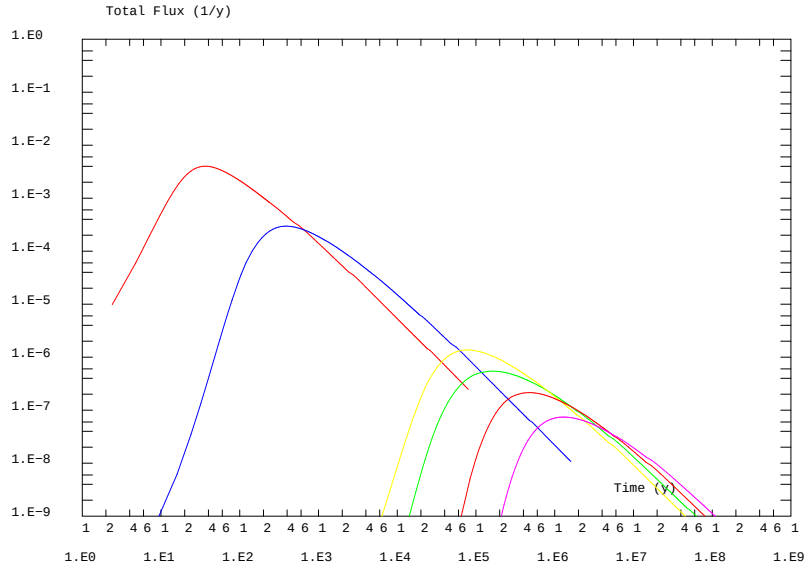

(a) No flow side boundary conditions (reference case)

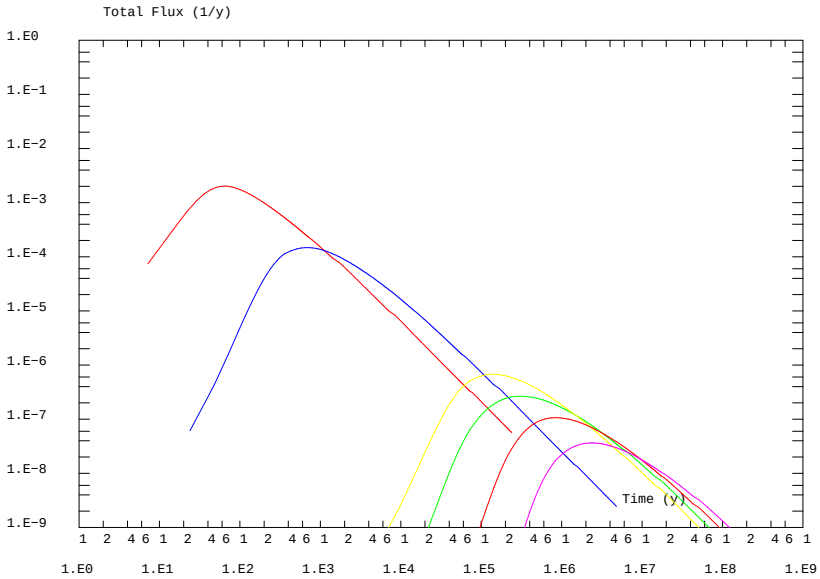

(b) Side boundary conditions allowing flow transfers

Figure 5.12: Breakthrough curves at the exit of the block for the same head gradient but different side conditions (no flow or allowing side flow). We consider the 1200 fractures model and a Dirac input

Source	$T_{5\%}(y)$	$T_{50\%}(y)$	$T_{95\%}(y)$
Iodine Dirac	36	470	68000
Calcium Dirac	430	6900	$1.0\ 10^6$
Cesium Dirac	$2.2\ 10^5$	$4.0\ 10^6$	$4.8\ 10^8$
Radium Dirac	96000.	$1.5\ 10^6$	$2.2\ 10^8$
Technetium Dirac	$6.1\ 10^5$	$9.7\ 10^6$	$> 1.4\ 10^9$
Americium Dirac	$1.7\ 10^6$	$2.9\ 10^7$	$> 1.4\ 10^9$

Table 5.17: Other boundary conditions :breakthrough time history

Source	Maximal flux (1/y)	Time (y)
Iodine Dirac	$2.0\ 10^{-3}(1/y)$	63
Calcium Dirac	$1.5\ 10^{-4}(1/y)$	670
Cesium Dirac	$2.6\ 10^{-7}(1/y)$	$3.0\ 10^5$
Radium Dirac	$6.8\ 10^{-7}(1/y)$	$1.4\ 10^5$
Technetium Dirac	$1.0\ 10^{-7}(1/y)$	$8.6\ 10^5$
Americium Dirac	$3.6\ 10^{-8}(1/y)$	$2.3\ 10^6$

Table 5.18: New boundary conditions: maximum fluxes and peak arrival times for Dirac input.

So these modified boundary conditions lead to some change in the transfer properties although remaining of the same order. Detailed understanding of the travel paths and mixing at intersections with fracture intersecting the boundaries would be necessary. This was not done here. A possible explanation for the discrepancies could be that inflow of water from the sides of the block leads to relative dilution of the transported plume as well as some changes in the distribution of the water fluxes in the network.

Considering the limited sensitivity to the boundary conditions, one may prefer the first hypothesis brought up previously: transfer is mainly limited to one major transport path due to the actual structure of the fracture network (its connectivity in particular).

We further study below the properties of the block for different uniform flows corresponding to the same head gradient and no flow on the sides of the domain but for flow along the Y and Z orientations and both directions.

Different flow directions

In the following our purpose is to improve the understanding of the flow in the fractured network considering different uniform flow conditions (no flow on the sides of the domain) with the same head gradient intensity but in various directions. The geometry we work with is our 1200 fracture system.

The block is first characterized in terms of flow properties. We test the block with uniform gradients along two opposite sides of the block and no flow boundary conditions

on the sides. This is done along the 3 main axes orthogonal to the sides (X, Y, Z vertical axis).

The values measured for the permeability of the total block result from the total flux transiting in the system and the head gradient. The values are represented in Table 5.19.

	Along X	**Along Y**	**Along Z**
Total flux (m^3/y)	5.97	3.68	28.1
	Along X	**Along Y**	**Along Z**
Total permeability (m/s)	$9.46\ 10^{-10}$	$5.8\ 10^{-10}$	$4.45\ 10^{-9}$

Table 5.19: Diagonal terms of the permeability tensor

Two series of figures provide the breakthrough curves for the different tests considered (uniform flow and no flow on the sides). We considered flow in both directions from the same release position as in the deliveries. We draw here again the breakthrough curves provided in the performance measures for sake of illustration. These systems include the 1200 fracture network as well as full matrix diffusion in the line of the selected model.

X-axis flow

We just reversed the flow in the transport simulation by changing the Darcy velocity V into $-V$. We present the maximum fluxes and fluxes time recoveries for the different tracers as well as former results involving the direct X flow.

Time recoveries

The 5, 50 and 95 % time recoveries for the flux are summed up in Tab. 5.20, for the 1200 fractures mesh.

Orientation	$T_{5\%}(y)$	$T_{50\%}(y)$	$T_{95\%}(y)$
Iodine X	26	260	42000
Iodine -X	28	324	54000
Calcium X	310	3840	$6.4\ 10^5$
Calcium -X	330	4700	$> 8.\ 10^5$
Cesium X	$1.4\ 10^5$	$2.1\ 10^6$	$> 1.6\ 10^8$
Cesium -X	$1.6\ 10^5$	$2.7\ 10^6$	$> 1.6\ 10^8$
Radium X	64000.	$8.6\ 10^5$	$1.4\ 10^8$
Radium -X	72000.	$1.0\ 10^6$	$> 1.6\ 10^8$
Technetium X	$4.0\ 10^5$	$5.5\ 10^6$	$> 4.8\ 10^8$
Technetium -X	$4.3\ 10^5$	$6.7\ 10^6$	$> 4.8\ 10^8$
Americium X	$1.1\ 10^6$	$1.4\ 10^7$	$> 4.8\ 10^8$
Americium -X	$1.3\ 10^6$	$1.9\ 10^7$	$> 4.8\ 10^8$

Table 5.20: X-axis flow (direct and reverse): breakthrough time history

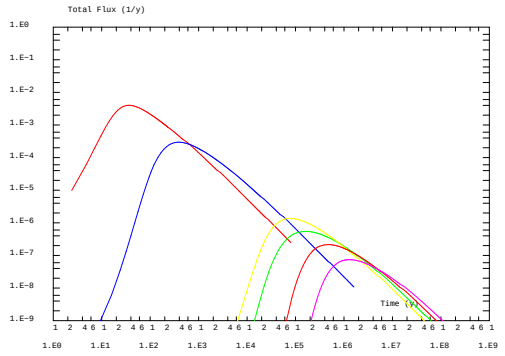

(a) Flow along X

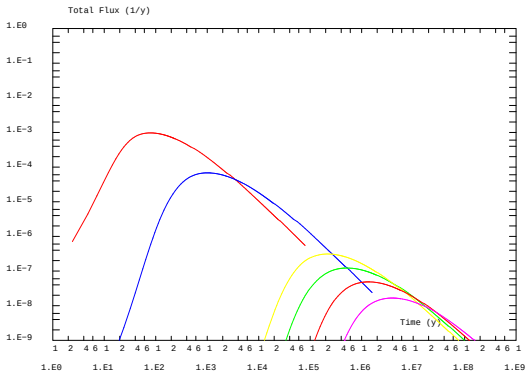

(b) Flow along Y

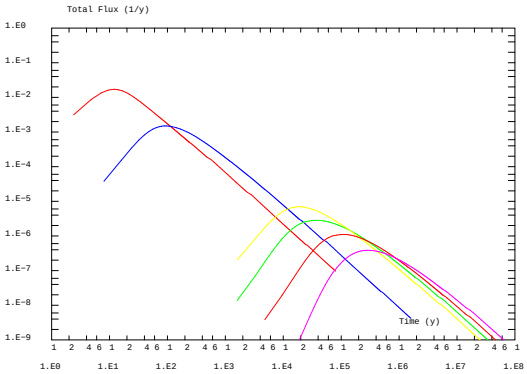

(c) Flow along Z

Figure 5.13: Breakthrough curves at the exit of the block for 3 different uniform flow directions (along X, Y and Z), 1200 fractures model, Dirac input

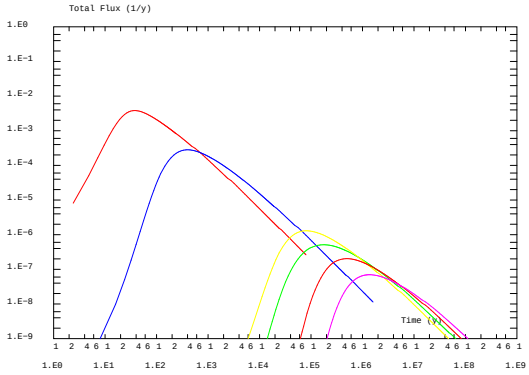

(a) Flow along -X

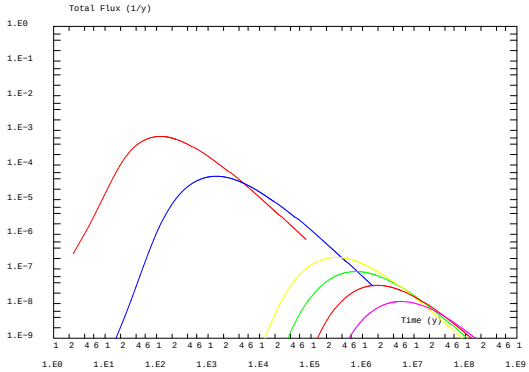

(b) Flow along -Y

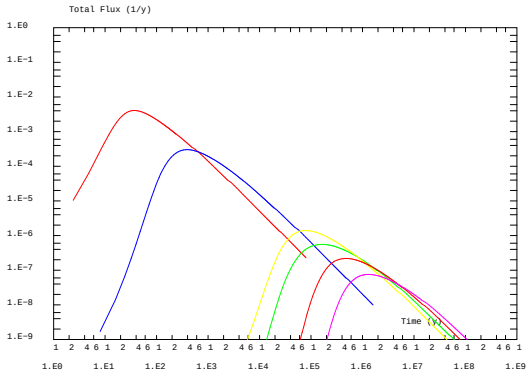

(c) Flow along -Z

Figure 5.14: Breakthrough curves at the exit of the block for 3 different uniform flow directions (along -X, -Y and -Z), 1200 fractures model, Dirac input

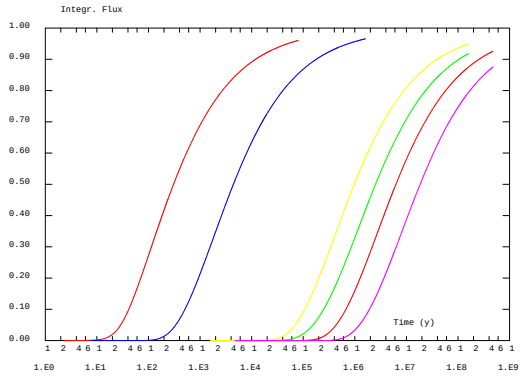

(a) Flow along X

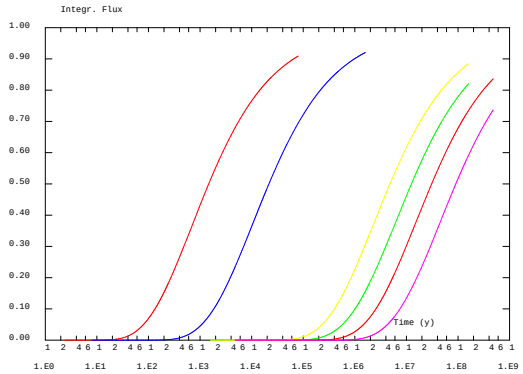

(b) Flow along Y

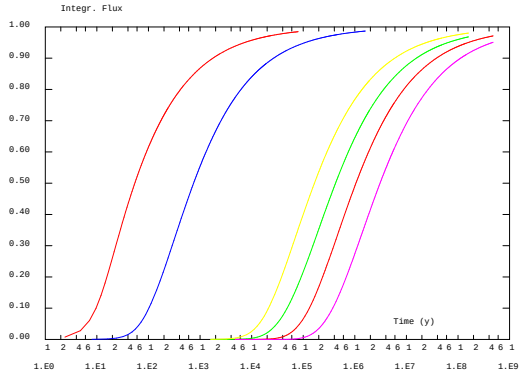

(c) Flow along Z

Figure 5.15: Cumulated flux at the exit of the block for 3 different uniform flow directions (along X, Y and Z), 1200 fractures model, Dirac input

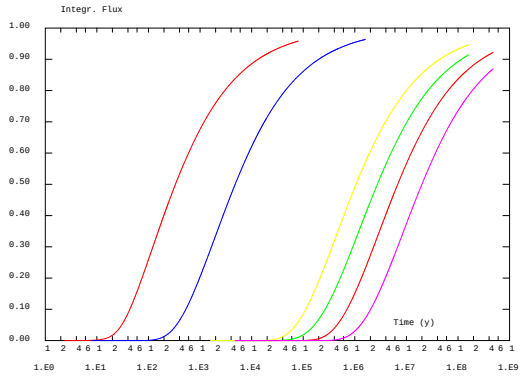

(a) Flow along -X

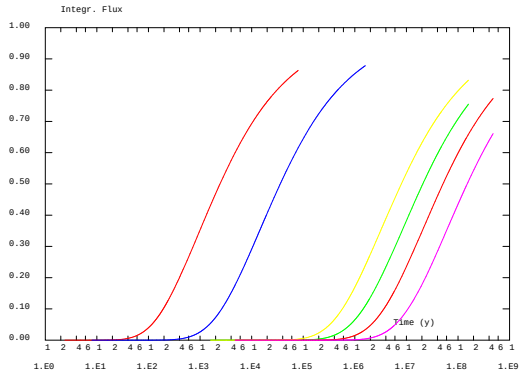

(b) Flow along -Y

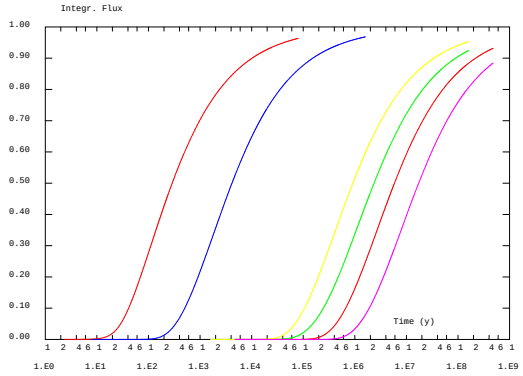

(c) Flow along -Z

Figure 5.16: Cumulated flux at the exit of the block for 3 different uniform flow directions (along -X, -Y and -Z), 1200 fractures model, Dirac input

Maximum fluxes

The maximum peak values for the flux are summed up in Tab. 5.21.

Direction	**Maximal flux (1/y)**	**Time (y)**
Iodine X	$4.\ 10^{-3}(1/y)$	35
Iodine -X	$3.8\ 10^{-3}(1/y)$	35
Calcium X	$3.2\ 10^{-4}(1/y)$	360
Calcium -X	$2.8\ 10^{-4}(1/y)$	387
Cesium X	$5.6\ 10^{-7}(1/y)$	$1.5\ 10^{5}$
Cesium -X	$5.1\ 10^{-7}(1/y)$	$1.7\ 10^{5}$
Radium X	$1.5\ 10^{-6}(1/y)$	76000
Radium -X	$1.3\ 10^{-6}(1/y)$	$0.77\ 10^{5}$
Technetium X	$2.3\ 10^{-7}(1/y)$	$4.4\ 10^{5}$
Technetium -X	$2.03\ 10^{-7}(1/y)$	$4.6\ 10^{5}$
Americium X	$8.1\ 10^{-8}(1/y)$	$1.2\ 10^{6}$
Americium -X	$7.0\ 10^{-8}(1/y)$	$1.3\ 10^{6}$

Table 5.21: Performance measures (direct and reverse): maximum fluxes for Dirac input.

Y-axis flow

We apply the head gradient along the Y-axis instead of the X-axis. Both directions are considered. Flow and transport for the same source location is simulated. We present the maximum fluxes and fluxes time recoveries for the different tracers.

Time recoveries

The 5, 50 and 95 % time recoveries for the flux are summed up in Tab. 5.22, for the 1200 fractures mesh.

Source	$T_{5\%}(y)$	$T_{50\%}(y)$	$T_{95\%}(y)$
Iodine Y	78	1400	> 80000
Iodine -Y	110	2400	> 80000
Calcium Y	1050	21000	$> 1.6\ 10^{6}$
Calcium -Y	1500	35000	$> 1.6\ 10^{6}$
Cesium Y	$5.5\ 10^{5}$	$1.2\ 10^{7}$	$> 1.6\ 10^{8}$
Cesium -Y	$8.2\ 10^{5}$	$2.\ 10^{7}$	$> 1.6\ 10^{8}$
Radium Y	$2.3\ 10^{5}$	$4.6\ 10^{6}$	$> 1.6\ 10^{8}$
Radium -Y	$2.1\ 10^{5}$	$7.2\ 10^{6}$	$> 1.6\ 10^{8}$
Technetium Y	$1.4\ 10^{6}$	$2.8\ 10^{7}$	$> 4.8\ 10^{8}$
Technetium -Y	$2.0\ 10^{6}$	$5.0\ 10^{7}$	$> 4.8\ 10^{8}$
Americium Y	$4.2\ 10^{6}$	$8.9\ 10^{7}$	$> 4.8\ 10^{8}$
Americium -Y	$5.7\ 10^{6}$	$1.4\ 10^{7}$	$> 4.8\ 10^{8}$

Table 5.22: Y-axis flow (direct and reverse): breakthrough time history

Maximum fluxes

The maximum peak values for the flux are summed up in Tab. 5.23.

Source	Maximal flux (1/y)	Time (y)
Iodine Y	$9.7\ 10^{-4}(1/y)$	78
Iodine -Y	$6.7\ 10^{-4}(1/y)$	110
Calcium Y	$6.8\ 10^{-5}(1/y)$	970
Calcium -Y	$4.7\ 10^{-5}(1/y)$	1350
Cesium Y	$1.2\ 10^{-7}(1/y)$	$2.2\ 10^{5}$
Cesium -Y	$8.4\ 10^{-8}(1/y)$	$8.\ 10^{5}$
Radium Y	$3.1\ 10^{-7}(1/y)$	$0.77\ 10^{5}$
Radium -Y	$2.1\ 10^{-7}(1/y)$	$3.2\ 10^{5}$
Technetium Y	$4.8\ 10^{-8}(1/y)$	$1.3\ 10^{6}$
Technetium -Y	$3.3\ 10^{-8}(1/y)$	$1.9\ 10^{6}$
Americium Y	$1.6\ 10^{-8}(1/y)$	$3.8\ 10^{6}$
Americium -Y	$1.1\ 10^{-8}(1/y)$	$5.7\ 10^{6}$

Table 5.23: Performance measures (direct and reverse): maximum fluxes for Dirac input.

Z-axis flow

We apply the head gradient along the Z-axis. Both directions are considered. We present the maximum fluxes and fluxes time recoveries for the different tracers. We aim here at studying block transfer properties, vertical flow has at sp no reality.

Time recoveries

The 5, 50 and 95 % time recoveries for the flux are summed up in Tab. 5.24, for the 1200 fractures mesh.

Source	$T_{5\%}(y)$	$T_{50\%}(y)$	$T_{95\%}(y)$
Iodine Z	4.8	52	7200
Iodine -Z	29	290	42000
Calcium Z	64	740	$1.0\ 10^{5}$
Calcium -Z	330	4100	$6\ 10^{5}$
Cesium Z	$2.8\ 10^{4}$	$4.2\ 10^{5}$	$6.\ 10^{7}$
Cesium -Z	$1.4\ 10^{5}$	$2.2\ 10^{6}$	$> 1.6\ 10^{8}$
Radium Z	$1.2\ 10^{4}$	$1.6\ 10^{5}$	$2.4\ 10^{7}$
Radium -Z	$6.8\ 10^{4}$	$9.1\ 10^{5}$	$1.4\ 10^{8}$
Technetium Z	$8.4\ 10^{4}$	$1.0\ 10^{6}$	$1.5\ 10^{8}$
Technetium -Z	$4.0\ 10^{5}$	$5.7\ 10^{6}$	$> 4.8\ 10^{8}$
Americium Z	$2.4\ 10^{5}$	$3.0\ 10^{6}$	$4.5\ 10^{8}$
Americium -Z	$1.2\ 10^{6}$	$1.7\ 10^{7}$	$> 4.8\ 10^{8}$

Table 5.24: Z-axis flow (direct and reverse): breakthrough time history

Maximum fluxes

The maximum peak values for the flux are summed up in Tab. 5.25.

Source	Maximal flux (1/y)	Time (y)
Iodine Z	$1.7\ 10^{-2}(1/y)$	12
Iodine -Z	$4.1\ 10^{-3}(1/y)$	37
Calcium Z	$1.4\ 10^{-3}(1/y)$	95
Calcium -Z	$3.\ 10^{-4}(1/y)$	370
Cesium Z	$2.8\ 10^{-6}(1/y)$	$3.7\ 10^{4}$
Cesium -Z	$5.5\ 10^{-7}(1/y)$	$1.6\ 10^{5}$
Radium Z	$6.9\ 10^{-6}(1/y)$	$1.8\ 10^{4}$
Radium -Z	$1.4\ 10^{-6}(1/y)$	$7.8\ 10^{4}$
Technetium Z	$1.1\ 10^{-6}(1/y)$	$1.1\ 10^{5}$
Technetium -Z	$2.2\ 10^{-7}(1/y)$	$4.7\ 10^{5}$
Americium Z	$3.8\ 10^{-7}(1/y)$	$2.9\ 10^{5}$
Americium -Z	$7.5\ 10^{-8}(1/y)$	$1.2\ 10^{6}$

Table 5.25: Performance measures (direct and reverse): maximum fluxes for Dirac input.

Results

Results show that the studied block presents properties depending on the direction of the uniform flow considered. Indeed, flow properties depend on the connectivity of the input and the output face. Transport in this system from the source located roughly in the middle of the cube leads to exploration of the plume of different portions of the block, ie the fracturation ramification located downstream. Results show that uniform flow within the horizontal plane lead to variable properties though of the same order of magnitude. Transfers in the vertical direction are easier and lead to rapid transfers. This is certainly due to the geometrical structure of the system with major extended subvertical fractures. Transfers in the horizontal direction differ nevertheless when it comes to the transport times. Transport along X direction is in this block roughly twice slower than along Y direction. The reasons for such results should be researched in the local structure of the fracture network along these directions. Direct and reverted flow were considered here since for both cases, flow properties in absolute values are identical, the direction of flow selecting the opposite part of the block for transport. So, in case one major flow line exists, transport in the opposite direction should remain on the same flow path, just would differ in exploring the local transport properties. For the X direction, breakthrough curves are almost identical. Reasons for such a result were not further researched. For the Y directions, results are similar though differing. Results show that there exist indeed a variability of transport properties within the block that explains the discrepancies in transport properties in all the considered directions. By the way, the direction selected in the deliveries leads to the shortest transit times within the horizontal direction.

Closer study of the structure of the flow and spatial repartition of the transport features would be required to understand at depth such results. It should be done in the line

followed previously for the actual conditions required in the deliveries. This was not done here due to a lack of time.

5.3 Discussion and conclusions

5.3.1 Discussion of results

We have studied a 200x200x200 meter cubic bloc of granite containing initially roughly 5600 fractures of more than 2 meters of extension. Sensitivity tests have been carried out:

- Sensitivity to the amount of fractures involved.
- Sensitivity to dispersivity.
- Sensitivity to representation of fracture complexity.
- Sensitivity to representation of matrix diffusion and impact of various sub units.

A reference model including 1200 fractures was selected to provide performance assessment measurements. All features like complexity and matrix diffusion could be correctly included in the model.

We also have built up and assessed a simplified PA model, involving 12 major fractures for flow and transport. This model proves comparable to the 1200 fracture system in terms of performance measures (within 10%). Reasons mainly rely in the low connectivity of the fracture network as developed below.

Results show that the different components of the system can be organized in first order and second order phenomena. The major features of the system correspond to the following items:

- From the 5600 fractures, only a surprisingly small amount actually contributes dominantly to water and tracer transfers. These principal fractures include main conductors as well as smaller fractures along the main travel paths. Although performance measures are based on a 1200 fracture system, we show that a well chosen 12 fracture system provides good performance measures as well.
- Matrix diffusion plays a dominant role in the transport as a retardation effect. The overall retardation measured in terms of peak arrival time ranges from roughly 10 (Iodine) to $4.\,10^5$ (Americium) and reduction of peak level from factor of 60 (Iodine) to a factor of $3.\,10^6$ (Americium). The impact of deeper matrix zones (altered and non altered rock) is dominant in the retardation of the breakthrough curves as measured on peak arrival times and levels as well as in terms of large tailing effects. For instance, due to these deeper zones, arrival time of 95% of the mass is delayed by factors ranging from $4.\,10^3$ (Iodine) to $4.\,10^7$ (Americium).

- The issue of complexity of fractured zones was studied. Simulations based on pure Type 1 versus pure Type 2 lead to significant differences showing that identification of these patterns are important. These effects are nevertheless less important than former points. In addition, for even slower flow conditions, penetration depth for matrix diffusion increases so that the impact of local matrix heterogeneity patterns (close to the flow path, for instance with mylonite) becomes minor.

Second order effects enclose:

- Dispersion effects in the fractures (modeling heterogeneity of flow patterns) as compared with dispersion related with the different paths along the fracture network.
- Some models for matrix diffusion proved to lead to similar results. This was the case for pure Type 1 versus dominant type because main conductors are dominantly of Type 1. It is similarly hard to discriminate between the composite approach for more in depth matrix zones (altered 20 cm + infinite non altered) and (infinite non altered) because the penetration depth is of the order of several meters making the 20 cm contribution of an altered zone in its properties of secondary importance as compared with non altered properties.
- The impact of back ground fracturing proved second order effect. Based on our studies the presence of these smaller features does not significantly modify the breakthrough curves corresponding to mass flux exiting the system.

There is nevertheless room for further studies. In particular, some efforts were put in trying to understand the reasons for obtaining good restitution of breakthrough curves based on a single transport path for a very reduced amount of fractures (12 units). Sensitivity of the properties of the block to different boundary conditions as well as analysis of the connectivity of the complex block leads to preliminary results showing that the geometrical features play a dominant role in this regard. For the present block, additional minor fracture does not lead to increased connectivity of the fracture network. No flow boundary conditions amplify this fact but are not the main contributor to this result.

5.3.2 Main conclusions

The most important conclusion is that modeling transfers in such a fractured block at PA time scale requires a sound understanding and modeling of some major fractures responsible for the dominant part of flow and transport properties. In addition to modeling of flow and transport in this system, matrix diffusion effects (as well as sorption effects) should be included with great care due to their major role in retarding the transfer of tracers.

As a consequence, more efforts could be put in characterizing the complexity of these main fractures (heterogeneous conductors) and modeling them taking the associated uncertainties into account. The actual influence of minor fractures on transfers appeared low

due to the connectivity structure of the system considered but could prove important for other test cases and require further studies. Based on studies conducted elsewhere (partially reported in chapter 7) relying on more connected fracture networks, the impact of back ground fracturing leads to increased access to matrix blocks enhancing retardation of the plume. The retardation can nevertheless show as global retardation of the plume without major tailing effect since the size of small scale blocks is small leading to shorter diffusive transit times in such smaller units. On the contrary systems at the percolation threshold would emphasize the results obtained in the present study since a very limited amount of travel path for water exist throughout the system. A source term well located aside from such travel paths would not lead to quick transfer times (in contrast with the short water travel time by roughly 3 years for the source location selected in the present study) since access to the water travel paths would require diffusion processes in the bulk of the rock. The implications of the particularity of the Task6C studied block are developed at larger extent in the next session.

The requirements in terms of information on the block properties for a sound PA modeling of transfers showed that information contained in tracer tests (conducted at maximum monthly to yearly scale) is poorly constraining. Along the lines of former conclusions bounded with the Task6C block, one should put a priority on a better characterization of the complexity of main conductors. These are here mainly responsible for the transfer properties of the 12 fracture travel path. In addition to these properties, local fracturing around the source term has as well a major impact on the results and should be documented. Associated best representation and modeling approaches should be listed. However, if the next block to be studied involves more connected fracturation, a good characterization of block sizes and their impact on the transfer would be required. In all cases a sound understanding of the flow properties of the system is required relying on a good knowledge and representation of the connectivity of the system. This is a crucial step but of course hard to obtained from mapping of fractures, geophysical studies and connectivity studies based on series of pumping tests.

This result (simplification to 12 major units) is rather surprising but can be explained based on considerations involving mainly connectivity of the fractures and position or extension of the initial conditions (the type of boundary conditions considered proved of minor importance). Another surprising result is that transit times in the block are of roughly 3 years, which is a rather short time as compared with what would be possibly expected from an actual storage situation. The question arising is how representative is the case studied as compared the objective of characterization of properties for the near field for a block where a storage is installed. This encloses representativity of the structural model as well. Another way of questioning the line of attack for the present task involves the following points: (i) are the results sensitive to the location of the source or the extension of the source, (ii) how much do the results dependent on the geometrical patterns of the system.

5.3.3 Lessons learned and implications for Task6 objectives

The fractured block studied is a complex system involving several spatial scale as well as temporal scales. Modeling such a system with sufficient precision and obtaining reliable results is in itself a challenging task. An even more challenging task goes further than representation and modeling issues and acquisition of breakthrough curves. It consists in understanding the results obtained from the code and the implication of the possible hypothesis. The main part of our efforts was indeed put in assessing the impact of various parts of the system to block transfer properties. In particular, understanding the two main results in terms of radical simplification of the total fracture network and assessing the impact of various matrix zones required longer studies than simply running the model on the cases required in the deliveries. The lesson learned is that such an effort is valuable in terms of results but is time consuming.

Another point is that working on the 5600 fracture system resulting from Task 6C was here a good incentive to obtain some general results on a realistic system. Nevertheless, some of the conclusions remain bounded to the system studied and would not apply to other systems. For instance, the possibility of an extreme simplification of the system to 12 major features is apparently linked to the structure of connectivity of this particular fracture network.

This leads to implications for general objectives of assessing transfers at PA time scale in a realistic 200 m block. The present situation within the task is favorable to consider the implications of various competing modeling approaches and their consequences in terms of mass flux exiting the system. More general considerations on the properties of some generic fracture block would require studying other geometries as the present realization (which is only representative for itself). This would not be particularly difficult due to the modeling capacities developed at the present stage. A refined understanding of the role of smaller scale heterogeneity could be included along the line of complexity of main conductors or back ground fracturing depending on the connectivity of these units.

Another point corresponds to the pertinence or representativity of the present test case as compared with the situation expected in the 200 m vicinity of a repository installed in a fractured block. In addition to former remarks about the particularity of the geometry considered and the need for other cases, a refined study of the boundary conditions to be imposed is necessary in our view in the line started in the present study. One may refer to the very short travel time of water in the simulated situation (roughly 3 years) and enhanced travel times when considering for instance horizontal flow but along perpendicular direction (labeled Y direction in our study). But another major difference is certainly to be found in the size of the initial source. Indeed due to the volume of the storage, considering a spatial punctual source is certainly a strong hypothesis leading to possible selection of some main transport paths whereas a larger source would definitely integrate many more transport paths to the outlet of the block. The resulting transfer properties of the block would possibly lead to a more continuum representation of the system whereas the present one boils down to a major transport path.

Chapter 6

Task 6F

We present the results along the following sections. Section 6.1 provides the information from the specifications [*Elert et Selroos 04b*] including calculation cases, modeling strategy, and performance measurements. Section 6.2 provides the modeling strategy. Section 6.3 provides the results. Section 6.4 provides analysis of the results along the lines of understanding the role played by various matrix sub units, study of the impact of matrix diffusion of Type 1 versus Type 2, quantification of the delay introduced by the various cases, building of an equivalent representation of the system for different regimes.

6.1 Introduction

Simulations are conducted according to the specifications of the task [*Elert et Selroos 04b*].

Two fractures are extracted from the semi synthetic Task 6D block : Feature 1S with pure Type 1 matrix properties and Feature 4S with pure Type 2 matrix properties. Six cases are defined corresponding to 3 flow regimes (over 2 orders of magnitude changes in head gradient in the fracture). Travel times range from 0.1 year to 10 years (see a overview of the flow regimes considered on table 6.1). Uniform flow is considered in the fracture planes. The source term is a 3 m line in a 112 m long unit. The collection line is located 20 m down the flow. One may report to Figure 6.1. Three tracers are considered ranging from non sorbing to intermediate sorbing : I-129, Cs-137, Am-241.

Breakthrough time histories at the collection lines are simulated as well as other performance measures presented below.

6.2 Modeling strategy

We explicit our modeling strategy for the fracture flow and for matrix properties.

Travel time (yr)	Feature 1S, Type1	Feature 4S, Type 2
0.1	A1	A2
1.	B1	B2
10.	C1	C2

Table 6.1: Simulation cases considered

6.2.1 Fracture properties

Constant flow properties are considered in the fracture (see Figure 6.1). Due to lack of information about the heterogeneity of the fracture, no variation in Transmissivity is introduced within the fracture nor any variation in fracture flow or transport aperture. This is consistent with our approach in Task 6A, 6B, 6D and with the specifications [*Elert et Selroos 04b*].

As a consequence, for the boundary conditions considered, the flow in the fracture is uniform from upstream limit to downstream border. Transport in the fractures occurs by advection and dispersion. Sorption 'onto fracture walls' is included. In reality it corresponds to diffusion into the thin fracture coating zone and is equivalently represented by a fracture retardation coefficient term (see [*Dershowitz et al. 03*], Equation 2.2 Page 40).

Fracture properties are recalled in Table 6.2.

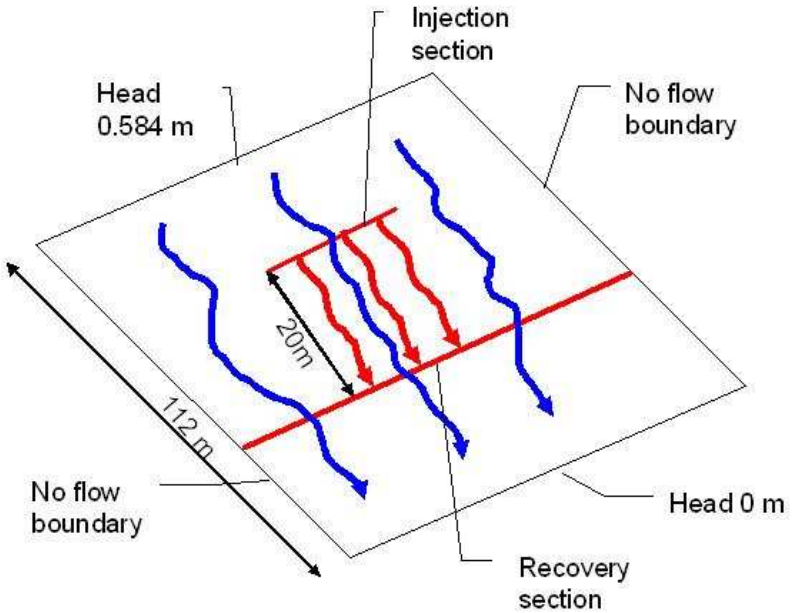

Figure 6.1: System geometry, boundary conditions, collection line

Structure Name	Geological type	Transmissivity (m^2/s)	Aperture (m)
1S	1	$3.14\ 10^{-7}$	$2.58\ 10^{-4}$
4S	2	$1.90\ 10^{-7}$	$2.02\ 10^{-4}$

Table 6.2: Properties of the selected features 1S and 4S (according to data deliveries)

6.2.2 Matrix properties

Two matrix types are involved (see Task6C report, [*Dershowitz et al. 03*]). These involve for Type 1 (fault), gouge, fracture coating, cataclasite, altered zones, non altered zones; for Type 2 (non fault feature), fracture coating, altered and non altered zones.
Lacking more precise information about repartition of these subunits, we model the Type 1 and 2 units deterministically and as provided in the deliveries [*Elert et Selroos 04b*] (see Figure 6.2-a and 6.2-b). This approach is coherent with our Models 1 and 2 from Task 6AB [*Grenier 03*] as well as Task6D approach [*Grenier 04*].

Matrix properties are recalled in Table 6.4. Matrix zones are modeled as no flow zones, accessed by pure diffusion processes from the fracture. Diffusion in these units is fully 3D. Sorption in the bulk is modeled.

As a consequence, flow is uniform in the fracture, matrix properties are identically distributed all over the fracture (only variating orthogonally in the matrix depth). We consider an infinite collection line (capturing the mass across the whole fracture, as required in [*Elert et Selroos 04b*]). For such homogeneous properties and collection conditions, the system is equivalently represented as a 1D fracture with punctual source and output location 200 m downstream. We consider pure Type 1 or Type 2 matrix properties as required.

The different cases considered are summed up on Table 6.1.

6.2.3 Numerical simulation

The simulation for flow and transport is conducted within our Cast3M code. The fracture and matrix zones are meshed. Simulation of flow and transport is conducted based on a mixed and hybrid finite element scheme. Transport calculation is Eulerian. The discretization of the different zones is conducted taking appropriate Courant as well as Fourier coefficients into account. This means that efforts are put into providing the best discretization strategy for each simulation. The penetration depth for the last zone considered in the depth of the matrix (non altered zone) is chosen so that this boundary condition (no flux) is far enough from the plume in order to minimize its influence. Practically speaking this is hard to maintain for all positions along the flow path. We made compromises between simulation costs and precision of the results. We nevertheless chose matrix depths sufficient to have very minor effects on the tailing of the breakthrough curves, at least up to the performance measure T95 (time of arrival of 95% of the injected mass).

Initial conditions are Dirac mass in the fracture element closer to 20 m distance to the downstream limit of the domain. The simulation domain extends 20% more than the 20 m required in order to prevent from the influence of upstream boundary conditions (zero concentration imposed). The rest of the domain is imposed zero diffusive flux. This condition is transparent at the output for breakthrough curves.

We measure breakthrough curves in terms of concentration at the outlet, output mass flux, evolution of masses in the various units of the system, concentration profiles across the system, concentration fields in the whole system at different simulation times.

Depths considered for simulation for non altered rock are provided below on table 6.3. Actual penetration depths are hard to determine because of the smooth shape of diffusion curves. One can probably consider that the half value as representative of the phenomenon. Anyway, results show that the penetration depth increases with slower flow regimes (large contact time) and decreases with increasingly sorbing tracers (lower apparent diffusion coefficient). Maximum penetration depth is lower than 10 meters. Actual penetration depth for sorbing tracers is more of the oder of 1 m. Diffusion into matrix zones as a conclusion involves metric zones of the rock around this kind of more transmissive unit. As a whole, at the scale of 200 m and for sorbing cases considered for most radio nuclides, transfers would remain dominantly local around such fractures if no additional back ground fracturing was to be considered.

Penetration depths (m)	A1	B1	C1	A2	B2	C2
Iodine	0.5	2.5	15.	0.3	1.	7.5
Cesium	0.01	0.75	3.	0.02	0.75	5.
Americium	0.01	0.5	2.	0.01	0.5	3.

Table 6.3: Penetration depths

The system modeled is illustrated for Feature 1S (refer to figure 6.2). It is represented as a fracture volume surrounded all along by matrix zones (Gouge, Cataclasite, altered and non altered zones) (Fig. figure 6.2(a)). Fracture coating zone is not meshed but its presence is included by means of an equivalent retardation coefficient. An example of the mesh is reproduced on Figure 6.3(a) (vertical dimension amplified) showing that all previous units are discretized. An example of concentration field is provided on figure 6.3(b). The fracture is roughly vertically in the middle of the modeled zone. The initial source is located 20 m from the outlet (left of the domain). The domain is 20% larger upstream to impose zero concentration at a sufficient distance. Output fluxes are collected at the outlet (no diffusive flux boundary condition as for all other sides of the domain). Flow velocity is uniform in the fracture and negligible in the matrix zones. An example of the evolution of the concentration profile across the system is provided on figure 6.3(c): concentration moves from fracture to surrounding matrix zones penetrating deeper and smoothing down when time goes on. The depth chosen in the simulations is sufficiently large to have negligible effect on the calculation.

Feature 4S is treated similarly. Only half of the system needs to be represented due

to symmetrical properties of Type 2 matrix zones. One should indeed recall that fracture coating is not meshed but represented equivalently in the fracture equation as a retardation factor.

Task6F	Fracture	Gouge	Cataclasite	Altered Rock	Non Alt. R.
Extent	$2.58\,10^{-4}m$(1S)	$5mm$	$2cm$	$20cm$	
Extent	$2.02\,10^{-4}m$(4S)	$5mm$	$2cm$	$20cm$	
Porosity	1	20%	1%	0.6%	0.3%
Pore diffusion coef. (m^2/s)	10^{-9}	6.10^{-10}	10^{-10}	$7.8\,10^{-11}$	$5.3\,10^{-11}$
Effective diffusion coef. (m^2/s)	10^{-9}	10^{-10}	10^{-12}	5.10^{-13}	$1.5\,10^{-13}$
Iodine $K_a(m)$, $K_d(m^3/kg)$	Fr. Coat.	0.	0.	0.	0.
Iodine R_a or R_d	1.10(1S)	1.	1.	1.	1.
Iodine R_a or R_d	1.12(4S)	1.	1.	1.	1.
Cesium $K_a(m)$, $K_d(m^3/kg)$	Fr. Coat.	$1.6\,10-1$	$1.5\,10^{-2}$	$2.0\,10^{-2}$	$1.0\,10^{-2}$
Cesium R_a or R_d	259.59(1S)	1729.0	4010.5	8947.0	8974.0
Cesium R_a or R_d	332.92(4S)	1729.0	4010.5	8947.0	8974.0
Americium $K_a(m)$, $K_d(m^3/kg)$	Fr. Coat.	0.5	0.5	0.5	0.5
Americium R_a or R_d	2486.6(1S)	5401.0	$1.34\,10^5$	$2.24\,10^5$	$4.49\,10^5$
Americium R_a or R_d	3191.4(4S)	5401.0	$1.34\,10^5$	$2.24\,10^5$	$4.49\,10^5$

Table 6.4: Parameter set for different matrix zones from the deliveries. Fracture sorption properties correspond to the presence of fracture coating (porosity by 5%, extent by $5mm$, $K_d = 5.2\,10^{-2}$ for Cesium and $K_d = 0.5$ for Americium).

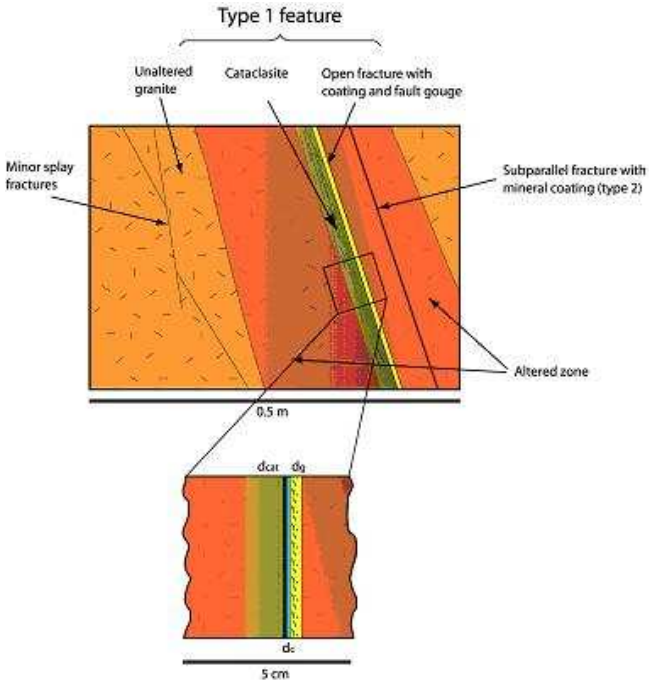

(a) Type 1 (fault) with fracture coating, gouge, cataclasite, altered and non altered rock)

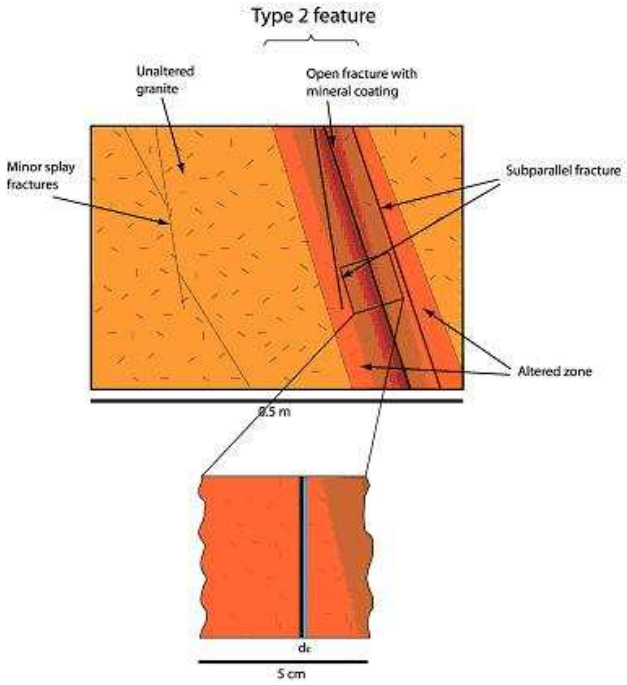

(b) Type 2 (non fault) with fracture coating, altered and non altered rock

Figure 6.2: Fracture types; Type 1 (fault) and Type 2 (non fault)

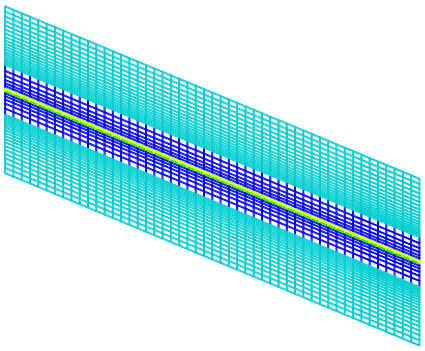

(a) Meshing of the system

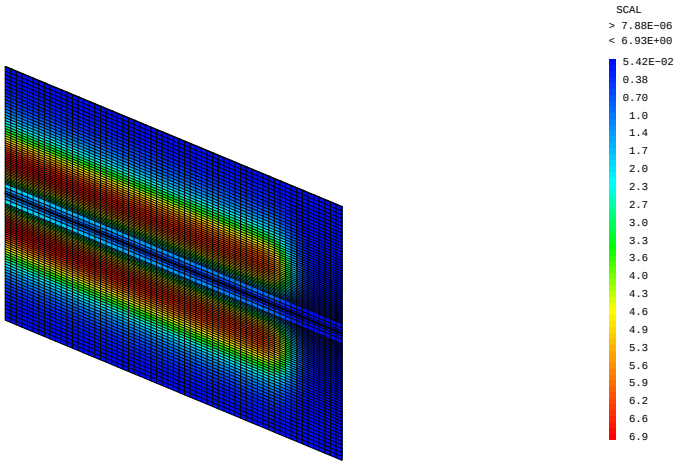

(b) Concentration fi eld

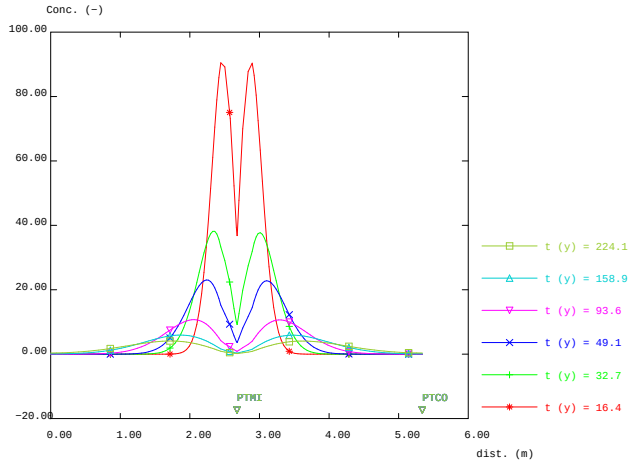

(c) Concentration profi le evolution across the system (vertical plane at mid distance (10 m))

Figure 6.3: Feature 1S, Type 1: illustration of the simulation approach. Results correspond to Iodine for Case B1

6.3 Results

Performance measures include :

- Breakthrough curves associated with each simulation case and for all 3 tracers (Iodine, Cesium, Americium). These are firstly jointly represented on figures 6.4 and 6.5 with a free scale. The same results are provided in the format required in the specifications on figures 6.6 to 6.11. The curve associated with each of the tracer, is identified through its color as follows:
  - Red for Iodine
  - Green for Cesium
  - Blue for Americium
- Peak arrival times and associated fluxes are provided on Table 6.5.
- Arrival times for 5%, 50% and 95% of the injected mass are provided on Table 6.6.

These results are discussed in next section 6.4.

Peak arrival	A1	B1	C1	A2	B2	C2
Iodine, Max. Fl., (1/y)	1.57	$7.95\,10^{-2}$	$2.80\,10^{-3}$	4.19	$8.84\,10^{-2}$	$2.75\,10^{-3}$
Iodine, Ass. Time (y)	0.56	7.17	161.39	0.14	2.70	131.55
Cesium, Max. Fl., (1/y)	$6.79\,10^{-4}$	$1.53\,10^{-5}$	$4.28\,10^{-7}$	$1.05\,10^{-3}$	$1.13\,10^{-5}$	$3.13\,10^{-7}$
Cesium, Ass. Time (y)	901.78	16975.	$8.59\,10^{5}$	169.79	12518.	$1.09\,10^{6}$
Americium, Max. Fl., (1/y)	$3.61\,10^{5}$	$6.45\,10^{-7}$	$1.29\,10^{-8}$	$4.33\,10^{-5}$	$4.53\,10^{-7}$	$8.86\,10^{-9}$
Americium, Ass. Time (y)	6097.5	$2.89\,10^{5}$	$2.01\,10^{7}$	3638.2	$3.06\,10^{5}$	$2.81\,10^{7}$

Table 6.5: Peak arrival time and associated maximum fluxes (Mass Dirac injection)

Times	A1	B1	C1	A2	B2	C2
Iodine, T5 (y)	0.36	4.82	80.69	9.11E-02	1.97	79.27
Iodine, T50 (y)	0.68	12.22	277.95	0.23	10.29	291.78
Iodine, T95 (y)	7.14	152.17	12967.	9.25	209.78	14829.
Cesium, T5 (y)	623.29	12466.	5.04E+05	114.86	9188.5	6.26E+05
Cesium, T50 (y)	1445.5	62329.	1.84E+06	923.84	79900.	2.52E+06
Cesium, T95 (y)	54770.	1.21E+06	3.86E+07	70933.	1.59E+06	8.99E+07
Americium, T5 (y)	3556.9	1.90E+05	1.25E+07	2585.1	2.27E+05	1.75E+07
Americium, T50 (y)	22866.	1.44E+06	6.60E+07	22500.	2.04E+06	9.48E+07
Americium, T95 (y)	1.39E+06	4.18E+07	1.13E+09	1.77E+06	5.25E+07	2.27E+09

Table 6.6: Times associated with arrival of 5%, 50% and 95% of the injected mass

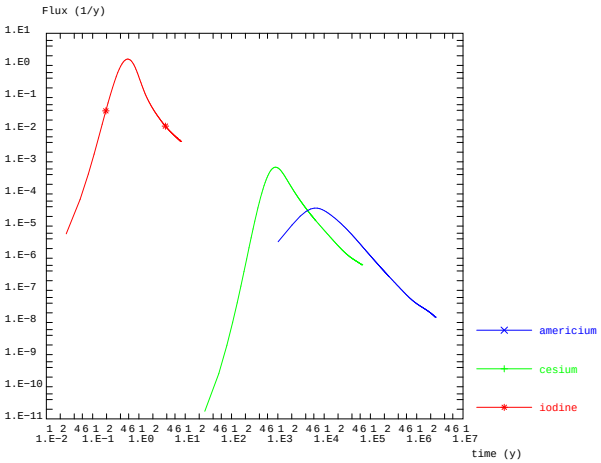

(a) Case A1

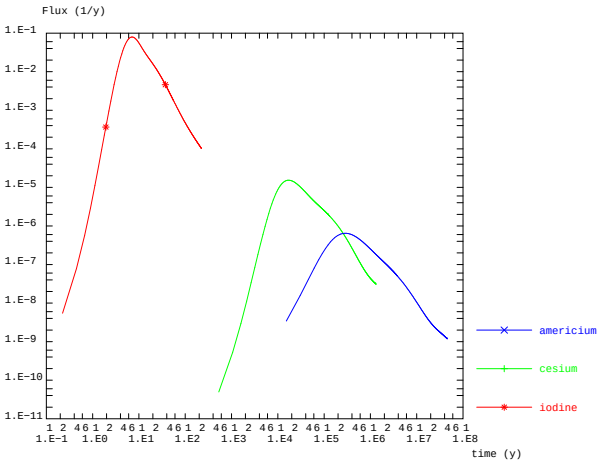

(b) Case B1

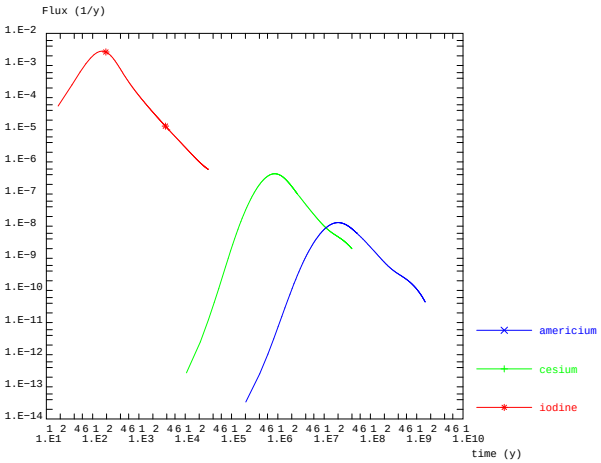

(c) Case C1

Figure 6.4: Feature 1S, Type1: BTC for Iodine, Cesium, Americium

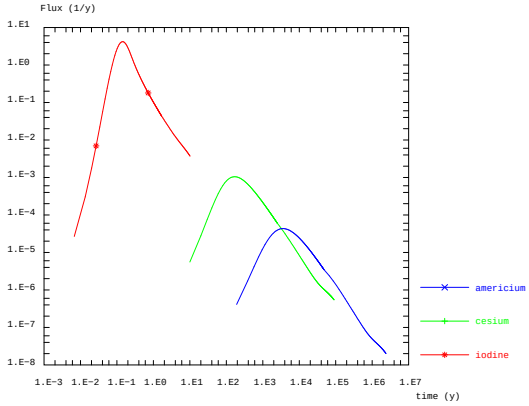

(a) Case A2

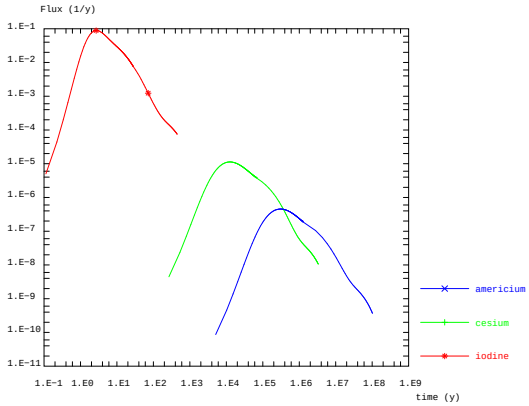

(b) Case B2

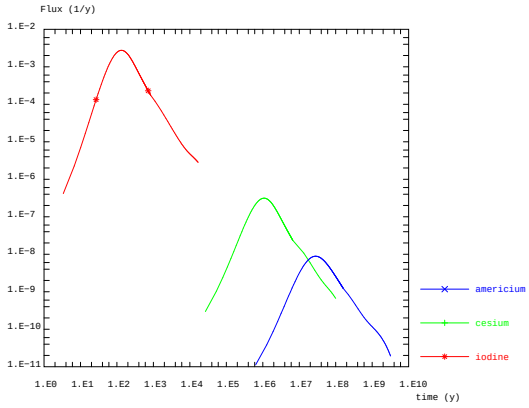

(c) Case C2

Figure 6.5: Feature 4S, Type2: BTC for Iodine, Cesium, Americium

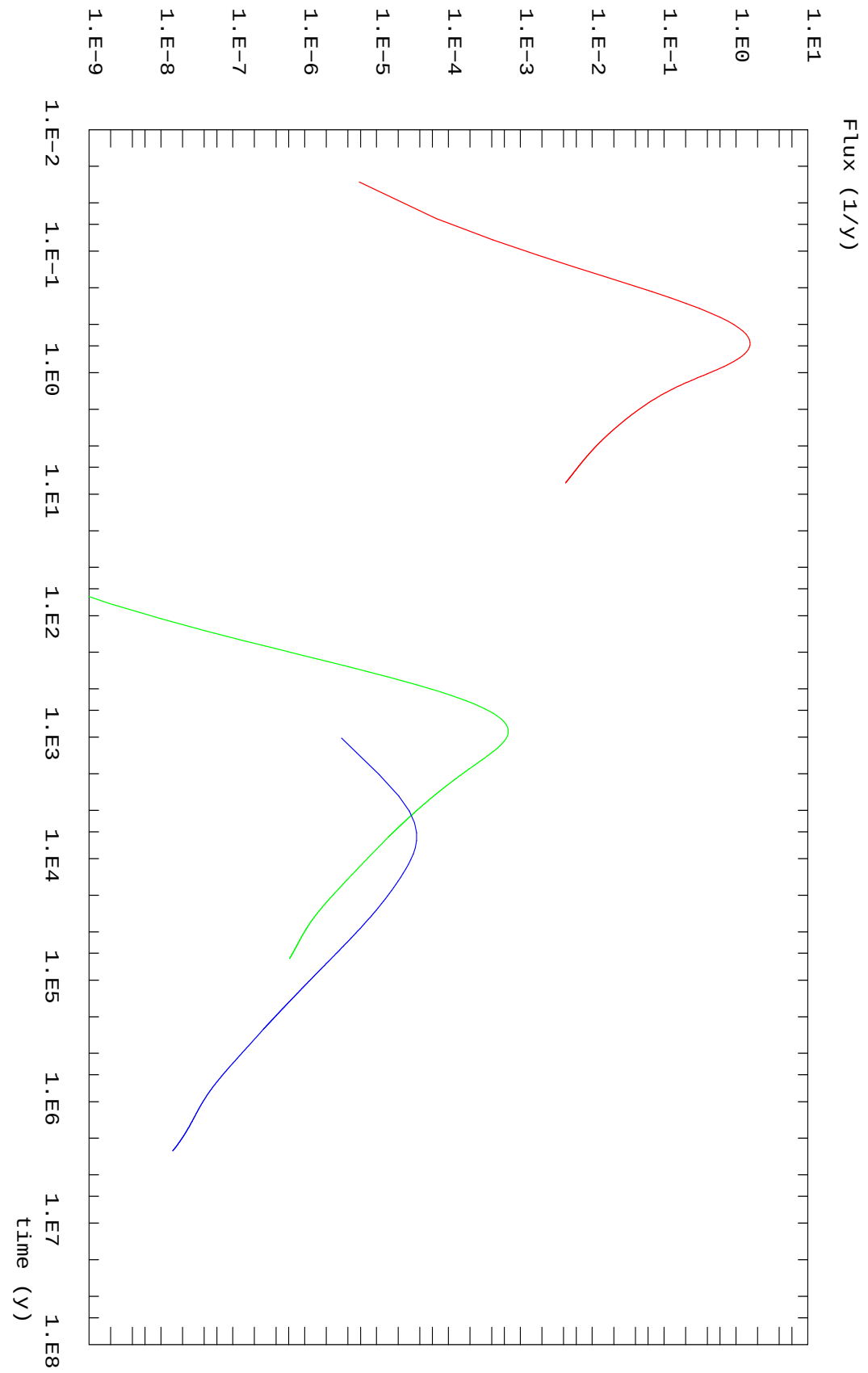

Figure 6.6: Case A1, Breakthrough curves for Iodine, Cesium and Americium for mass Dirac input

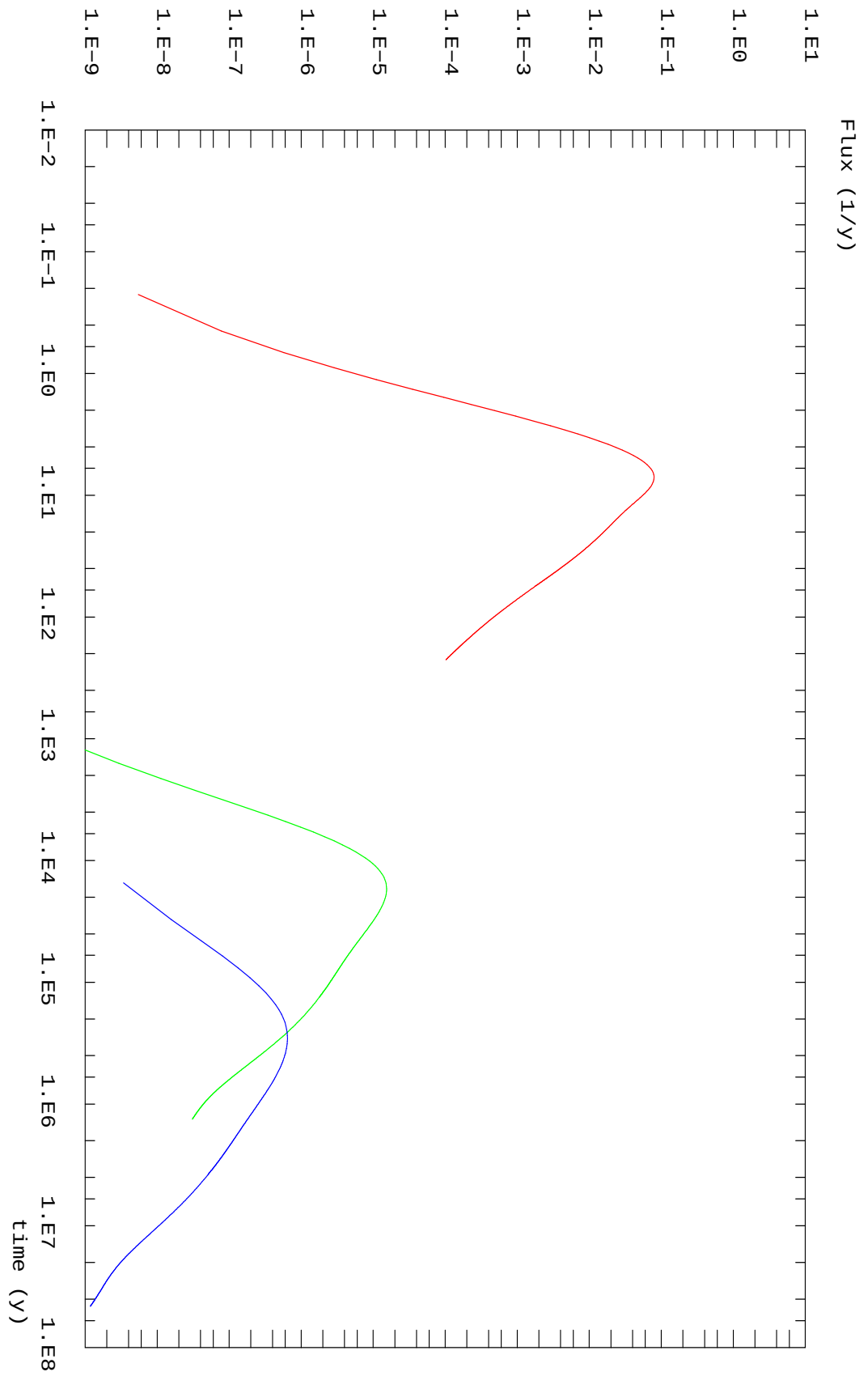

Figure 6.7: Case B1, Breakthrough curves for Iodine, Cesium and Americium for mass Dirac input

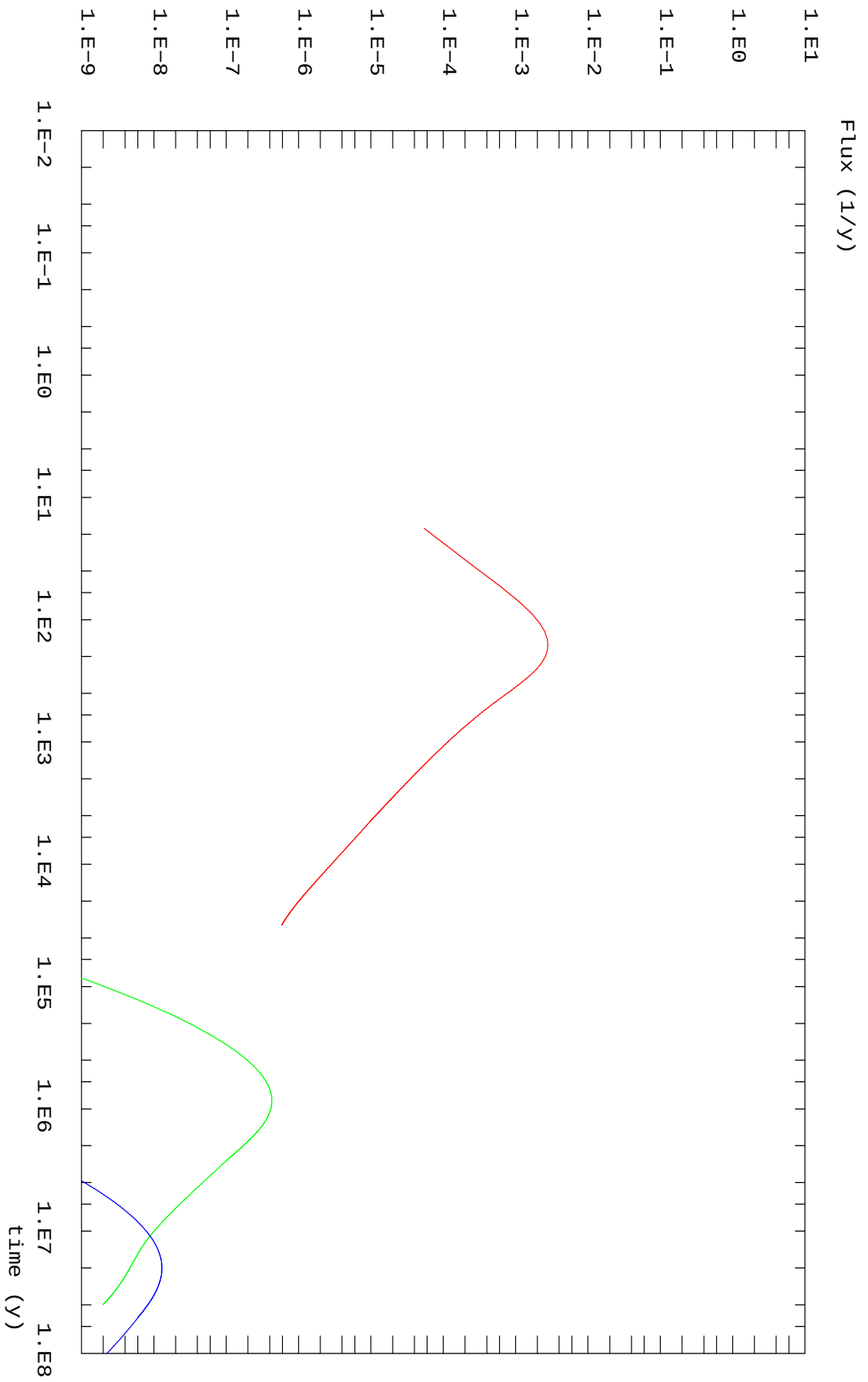

Figure 6.8: Case C1, Breakthrough curves for Iodine, Cesium and Americium for mass Dirac input

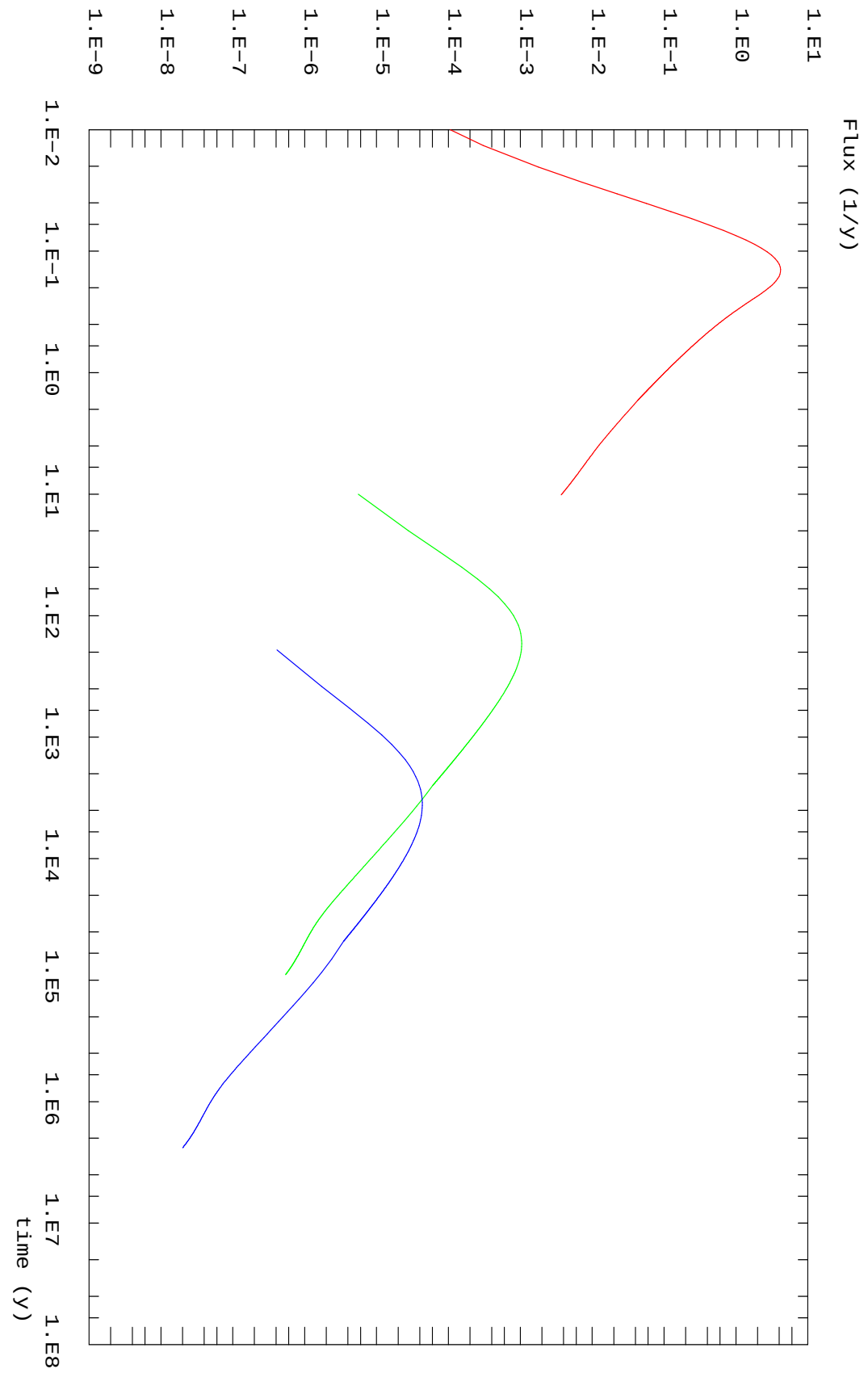

Figure 6.9: Case A2, Breakthrough curves for Iodine, Cesium and Americium for mass Dirac input

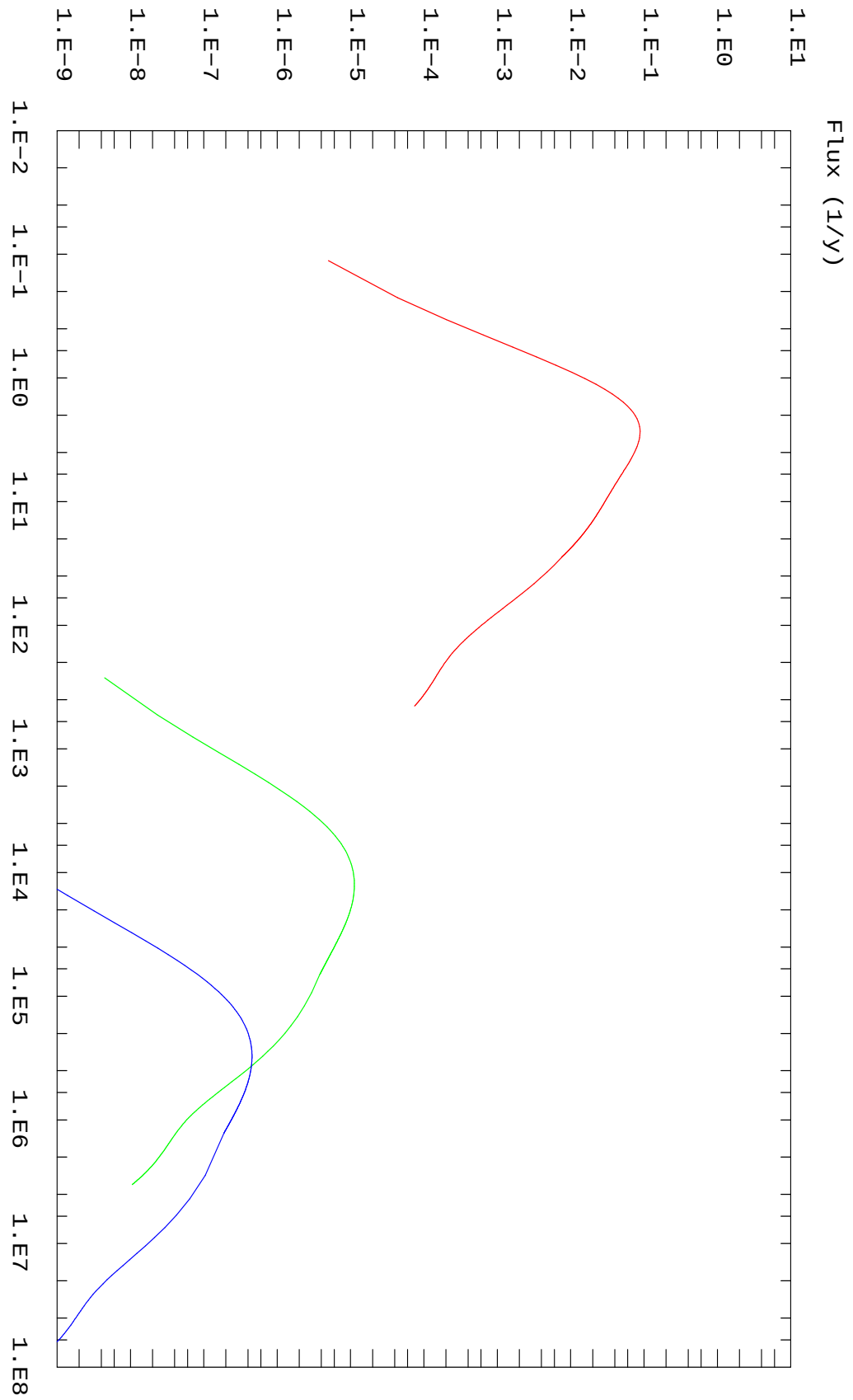

Figure 6.10: Case B2, Breakthrough curves for Iodine, Cesium and Americium for mass Dirac input

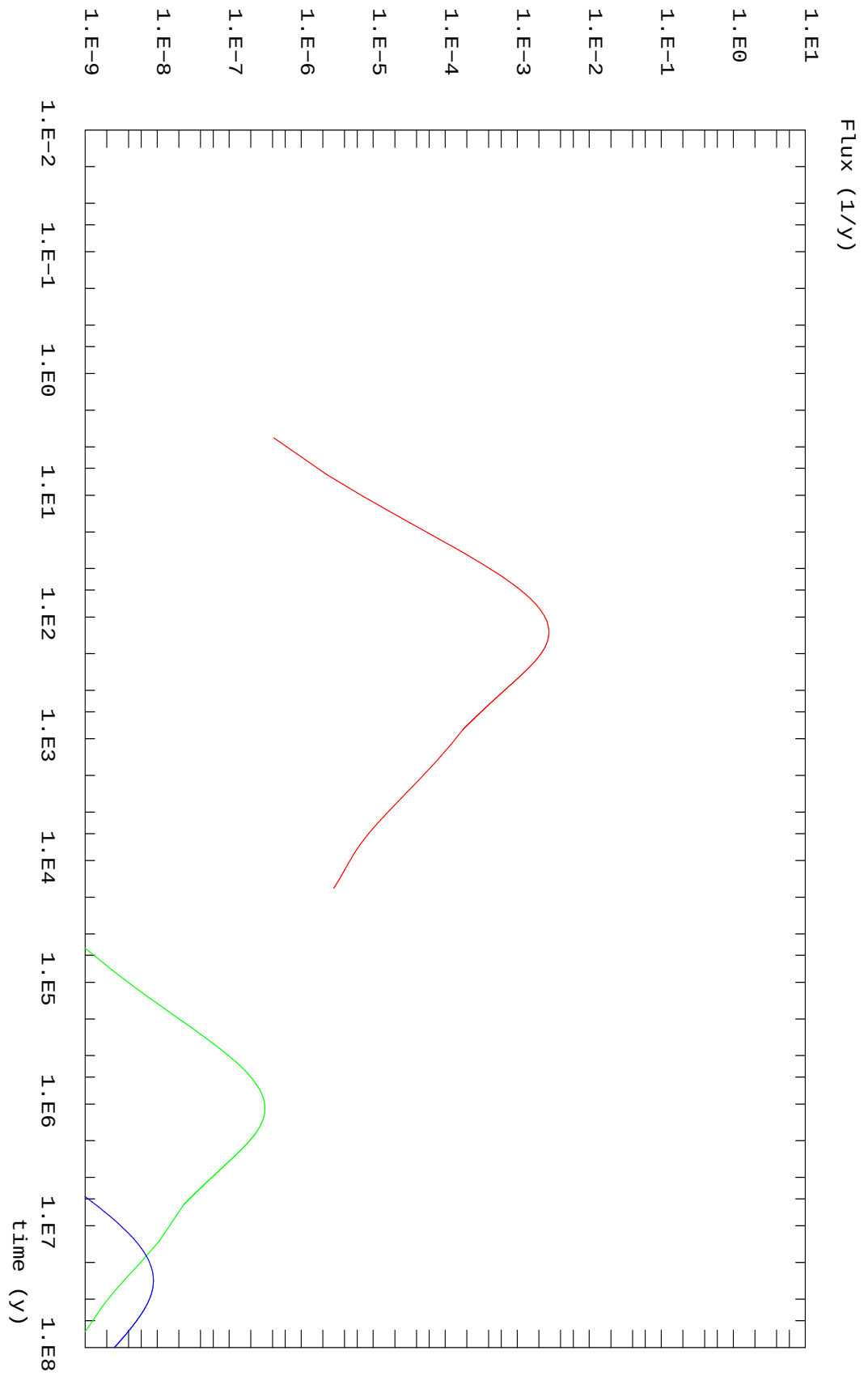

Figure 6.11: Case C2, Breakthrough curves for Iodine, Cesium and Americium for mass Dirac input

6.4 Analysis of the results

Former results showed classical results. First, when flow velocity is lowered, matrix diffusion is the main part of the system controlling the transfer time scales. This is visible in terms of peak arrival time as well as for the global shape of the curves. In particular, $T_{95}\%$ increases rapidly. Another expected results is that Type 1 matrix zones have a stronger retention impact as Type 2 matrix zones. This is indeed due to the presence of additional matrix zones like Gouge and Cataclasite that are associated with large porosities and diffusion coefficients. Another trend which is not to be surprising is that when moving to more strongly sorbing tracers, breakthrough curves are very efficiently delayed.

Nevertheless, some other features observed deserve some comments and explanations whereas more in depth analysis of the results allow for better understanding of the regimes of the system. So, we add here a few comments and analysis on the former results. These are developed along the following lines:

1. In section 6.4.1, we study of the role played by the different matrix zones in the retention process. We analyze their impact for the different flow regimes considered as well as the possibility to simplify their geometry for PA purposes in the line of former studies [*Grenier 03*].

2. In section 6.4.2, we analyze the influence of considering pure Type 1 or pure Type 2 matrix conditions for Feature 1S. This analysis provides explanations for the performance measurements obtained previously on both systems based on Feature 1S for pure Type 1 and Feature 4S for pure Type 2. In particular one can observe that when moving to slow flow cases as well as strong sorbing cases, breakthrough curves associated with Type 1 case (ie Case C1) and Type 2 case (ie Case C2) seem to merge. This is studied here with the introduction of a new series of simulations A3 to C3 considering Feature 1S properties for pure Type 1 matrix.

3. In section 6.4.3, we confront the results obtained in terms of peak arrival times with estimations based on analytical expressions derived from simplified systems.

6.4.1 Contributions to the transfer for the various matrix zones

We take here opportunity of the previous simulations to increase the level of understanding of the effects of the heterogeneity of matrix properties on the retention of a plume.

We plot in the following the evolution of masses in the various matrix sub units of the system. This helps in understanding (i) the role played by the different matrix sub units to the retention process and (ii) the way the system can be simplified for PA purposes.

Evolution of masses for cases A1, B1, C1 (pure Type 1, Feature 1S)

We provide below with plots of the evolution of masses in the different sub units of the matrix for all cases and tracers considered. One should recall that water arrival times for Cases A1, B1, C1 are respectively 0.1, 1. and 10. years. Mass initially introduced in the system is 1. (Mass Dirac).

We refer in the following to figures 6.13, 6.14 and 6.15 providing the evolution of masses in the different matrix sub units for all tracers and cases. On these figures, altered and non altered zones are presented twice since two distinct zones of each type are present above and below the fracture. We include a mention of peak arrival times for each case in the figure caption (one may refer as well to table 6.5). We propose here some comments:

- Considering the curve associated with total matrix mass (green solid line), figures show that the system is most controlled by the matrix as the flow is slow. This is due to the fact that diffusion processes have more time to develop. This leads to large control of the transfer regimes by large diffusive time scales.

- Comparing the difference between peak arrival times (see captions) and advective travel times (0.1, 1., 10. years respectively for A1, B1, C1): the discrepancy increases when moving to slow flows. This confirms the former remark knowing that matrix diffusion acts as a retention process. Moreover, considering the shapes of the curves, matrix diffusion leads to delays in the peak arrival times as well as larger tailing of the curves, that is classical change in the shape of the curve.

- Figure 6.12 provides the evolution of masses in fracture, cumulated in all matrix zones and total mass. This result corresponds to Case B1 for Iodine. We see here the classical features associated with matrix diffusion: mass in the fracture is rapidly transfered (blue curve quickly decreasing) whereas mass in the matrix increases and later slowly decreases (red line) providing long tailing in the breakthrough curves at the outlet. After less than 10 years, mass present in the system is almost exclusively to be found in the matrix (compare green line representing total mass and the red line). The shape of the curves is typical and is to be found in other cases.
  Indeed for Cases A1, B1, C1, some sub units provide similar behaviors as the previous fracture curve whereas others have typical matrix mass evolutions corresponding to intermediate storage. We comment the curves associated more in details in the following (refer to figures 6.13, 6.14 and 6.15). Evolution of masses is represented for each sub unit modeled: Gouge, Cataclasite, altered and non altered units. The latter are described by two curves because we modeled two units of each according to the representation on Figure 6.2(a).

  – For Case A1 (Fig. 6.13), mass remains in the vicinity of the fracture. The amount of mass is negligible in non altered zones, it is mainly located in Gouge and to lesser extent in Cataclasite and non altered zones. The curve for Gouge provides patterns typical of fracture behavior as described formerly:

rapid vanishing without storage. This means that this zones acts as a buffer immediately filled up by the mass present in the fracture. This was observed and explained previously in [*Grenier 03*]. We stated as well that this system can be equivalently represented by including this type of zone (here Gouge only, that is for Equation 6.1, $N = 1$ and Gouge properties) as equivalent fracture property by means of retention coefficient R' (N number of zones following this regime, e fracture aperture, ϵ_i for porosity of zone i, d_i for depth of the zone, R_i for associated bulk retention coefficient):

$$R' = 1 + \frac{1}{e} \sum_{i=1}^{i=N} \epsilon_i d_i R_i \tag{6.1}$$

- For Case B1 (Fig. 6.14), similar analysis can be done whereas Gouge as well as Cataclasite presents the fracture type behavior. Non altered zones play a minor role for short time behavior but dominant role in tailing effects.
- For Case C1 (Fig. 6.15), similar analysis pertains. Mass is dominantly present in altered and non altered zones, the latter mainly controlling the transfer for the larger temporal part of the phenomenon. Nevertheless, here, Gouge, Cataclasite as well as altered zones behave as an extended fracture zone. Transitory storage is limited to non altered zones.

As a conclusion, as the regimes move to slower, transfer is dominated by matrix diffusion leading to strong delays of peak and tailing effect. For the quicker flow regime, only Gouge follows the fracture regime, for the intermediate, Gouge as well as Cataclasite do, for the slower altered zone should be added to these. This means that these systems can be simplified considering an equivalent R' as developed before. For instance for the slower regime, the system is equivalently represented by a R' involving Gouge, Cataclasite and Altered zone properties and a classical matrix zone corresponding to non altered properties.

But, although this results are interesting, a more distant though exiting aim to reach should consist in inferring such regimes from the simple facts of fracture and matrix zone properties as well as head gradient imposed. Based on analytical expressions and simple considerations (refer to section 6.4.3 efforts for instance) it would be interesting to come up with a simplified equivalent system that could be directly used in the larger 200 m block model. This aim is more ambitious than the perspectives considered in Task6F as a bench mark test. This is nevertheless interesting in the view of the understanding of the system and could provide practical applications in Task6E framework. This was not done here but efforts will have to be put into it in the future.

Evolution of masses for cases A2, B2, C2 (pure Type 2, Feature 4S)

We refer in the following to figures 6.16, 6.17 and 6.18 providing the evolution of masses in the different matrix sub units for all tracers and cases. On these figures, only altered

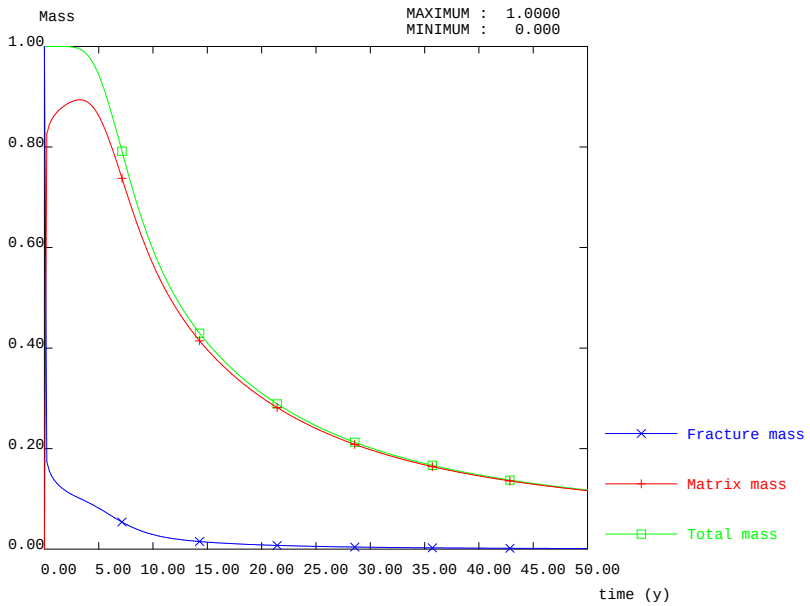

Figure 6.12: Evolution of masses (total mass, mass in fracture and in all matrix zones), Iodine, intermediate regime, Case B1. $t_{peak} = 7.17y$

and non altered zones are presented since we deal with Type 2 feature (see Fig. 6.2(b)). As mentioned before, fracture coating is included in the fracture properties by means of a retention coefficient. We include a mention of peak arrival times for each case in the figure caption (one may refer as well to table 6.5). We propose here some comments:

- For Case A2 (Fig. 6.16), mass remains in the vicinity of the fracture. The amount of mass is negligible in non altered zones, it is mainly located in altered rock zone.
- For Case B2 (Fig. 6.17), the importance of non altered zone increases.
- For Case C2 (Fig. 6.18), transfer is mainly controlled by the non altered zone. Altered rock zone follows a fracture type regime.

As a conclusion, as the regimes move to slower, transfer is dominated by deeper non altered rock leading to strong delays of peak and tailing effect. For the slower flow regime, altered zone can be represented by means of the equivalent approach presented before. Nevertheless, although finding an equivalent system is easy based on such simulation including the whole heterogeneity of the system, it is not straightforward to infer it simply from the fracture and matrix zones properties and the head gradient imposed to the system. We still have work ahead to fulfill this.

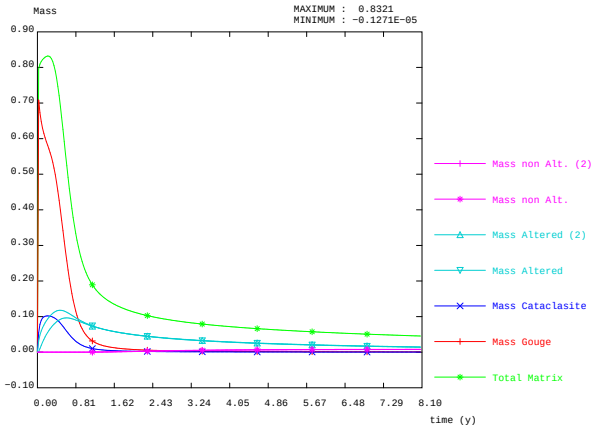

(a) Case A1, Iodine, $t_{peak} = 0.56y$

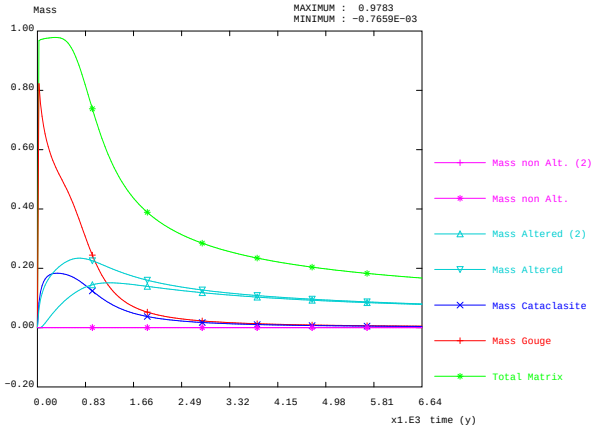

(b) Case A1, Cesium, $t_{peak} = 901.78y$

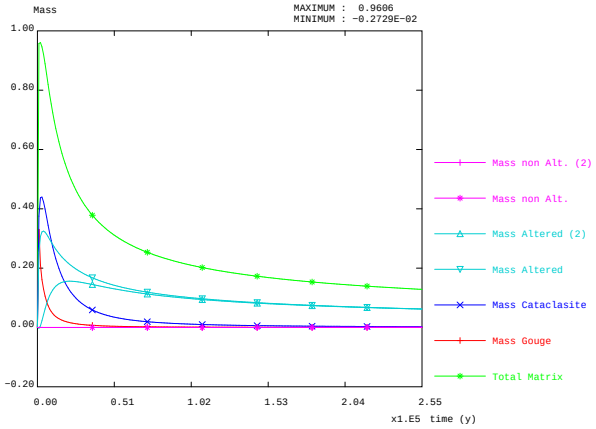

(c) Case A1, Americium, $t_{peak} = 6097.5y$

Figure 6.13: Case A1 (Feature 1S, Type1, quick regime): Evolution of masses in sub units (Gouge, Cataclasite, Altered and non altered zones on both sides of the fracture)

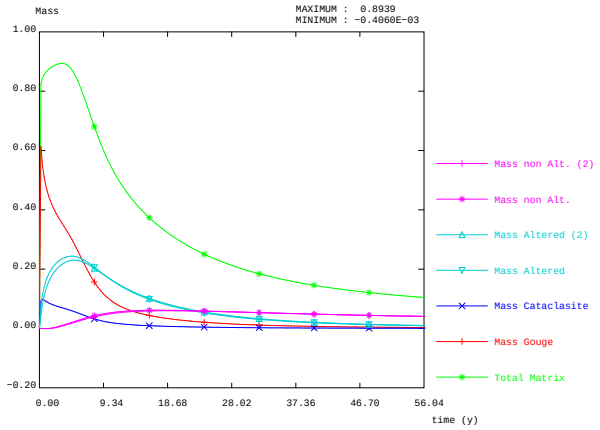

(a) Case B1, Iodine, $t_{peak} = 7.17y$

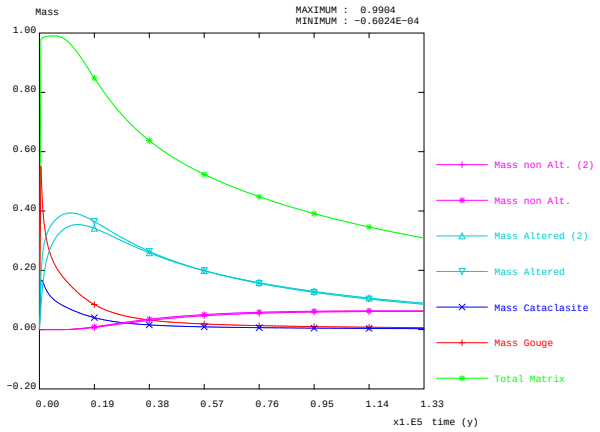

(b) Case B1, Cesium, $t_{peak} = 16975.y$

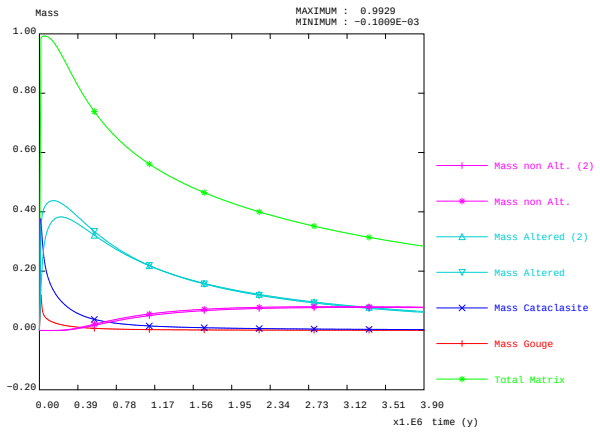

(c) Case B1, Americium, $t_{peak} = 2.90E5y$

Figure 6.14: Case B1 (Feature 1S, Type1, medium regime): Evolution of masses in sub units (Gouge, Cataclasite, Altered and non altered zones on both sides of the fracture)

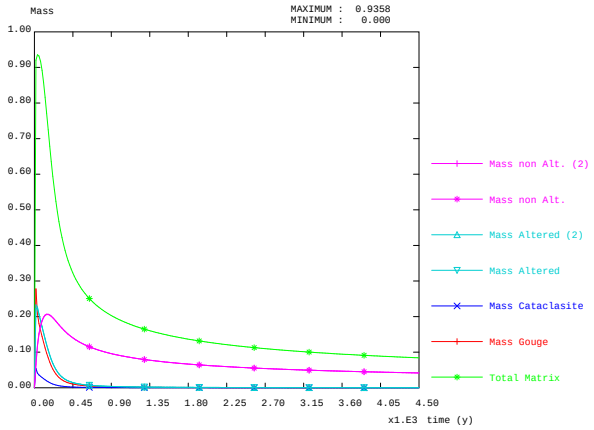

(a) Case C1, Iodine, $t_{peak} = 161.39y$

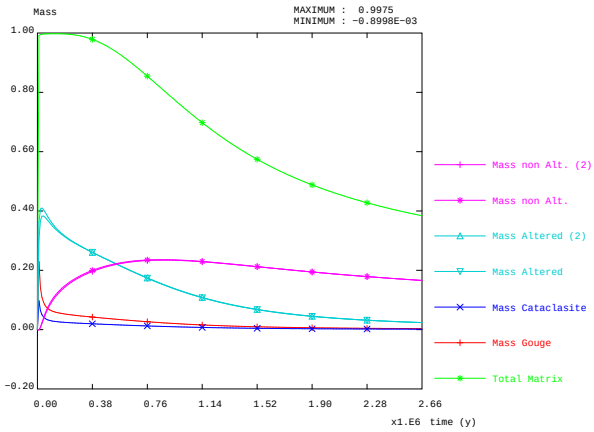

(b) Case C1, Cesium, $t_{peak} = 8.59\,10^5 y$

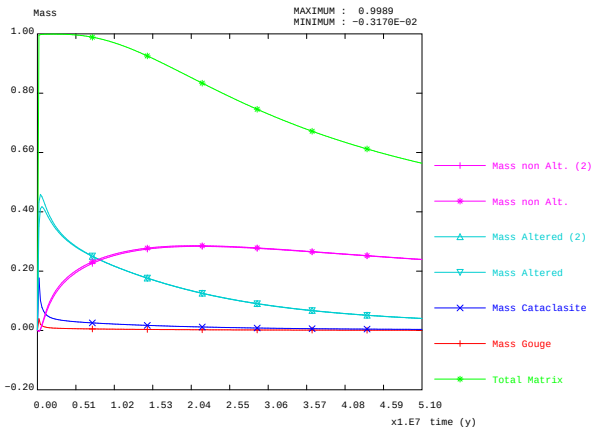

(c) Case C1, Americium, $t_{peak} = 2.01\,10^7 y$

Figure 6.15: Case C1 (Feature 1S, Type1, low regime): Evolution of masses in sub units (Gouge, Cataclasite, Altered and non altered zones on both sides of the fracture)

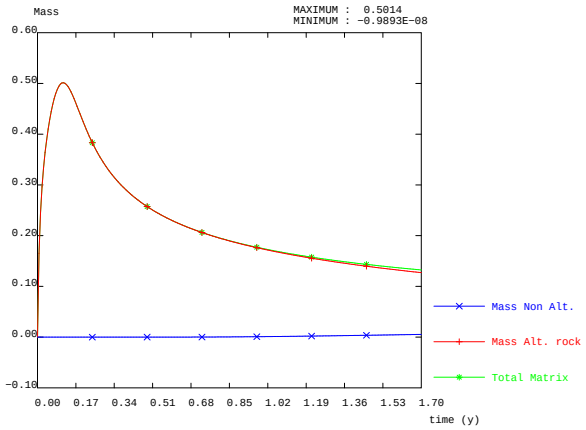

(a) Case A2, Iodine, $t_{peak} = 0.14y$

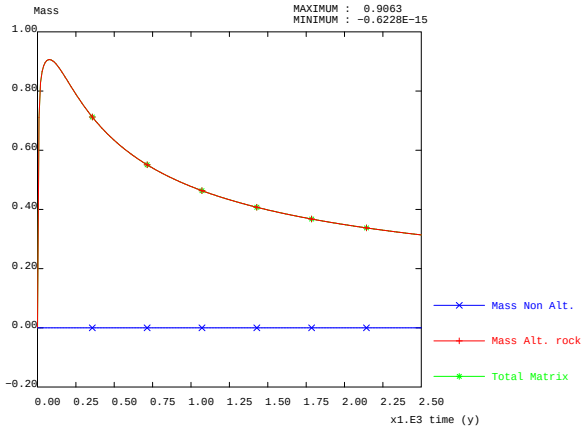

(b) Case A2, Cesium, $t_{peak} = 169.79y$

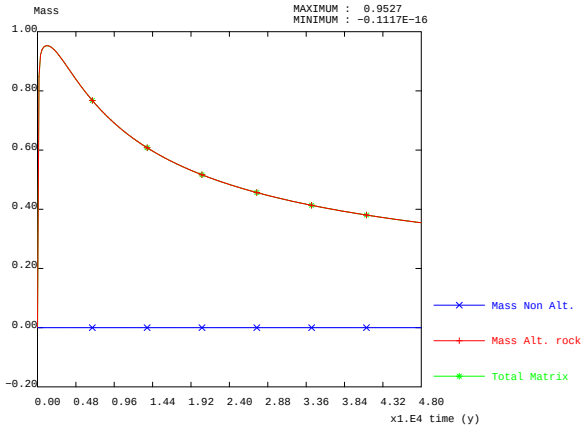

(c) Case A2, Americium, $t_{peak} = 3638.2y$

Figure 6.16: CaseA2 (Feature 4S, Type2, quick regime): Evolution of masses in sub units (Gouge, Cataclasite, Altered and non altered zones on both sides of the fracture)

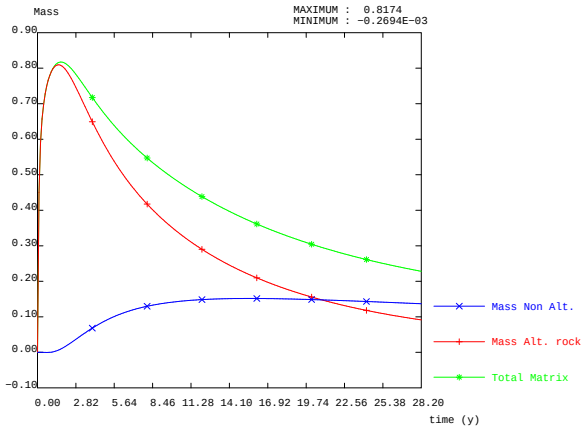

(a) Case B2, Iodine, $t_{peak} = 2.70y$

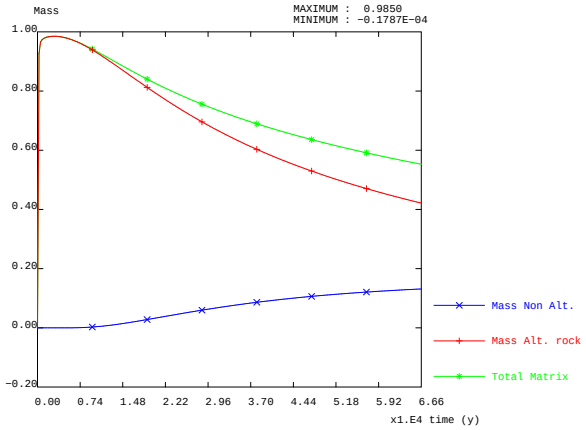

(b) Case B2, Cesium, $t_{peak} = 12518.y$

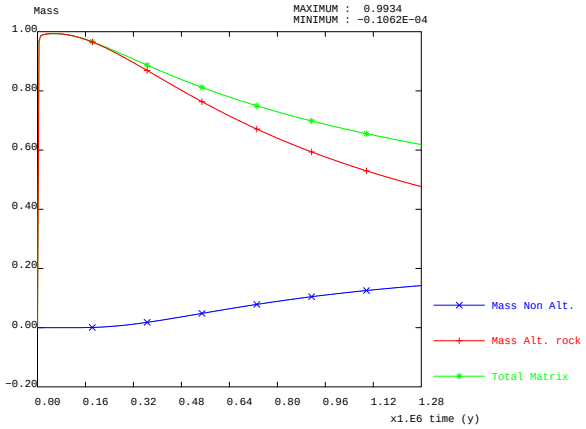

(c) Case B2, Americium, $t_{peak} = 3.06\ 10^5 y$

Figure 6.17: Case B2 (Feature 4S, Type2, medium regime): Evolution of masses in sub units (Gouge, Cataclasite, Altered and non altered zones on both sides of the fracture)

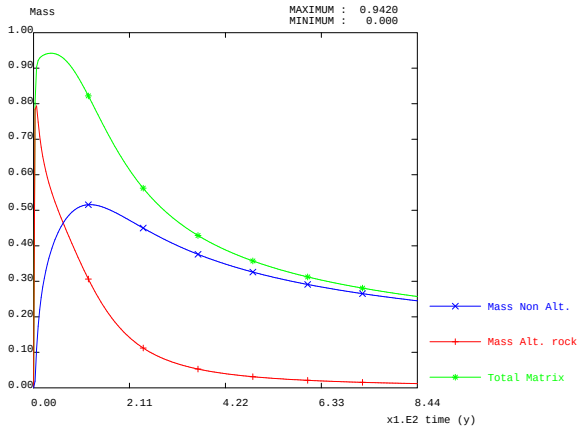

(a) Case C2, Iodine, $t_{peak} = 131.55y$

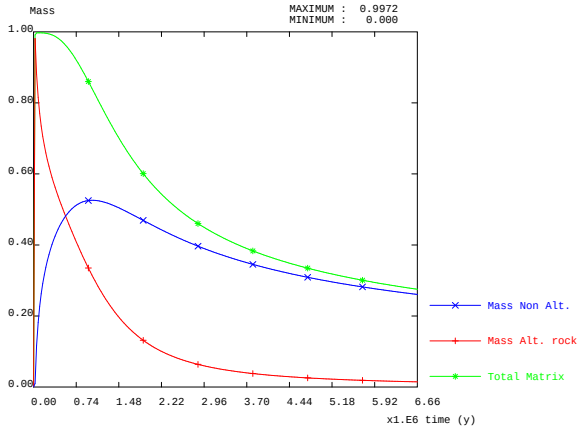

(b) Case C2, Cesium, $t_{peak} = 1.10\,10^6 y$

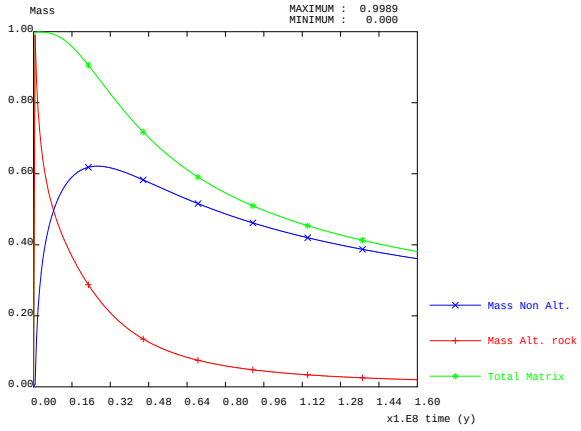

(c) Case C2, Americium, $t_{peak} = 2.81\,10^7 y$

Figure 6.18: Case C2 (Feature 4S, Type2, low regime): Evolution of masses in sub units (Gouge, Cataclasite, Altered and non altered zones on both sides of the fracture)

6.4.2 Impact of pure Type 1 versus pure Type 2 for Feature 1S, simulation cases A3, B3, C3

One general remark for the different simulations conducted (ABC1s versus ABC2s) is that when the regimes move to slower and in addition sorbing properties raise, breakthrough curves for Type 1 and for Type 2 cases seem to become identical. This is studied here considering a new series of cases involving the same feature (Feature 1S) for Type 2 matrix properties. Cases A3, B3, C3 defined as such can be easily confronted to Cases A1, B1, C1 involving the same Feature 1S but for pure Type 1 properties. We present the associated results as well as an analysis of the comparison.

So, we create a third series of simulation cases by considering Feature 1S as a pure Type 2. Depending on the flow regimes these are labeled A3, B3, C3 respectively for quick, medium and slow flow regimes (0.1 y, 1 y, 10 y). Results are provided on tables 6.7 and 6.8 and Fig. 6.19.

Results show indeed that when moving to slower regimes and as well for tracer of increasing sorbing properties, breakthrough curves for pure Type 1 and pure Type 2 come closer and even tend to provide identical peak arrival times. The shape of the curves remain nevertheless different, the curves associated with A3 to C3 having a larger spread a typical diffusive pattern. The curves associated with A1 to C1 are to be understood based on the equivalence studied formerly: Gouge and Cataclasite contribute as a corrected retention coefficient so that the velocity is lower, dispersion in fracture lower as well and the correction with matrix diffusion phenomenon is lower. As a consequence, breakthrough curves are stiffer. Explanations for this coming closer of pure Type 1 and pure Type 2 are the fact that for slower regimes, transfers are dominantly controlled by matrix zones. In addition, the volume of the matrix rock containing mass (see Table 6.3 for penetration depths) is dominated by the non altered rock fraction. The tendency is stronger for sorbing tracers due to higher K_d in altered and non altered zones as compared with Cataclasite and Gouge. Retardation coefficients as well as values of different coefficients involved in the calculation of masses are provided on Tab. 6.9, 6.10 and 6.11. These are discussed in the next section.

Peak arrival	A1	B1	C1	A3	B3	C3
Iodine, Max. Fl., (1/y)	1.57	7.94E-02	2.80E-03	5.22	0.13	3.80E-03
Iodine, Ass. Time (y)	0.56	7.17	161.39	0.13	2.19	98.72
Cesium, Max. Fl., (1/y)	6.78E-04	1.53E-05	4.28E-07	1.68E-03	1.84E-05	4.39E-07
Cesium, Ass. Time (y)	901.78	16975.	8.59E+05	109.03	7683.7	7.68E+05
Americium, Max. Fl., (1/y)	3.61E-05	6.45E-07	1.29E-08	7.02E-05	7.44E-07	1.30E-08
Americium, Ass. Time (y)	6097.5	2.89E+05	2.01E+07	2237.9	1.86E+05	1.93E+07

Table 6.7: Peak arrival time and associated maximum fluxes (Mass Dirac injection) for Feature 1S as pure Type 1 or pure Type 2

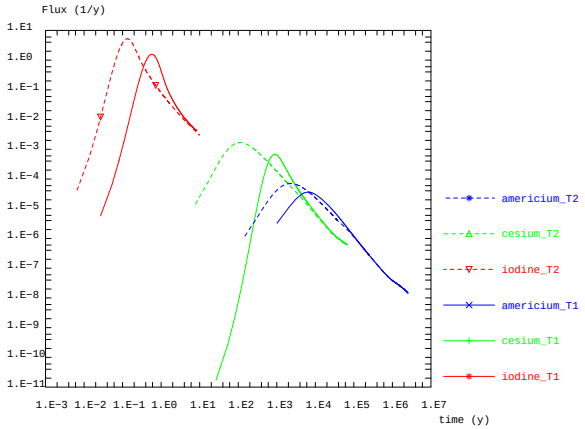

(a) Case A1, A3

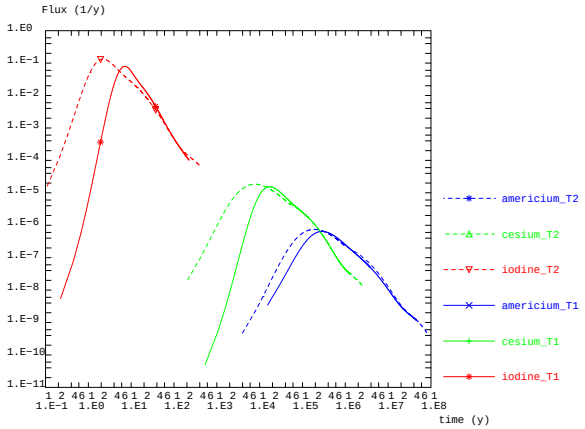

(b) Case B1, B3

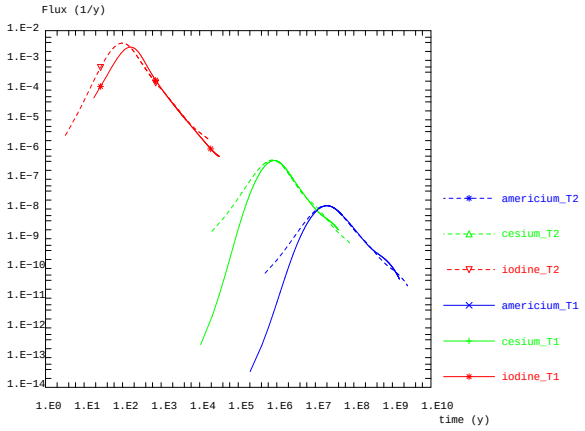

(c) Case C1, C3

Figure 6.19: Feature 1S, as pure Type 1 and Type 2: BTC for Iodine, Cesium, Americium, dots for pure Type 2 (A3, B3, C3) and solid line for Type 1 (A1, B1, C1)

Times	A1	B1	C1	A3	B3	C3
Iodine, T5 (y)	0.36	4.81	80.69	8.22E-02	1.48	54.29
Iodine, T50 (y)	0.68	12.21	277.95	0.18	7.07	202.38
Iodine, T95 (y)	7.14	152.17	12967.	6.41	143.39	11022.
Cesium, T5 (y)	623.29	12466.	5.03E+05	73.982	5710.9	4.25E+05
Cesium, T50 (y)	1445.5	62329.	1.84E+06	564.60	62300.	1.71E+06
Cesium, T95 (y)	54770.	1.20E+06	3.85E+07	53131.	1.17E+06	7.01E+07
Americium, T5 (y)	3556.9	1.90E+05	1.24E+07	1566.5	1.37E+05	1.11E+07
Americium, T50 (y)	22866.	1.44E+06	6.60E+07	13651.	1.59E+06	6.14E+07
Americium, T95 (y)	1.38E+06	4.17E+07	1.13E+09	1.33E+06	4.20E+07	1.92E+09

Table 6.8: Comparison Feature 1S as pure Type 1 or pure Type 2: times associated with arrival of 5%, 50% and 95% of the injected mass

6.4.3 Estimation of the delays associated with sorption and matrix diffusion from analytical expressions

We explore here the same question as in preceding section but in a more quantitative way. We provide here a way of controlling quantitatively the transfer times associated with the different phenomenon at stake: advection, sorption, matrix diffusion. We focus exclusively on the peak arrival time for which considerations from simple systems involving fracture transport as well as matrix diffusion are involved.

The first model to be considered is the one introduced formerly dealing with the delay in arrival time associated with fracture zones that are immediately filled up and in fact behave as buffers following the fracture regime. These zones contribute in the way of an equivalent retardation factor to the transfer (R' from equation 6.2, ϵ for porosity, R for retardation coefficient, e for fracture aperture):

$$R' = 1 + \frac{1}{e}\sum_{i=1}^{i=N} \epsilon_i d_i R_i \tag{6.2}$$

The second model to be considered here captures the delay in peak arrival time associated with pure fracture advection and 1D orthogonal diffusion in an infinite matrix. This is the basic model by [*Neretnieks et al. 80*]. Calculation of the position of the peak arrival time for input Dirac leads to a retardation factor which is function of the water travel time as written below (see R'' from equation 6.3, D_p for pore diffusion coefficient, t_w for water travel time):

$$R'' = 1 + \frac{2}{3}\frac{\epsilon^2 D_p R}{e^2} t_w \tag{6.3}$$

The limit of these models for prediction is that the systems considered for the present task present heterogeneous matrix features (that the second model fails to describe) and that the first does not include matrix diffusion acting in a classical way (intermediate storage and delayed release of mass).

Nevertheless for some cases described formerly, the system can be represented equivalently as a fracture with equivalent properties and a matrix system simplified to the matrix zone in the vicinity of the equivalent fracture (see former section and [*Grenier 03*]). In such a case, one can prove that the final delay in peak arrival time corresponds to the sum of both delays resulting from the first and second model.

Estimation of the time associated requires the following steps:

- Advective travel time associated with water movement: t_w = 0.1 y, 1 y, 10 y for the 3 cases considered.
- Sorption onto fracture walls corresponds here to diffusion and sorption into the bulk of fracture coating. Retardation coefficients R_a associated with the presence of fracture coating are provided on Table 6.9 for the features considered (Feature 1S and 4S). Retardation coefficient in the bulk of other matrix zones are provided in the same Table 6.9. The associated travel times in the fracture are expressed as : $t_{fr} = R_a t_w$.
- The same considerations can be extended to other matrix zones in the vicinity of the fracture if the time required to fill up these zones is small enough as compared with the total transfer time in the system. Such zones (refer to the previous section providing the evolution of mass in the sub units) follow the same regimes as the fracture itself and can be represented equivalently as a retardation coefficient. The expression for this coefficient is recalled in Equation 6.2.
- Another consequence of the presence of matrix zones, is that the peak arrival time can be strongly delayed. The shape of the curve is in this case typical of matrix diffusion providing large tailing effects. The delay in the peak arrival time is reduced for low matrix diffusion effects but can be dominant for large matrix diffusion effects or low velocity of the flow in the fracture. The expression for the delay in peak arrival time is provided in Equation 6.3.
- The estimation of the total delay in peak arrival time corresponds to the sum of both contributions: $t_{peak} = (R' + R'')t_w$.

We confront here these assessments with the results obtained from the simulations. In these cases the evolution of masses in the matrix subunits directly provides with the behavior of the various subunits: those behaving as classical matrix diffusion zones and those following the fracture regime.

A first verification step consists in coming back to the plotted curves of the evolution of masses in the various sub units for previous section and check the results. For instance, for the Feature 1S case, for the slow regime (Case A1), Gouge behaves as the fracture whereas the other units following a typical matrix diffusion behavior. Among those, Cataclasite plays the larger role (Cesium and Americium), closely followed by altered zones for Iodine. As a consequence, R' should include fracture coating and gouge and we consider here cataclasite as the dominant matrix zone contributing to R''. The associated

delay is the addition of both contributions. All the figures associated with the Feature 1S case are plotted on Table 6.10. Application leads to retardation coefficients by 4.88 for Iodine, 8227 for Cesium and 65634 for Americium. The associated actual factors are 5.6 for Iodine as resulting from the simulations (see Fig. 6.13 and Tab. 6.5), 9018 for Cesium and 60995 for Americium. The estimations are fair. The same was conducted for Cases B1 (one should count Gouge and Cataclasite to fracture type regime and altered rock as the major component of to matrix type) and Case C1 (Gouge, Cataclasite, Altered rock as fracture like and non altered as matrix type). The estimations are all satisfactory roughly within 10% and never larger than 50% in the worst cases.

Similar results were obtained for cases A2 to C2. The coefficients related are summed up on Table 6.11. The intermediate regime (Case B2) nevertheless does is not well estimated due to the fact that both altered and non altered rock units are involved as matrix diffusion zones. A kind of average of the impact of both zones could be considered but the retardation coefficients R'' for each zone differ enough.

Retardation coef.	Fract. (1S)	Fract. (4S)	Gouge	Cataclasite	Altered Rock	Non altered rock
Iodine	1.0969	1.1244	1.	1.	1.	1.
Cesium	259.59	332.92	1729.0	4010.5	8947.0	8974.0
Americium	2486.6	3191.4	5401.0	1.33E+05	2.23E+05	4.48E+05

Table 6.9: Retardation coefficients. Coefficients associated with fracture correspond to the inclusion of fracture coating as R_a coefficient

6.5 Conclusions

Results from simulations conducted on Feature 1S and 4S show that matrix diffusion becomes the most important retention phenomenon as one moves to low flow regimes more typical of post closure time scales.

For Type 1, the shape of breakthrough curves is impacted by the presence of highly porous zones in the vicinity of the fracture that act as retention coefficient (more symmetrical). For Type 2, the breakthrough curves have large spreads typical of diffusion processes. This diffusive component increases as water arrival time increases (0.1 y, 1 y and 10 y were considered) and breakthrough curves corresponding to pure Type 1 and pure Type 2 situations tend to come closer to each other. The same is true when moving to more sorbing cases. This is due to the large impact of altered and non altered properties over the properties of the other zones (mostly related with larger depths and K_d which compensate slightly lower diffusion coefficient and porosities).

Equivalent models to represent features associated with Type1 and Type 2 heterogeneous matrix zones were suggested based on understanding of the evolution of masses in sub units.

	Fract. coating	Gouge	Cataclasite	altered rock	non altered
Iodine, $\epsilon_k d_k R_k$ (m)	2.50E-05	1.00E-03	2.00E-04	1.20E-03	6.00E-04
Iodine, $1 + \frac{1}{e}\epsilon_k d_k R_k$	1.10	4.88	1.77	10.30	5.65
Iodine, $R' = 1 + \frac{1}{e}\sum_{i=1}^{i=k} \epsilon_i d_i R_i$	1.10	4.97	5.75	15.05	19.70
Cesium, $\epsilon_k d_k R_k$ (m)	6.67E-02	1.7290	0.80210	10.736	5.3844
Cesium, $1 + \frac{1}{e}\epsilon_k d_k R_k$	259.59	6702.6	3109.9	83229.	41741.
Cesium, $R' = 1 + \frac{1}{e}\sum_{i=1}^{i=k} \epsilon_i d_i R_i$	259.59	6961.1	10070.	93298.	1.35E+05
Americium, $\epsilon_k d_k R_k$ (m)	0.64	5.40	26.73	268.38	269.19
Americium, $1 + \frac{1}{e}\epsilon_k d_k R_k$	2486.6	20935.	1.04E+05	2.08E+06	2.087E+06
Americium, $R' = 1 + \frac{1}{e}\sum_{i=1}^{i=k} \epsilon_i d_i R_i$	2486.6	23421.	1.27E+05	2.21E+06	4.29E+06
Iodine, A1 quick regime, R''		758.03	0.31	8.86E-02	1.50E-02
Iodine, B1 median regime, R''		7580.3	3.15	0.88	0.15
Iodine, C1 slow regime, R''		75803.	31.58	8.86	1.50
Cesium, A1 quick regime, R''		1.31E+06	1266.7	793.51	135.20
Cesium, B1 median regime, R''		1.31E+07	12667.	7935.1	1352.0
Cesium, C1 slow regime, R''		1.31E+08	1.26E+05	79351.	13520.
Americium, A1 quick regime, R''		4.09E+06	42213.	19836.	6759.3
Americium, B1 median regime, R''		4.09E+07	4.22E+05	1.98E+05	67593.
Americium, C1 slow regime, R''		4.09E+08	4.22E+06	1.98E+06	6.75E+05

Table 6.10: Coefficients R" and R' associated with Feature 1S (pure Type 1). For non altered rock and R', we considered here an arbitrary depth by $20cm$.

We focused in particular our attention on peak arrival times for the various cases. Coefficients derived from simple analytical expressions to estimate the effects of matrix diffusion on the retardation of peak arrival time were proposed. The retardation factors associated (ratio between peak arrival time and water arrival time) are measured from breakthrough curves and confirmed by our approach by means of former analytical coefficients. They range (in years):

- from 5.6 to 16.1 for Iodine, Cases A1 to C1 and from 1.4 to 13.1 for Iodine, Cases A2 to C2;
- from $9018.$ to $8.6\,10^4$ for Cesium, Cases A1 to C1 and from $1698.$ to $1.1\,10^5$ for Cesium, Cases A2 to C2;
- from $60975.$ to $2.0\,10^6$ for Americium, Cases A1 to C1 and from $36382.$ to $2.8\,10^6$ for Americium, Cases A2 to C2.

The purpose of Task 6F as a bench mark task is fulfilled by the results presented here. Nevertheless, the single fracture systems studied here provide an interesting basis for a more in depth understanding of the transport regimes of larger features within the 200 m semi synthetic fractured block as well as the possible ways to simplify the system for post closure time scales. Further work would be interesting along the line of providing an easy way of finding the transport regimes as well as the simplified models to be considered for

	Fract. coating	altered rock	non altered
Iodine, $\epsilon_k d_k R_k$ (m)	2.50E-05	1.20E-03	6.00E-04
Iodine, $1 + \frac{1}{e}\epsilon_k d_k R_k$	1.1244	12.940	6.9701
Iodine, $R' = 1 + \frac{1}{e}\sum_{i=1}^{i=k} \epsilon_i d_i R_i$	1.1244	19.035	25.005
Cesium, $\epsilon_k d_k R_k$ (m)	6.67150E-02	10.736	5.3844
Cesium, $1 + \frac{1}{e}\epsilon_k d_k R_k$	332.92	1.06831E+05	53577.
Cesium, $R' = 1 + \frac{1}{e}\sum_{i=1}^{i=k} \epsilon_i d_i R_i$	332.92	1.19755E+05	1.73331E+05
Americium, $\epsilon_k d_k R_k$ (m)	0.64128	268.38	269.19
Americium, $1 + \frac{1}{e}\epsilon_k d_k R_k$	3191.4	2.67046E+06	2.67851E+06
Americium, $R' = 1 + \frac{1}{e}\sum_{i=1}^{i=k} \epsilon_i d_i R_i$	3191.4	2.83351E+06	5.51202E+06
Iodine, A2 quick regime, R''		0.14612	2.48223E-02
Iodine, B2 median regime, R''		1.4612	0.24822
Iodine, C2 slow regime, R''		14.612	2.4822
Cesium, A2 quick regime, R''		1307.4	222.76
Cesium, B2 median regime, R''		13074.	2227.6
Cesium, C2 slow regime, R''		1.30737E+05	22276.
Americium, A2 quick regime, R''		32681.	11137.
Americium, B2 median regime, R''		3.26807E+05	1.11365E+05
Americium, C2 slow regime, R''		3.26807E+06	1.11365E+06

Table 6.11: Coefficients R" and R' associated with Feature 4S (pure Type 2). For non altered rock and R', we considered here an arbitrary depth by $20cm$.

these units. This would be an important contribution to Task 6E issues and would as well provide a sound basis for Task 6F2.

Chapter 7

Task 6F2

Studies are developed along two directions:

- Impact of the complexity of fractures considering Type 1 and Type 2 units in series and in parallel.
- Impact of connectivity of the fractures on the actual shape of breakthrough curves, special case of sugar box geometry and triple porosity block.

7.1 Complexity of the fractures

We report here briefly about some modeling efforts made in the direction of including full complexity of the fractures as provided in the deliveries. Indeed, major fractures are potentially composed of a network of finer fissures of type 1 or 2. Minor features are of simpler geometry and composition.

We considered the issue of complexity considering:

- A fracture consisting of Type 1 and 2 in series (proportions varying from full Type 1 to full Type 2 as bounding cases). Results show that breakthrough curves provide a unique peak and can be approached by an equivalent model (advection, dispersion, matrix diffusion).
- Two fractures of Type 1 and Type 2 assembled in parallel for different proportions of flow flowing into the Type 1 or Type 2 unit. For this so called intermediate case, flow rates are equally divided onto both fissure and fissure apertures are divided by a factor of 2. Results show multi peak breakthrough curves which are not to be represented by a simple equivalent model. Pure Type 1 and Type 2 are no more bounding cases since retardation acts stronger for a half aperture fracture than for a full aperture for equal water travel times. Results would anyway differ for other

relative distributions of flow rates and related fracture apertures. These distributions are not well constrained from the available information leading to large uncertainties in dealing with complexity of fractures.

- The special case of Feature 6D is treated leading to non trivial breakthrough curve.

Results show that complex configurations can not be approached by means of a simple equivalent system (advection, dispersion, heterogeneous matrix diffusion). Moreover, uncertainties in terms of minor fissures openings as well as distributions of flow rates diverted into these units, are largely unconstrained by experimental data though leading to major differences in breakthrough curves. As a consequence, we simply considered major type associated with each fracture without introduction of complexity (only one single flow channel) for Task 6E. In such a case, pure Type 1 and pure Type 2 correspond to bounding cases studied in a sensitivity analysis.

Breakthrough curves are provided on figures 7.2. Configurations are illustrated on figures 7.1. Configurations in parallel and series involve feature 1S properties and a total length of 20 m. Structure 6D considers properties of fracture 4S with a total length of 20 m.

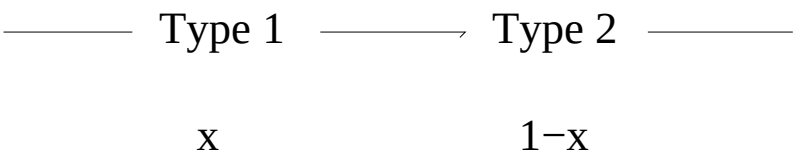

(a) Type1 and Type 2 in series

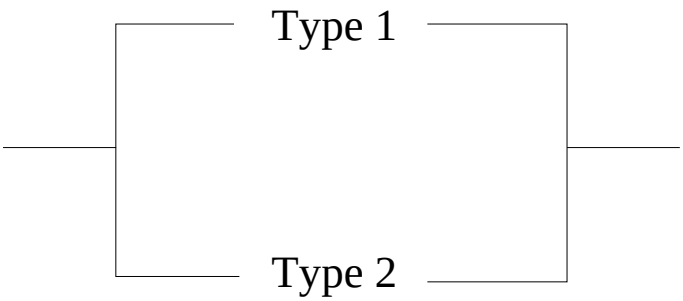

(b) Type1 and Type 2 in parallel

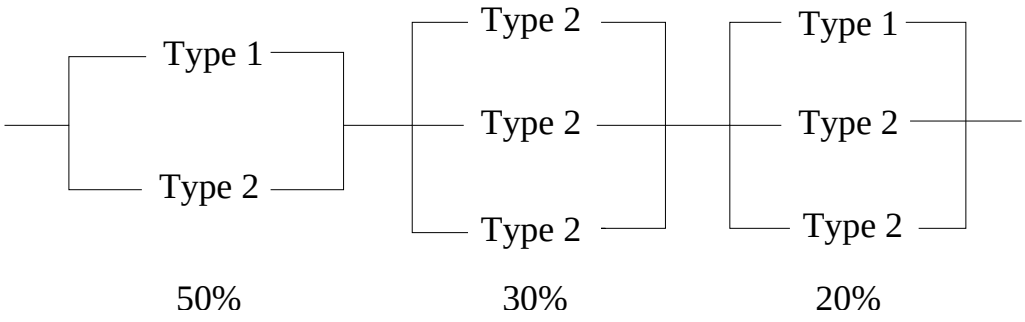

(c) Feature 6D

Figure 7.1: Configurations considered

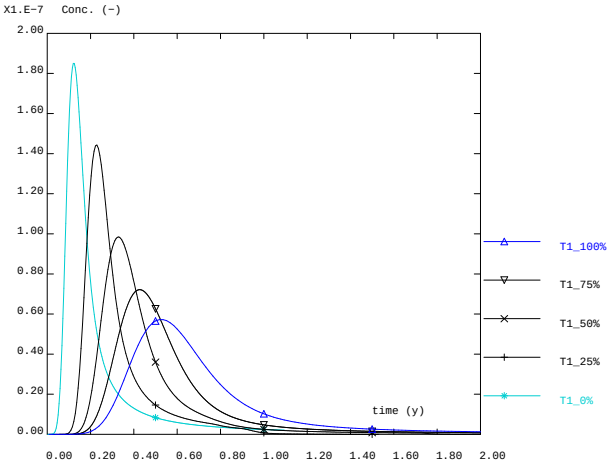

(a) Type1 and Type 2 in series

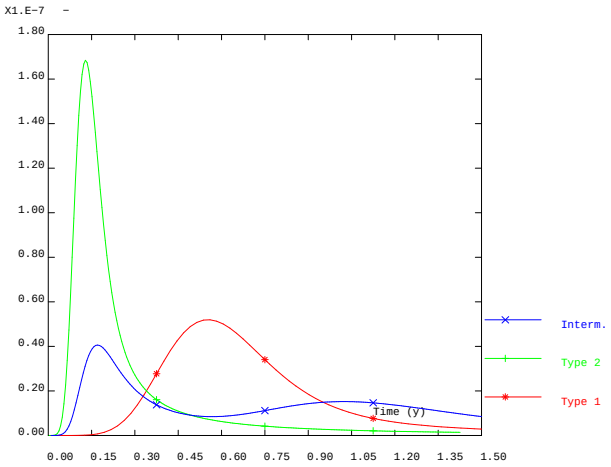

(b) Type1 and Type 2 in parallel

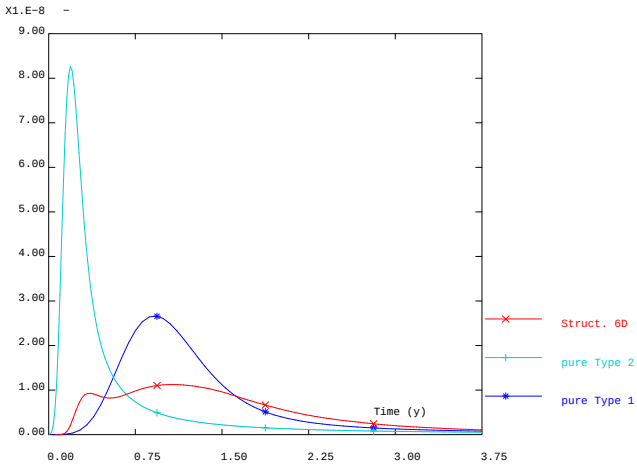

(c) Feature 6D

Figure 7.2: Complexity of fractures: 3 numerical experiments

7.2 Influence of fracture network connectivity on transport properties

Our purpose in this section is to show the type of breakthrough curves corresponding to transfers in a fully connected fractured block (sugar box geometry). Indeed some of the results and conclusions made based on the semi synthetic block of Task 6C are in close connection with the actual structure of the fractured network, in particular its low connectivity. Our focus here is to show that results obtained concerning the major influence of matrix diffusion on the delay of breakthrough curves pertain but that the shape of the breakthrough curves can largely depend on the actual connectivity of the fractured network. As mentioned earlier, the fracture network geometry considered here is regular sugar box geometry. This geometry is interesting to draw theoretical considerations, it is nevertheless clearly not a true representation of any actual site, in particular not Block Scale site. It is nevertheless a practical way to study the role played by limited matrix diffusion effects as related with back ground fracturing. The interest of the present exercise indeed relies in the fact that most simulation approaches among the modeling teams working on Task 6E have limited their approaches to the conceptualization of matrix diffusion as an orthogonal 1D diffusion process (should it be bounded or unlimited, related to homogeneous or heterogeneous matrix properties). For other (a real world ?) applications where connectivity of the fractured network can be large at various scales, this 1D approach is too limited, actual meshing of the actual matrix block geometries is required since diffusion a matrix block is fully 3D: tracers diffuse from all sides of the block into the actual block geometry and diffusion depends on history of concentrations at the boundaries as well as geometrical and diffusion properties. For PA time scales considered in Task 6E, diffusion is to occur over meters to tens of meters, which is already large as compared with the 200 m of the total block studied. In such a case and for more connected systems as the semi synthetic block of Task 6C, simplification of matrix diffusion to 1D orthogonal diffusion is no more possible.

We study such a case below with our Eulerian continuum approach where matrix blocks are fully discretized. We consider a 2D sugar box geometry for a block of 150 meters. This block contains 10*10 fractures. One may refer to figure 7.3, 7.4 and tables 7.1, 7.2 et 7.3. We apply typical Task 6E properties to these fractures as well as Type 1 matrix properties. We first compute the breaktrough curves for this dual porosity block. It shows as a classical matrix diffusion type curve including large delay in peak arrival time as well as large tailing effect (related with large diffusion zones, here block size is 15 m). In a second step, we include a second level of fracturation in-bedded into the former larger scale one: each block by 15 m is no more homogeneous but consists of a regularly fractured block containing 10*10 fractures bounding 1.5 m blocks. We thus obtain there a triple porosity system within a 150 m block (larger 15 m blocks containing a second scale of fracturation providing 1.5 m small blocks). The properties associated with this second scale of fracturation were obtained from the deliveries associated with Task 6C block for such smaller scale fractures and coated with Type 2 matrix properties.

The boundary conditions correspond to a uniform flow directed along the diagonal of the block. The intensity is 10^{-3}, typical of PA time scales. The initial Dirac concentration is located upstream at major fractures intersections. Flux drawn on the various figures corresponds to the total flux transiting through the downstream boundaries. See figure 7.4.

Results are provided on figures 7.5 for the intermediate case where matrix diffusion is not considered (one or two levels of fracturation) and on figures 7.6 for the case including matrix diffusion (double and triple porosity systems).

The results proposed on these figures are discussed below. Detailed analysis of such systems is not attempted here. In particular, for other parameter values (associated with fracture or matrix properties, other head gradient ...) the breakthrough curves are to differ. We simply consider the present study as illustrative. We moreover limit here our study to a non sorbing tracer.

Results show:

- Without matrix diffusion: the full system (both levels of fracturation) provides delayed arrival time with lower dispersivity (see Fig. 7.5-(b)). This is due to the fact that total porosity of the block is increased when moving from single to double fracturation. Lower dispersivity is explained by the fact that equivalent dispersion for such regular systems is linearly related with the size of the matrix block (15 m for the larger scale and 1.5 m for the smaller). These curves are most related with the parameters considered. Indeed, velocities in the large fracture systems and in the smaller are here comparable. For other situations, introduction of a smaller scale of fracturation can lead to a kind of tailing when flow velocity is significantly lower, leading to retardation of the plume in such zones. As mentioned formerly, we considered the transmissivity and fracture aperture properties provided in the deliveries and summed up in tables 7.1, 7.2 et 7.3. Masses, as provided on figure 7.5-(b) vary at similar time scales for both cases.

- With matrix diffusion: the first system considers large matrix blocks for a single scale of fracturation. It leads to large tailing effects (see Fig. 7.6-(a)). When including minor fracturation with associated matrix diffusion, peak arrival time is strongly delayed (due to increased porosity and matrix volumes) but rather leads to a symmetrical breakthrough curve. This is due to the fact that 1.5 m blocks are fully invaded by the plume leading to increased equivalent porosity without transitory buffer effect. The important fact is here that the type of retardation is very different from the usual long tailing effect observed for the Task 6E system indeed mainly corresponding to a single major transport path (along 12 fractures).

So, the present study confirms the importance of matrix diffusion for retardation of transfer of a plume in a fractured block at PA time scale. Nevertheless, the results obtained in Task 6E are to a large extent bound to the geometry considered (from Task 6C) and should not be generalized in a too straightforward way. For the point considered here, the

impact of matrix diffusion in terms of distribution of arrival times may very well depend on the connectivity of the fractured network (as well as the parameters associated with the properties of the different units - not illustrated here). For instance, here including a minor level of fracturation if considered fully connected (sugar box geometry) leads to more retarded outputs but providing larger intensity. For a criterion of maximum peak lower than a provided level, situation associated with this minor fracturation is not conservative. The triple porosity systems transfers the whole of the mass of the plume quicker than the dual porosity system. These results should anyway help in understanding that the results obtained in Task 6E are partially bounded to the situation of low connectivity of the geometrical fracture network.

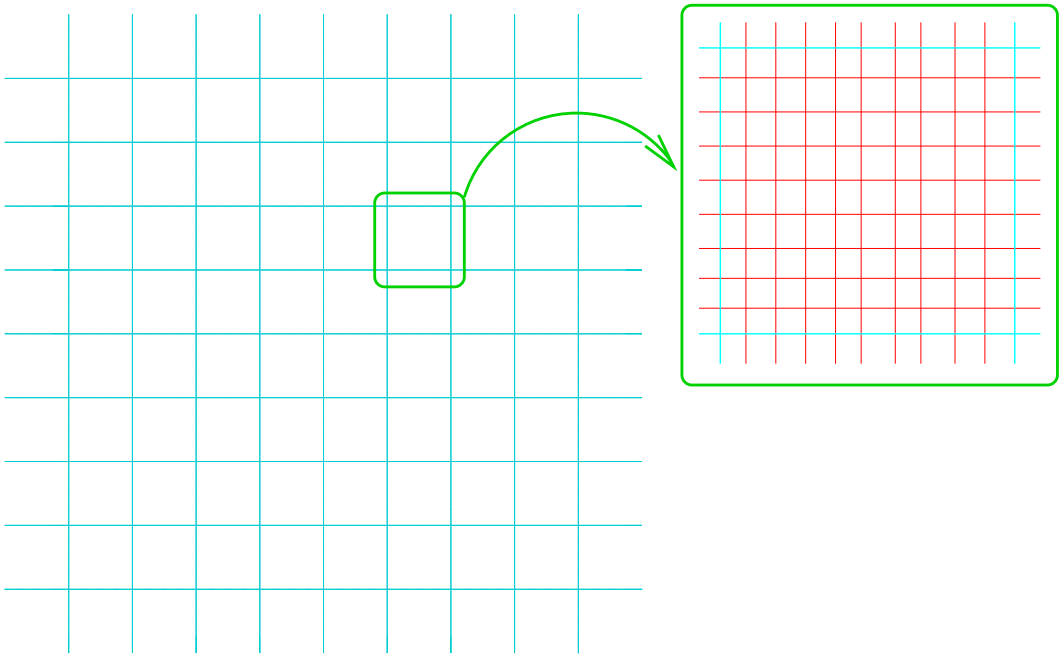

Figure 7.3: Studied system including two levels of fracturation, the second in-bedded in the former.

Block length	150 m
Fr. (Type 2, with fr. coat., mylonite ...)	2.56 cm
Matrix blocks length	15 m
Transmissivity	$1.10^{-7}\ m^2/s$
Fracture porosity	5.10^{-2}
Velocity	$7.79 * 10^{-8}\ m/s$

Table 7.1: Parameters associated with larger fractures (150 m scale)

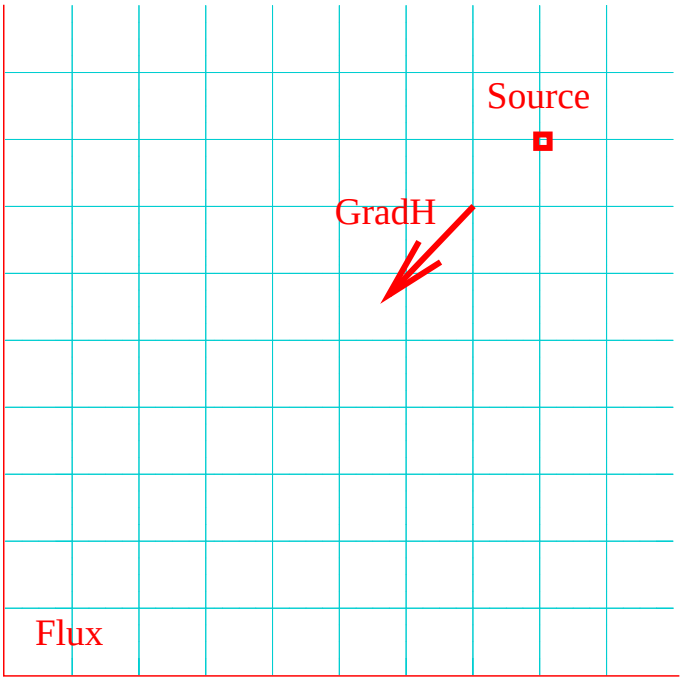

Figure 7.4: Initial and boundary conditions

Minor fracture aperture (Type 2)	0.56 mm
Transmissivity	$1.10^{-8}\ m^2/s$
Fracture porosity	0.15
Velocity	$5.95 * 10^{-8}\ m/s$

Table 7.2: Parameters associated with minor fracturing (15 m scale). Fracture coating is included as increase of fracture aperture

Matrix length	15 m or 1.5 m
Matrix porosity	6.10^{-3}
Pore matrix diffusion	$8.10^{-11} m^2/s$

Table 7.3: Matrix parameters (matrix zones in the vicinity of the flow path are homogenized as increased fracture aperture, we solely consider here altered rock properties

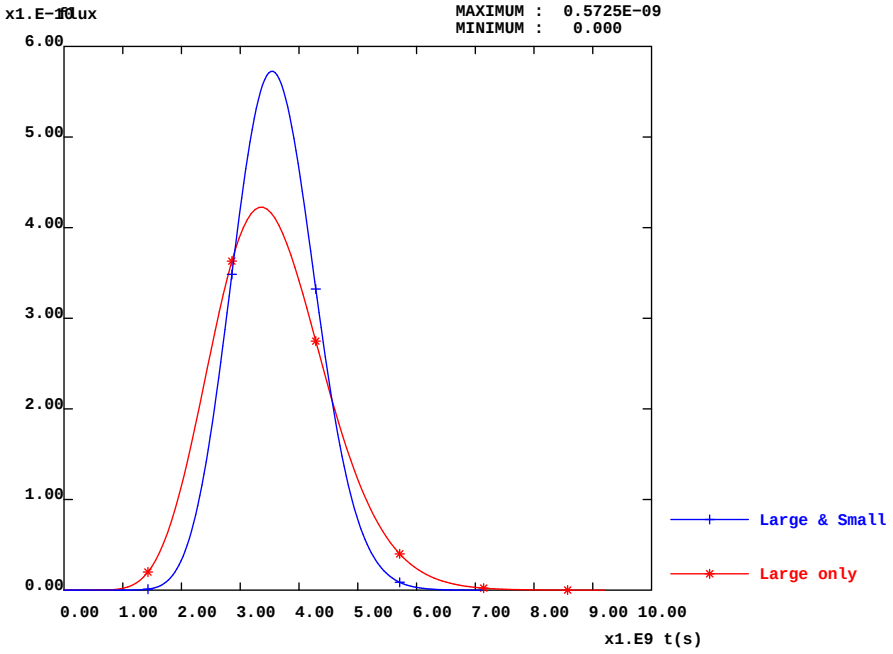

(a) Total flux exiting the system

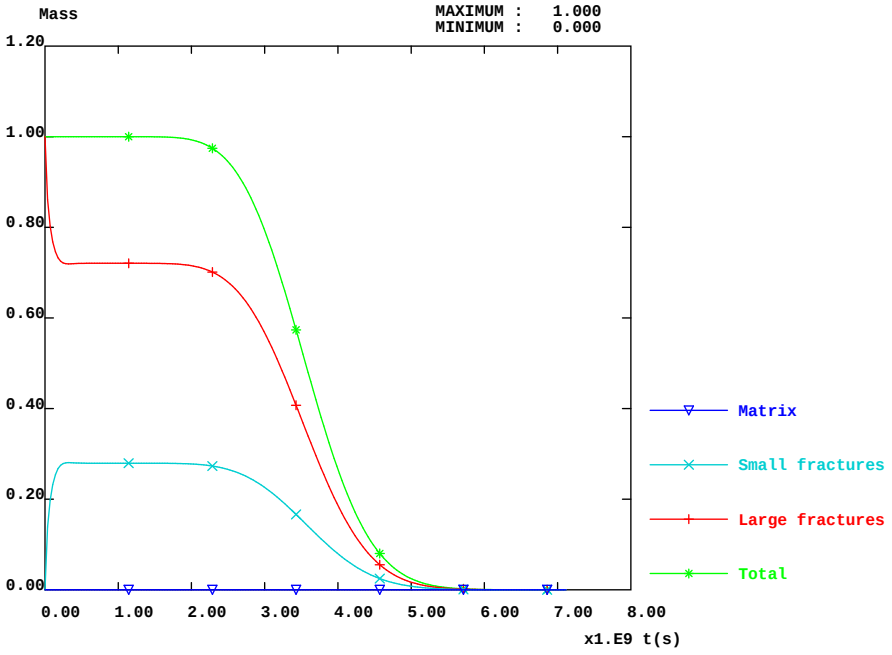

(b) Repartition of masses

Figure 7.5: Without matrix diffusion, BTC for both systems

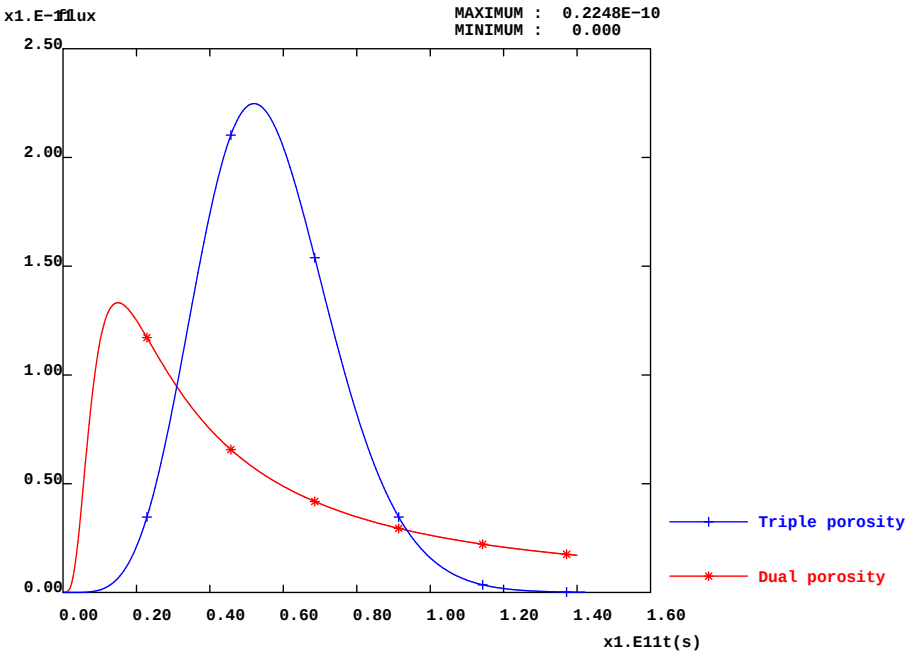

(a) Total flux exiting the system

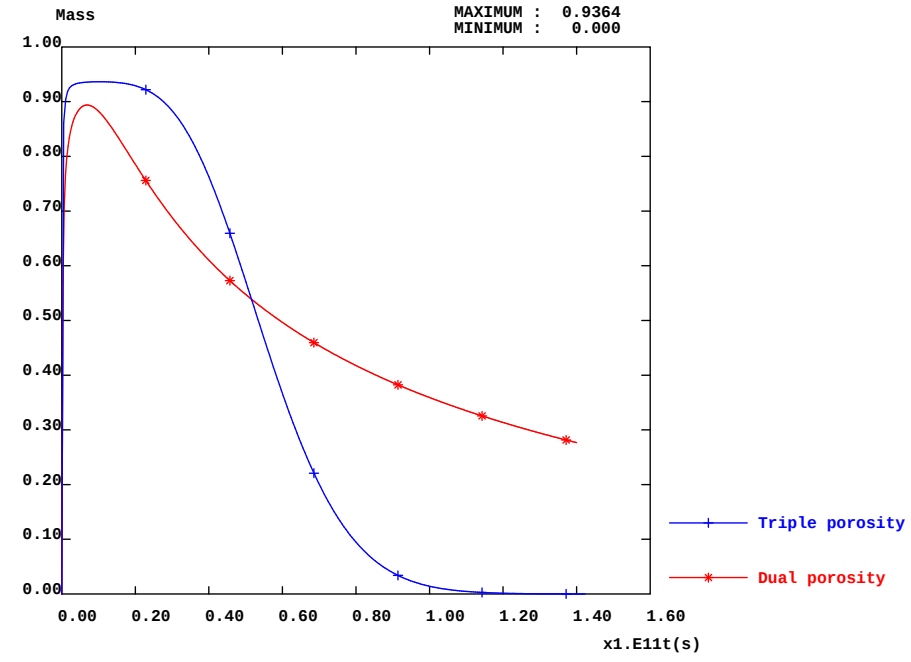

(b) Masses in matrix blocks

Figure 7.6: Triple porosity versus double porosity systems (including matrix diffusion)

Chapter 8

Discussion and conclusions

Main conclusions are provided within each task section. We ultimately here sum up the main conclusions.

- Tracer tests contain very limited amount of information to be transferred to PA time scale simulation.
- For PA time scales, matrix diffusion proved to be the major actor for retarding the plume. Intact rock mass located deeper in the rock mass is the major contributor as compared with matrix zones in the vicinity of the fractures due to the associated storage volumes. In addition to retarding the peak arrival time, resulting breakthrough curves provide long tailing effect. This feature is nevertheless strongly related with the low connectivity of the fractured block considered. As shown along Task 6F2, high connectivity would result into smaller matrix blocks and related smaller penetration depth resulting into highly retarded breakthrough curves but providing less tailing effects.
- Semi synthetic block provided by Task 6C showed low connectivity so that the 5600 features provided could be simplified to a major path of 12 fracture system providing almost identical breakthrough curves for the boundary and initial conditions considered.

Bibliography

[1] Äsp¨o Hard Rock Laboratory - 10 years of research. SKB. 1996.

[*Bear et al. 93*] J. BEAR, C.-F. TSANG, G. DE MARSILY (ED.). *Flow and contaminant transport in fractured rock*. ACADEMIC PRESS, 1993.

[*Carslaw and Jaeger 46*] H.S. CARSLAW, J.C. JAEGER. *Conduction of heat in solids*. OXFORD SCIENCE PUBLICATIONS, 1946.

[*Dershowitz et al. 03*] W. DERSHOWITZ, A. WINBERG, J. HERMANSON, J. BYEGARD, E.-L. TULLBORG, P. ANDERSSON, M. MAZUREK. *Äspö Task Force on modelling of groundwater flow and transport of solutes - Task6C - A semi-synthetic model of block scale conductive structures at the sp HRL*. MARCH 2003

[*Elert et Selroos 02*] M. ELERT, J. O. SELROOS. *TASK 6D modeling task specifications*. ÄSPÖ TASK FORCE, VERSION 1.0, 29TH NOVEMBER 2002

[*Elert et Selroos 04a*] M. ELERT, J. O. SELROOS. *TASK 6E Modelling task specifications*. ÄSPÖ TASK FORCE, VERSION 3.0, 20TH JANUARY 2004

[*Elert et Selroos 04b*] M. ELERT, J. O. SELROOS. *TASK 6F Sensitivity analysis - Modelling task specifications*. SIMPLIFIED 'TEST BENCH' TRANSPORT CALCULATIONS. ÄSPÖ TASK FORCE, VERSION 3.0, 15TH DECEMBER 2004

[*Elert et Selroos 04c*] M. ELERT, J. O. SELROOS. *TASK 6F2 Sensitivity analysis - Modelling task specifications*. ADDITIONAL TASKS. ÄSPÖ TASK FORCE, VERSION 1.0, 15TH DECEMBER 2004

[*Fourno et al. 03*] A. FOURNO, C. GRENIER, E. MOUCHE, H. BENABDERRAHMANE. *Qualification and validity of a smeared fracture modeling approach for transfers in fractured media*. PROCEEDINGS GROUNDWATER IN FRACTURED ROCKS, 15-19 SEPTEMBER 2003, PRAG (CZECH REPUBLIC). IHP-VI, SERIES ON GROUNDWATER, NO 7.

[*Grenier 04*] C. GRENIER. *Calibration of tracer test C2 in a semi synthetic block - Task 6D from the Äspö modeling Task Force exercise*. CEA INTERNAL REPORT SFME/MTMS/RT/04-004/A

[*Grenier 03*] C. GRENIER. *Modeling transfers in a single fracture system : from site characterization to performance assessment models. Contribution to Task A and 6B from the sp modeling Task Force exercise*. CEA INTERNAL REPORT SFME/MTMS/RT/02-022/A

[*Grenier et al. 98*] C. GRENIER, E. MOUCHE, E. TEVISSEN. *Influence of variable fracture aperture on transport of non sorbing solutes in a fracture : a numerical investigation*. JOURAL OF CONTAMINANT HYDROLOGY., 35, (1998), 305-313

[*Maloszewski et Zuber 85*] P. MALOSZEWSKI, A. ZUBER. *On the theory of tracer experiments in fissured rocks with a porous matrix*. JOURNAL OF HYDROLOGY, 79 (1985) 333-358.

[*Neretnieks et al. 80*] I. NERETNIEKS, *Diffusion in the rock matrix : an important factor in radionuclide retardation ?* JOURNAL OF GEOPHYSICAL RESEARCH, VOL. 85, NO. B8, PAGES 4379-4397, AUGUST 1980

[*Tang et al. 81*] D. H. TANG, E. O. FRIND, E. A. SUDICKY, *Contaminant transport in fractured porous media : analytical solution for a single fracture.* WATER RESOURCES RESEARCH, VOL. 17, NO. 3, PAGES 555-564, JUNE 1981